**FLAPPING WING MICRO AIR VEHICLE WING MANUFACTURE AND FORCE TESTING**

THESIS

Nathanael J. Sladek, Second Lieutenant, USAF

AFIT/GA/ENY/11-M14

**DEPARTMENT OF THE AIR FORCE**
**AIR UNIVERSITY**

# AIR FORCE INSTITUTE OF TECHNOLOGY

**Wright-Patterson Air Force Base, Ohio**

AFIT/GA/ENY/11-M14

**FLAPPING WING MICRO AIR VEHICLE WING MANUFACTURE AND FORCE TESTING**

THESIS

Presented to the Faculty

Department of Aeronautics and Astronautics

Graduate School of Engineering and Management

Air Force Institute of Technology

Air University

Air Education and Training Command

In Partial Fulfillment of the Requirements for the

Degree of Master of Science in Astronautical Engineering

Nathanael J. Sladek, BS

Second Lieutenant, USAF

March 2011

AFIT/GA/ENY/11-M14

**FLAPPING WING MICRO AIR VEHICLE WING MANUFACTURE AND
FORCE TESTING**


Nathanael J. Sladek, BS

Second Lieutenant, USAF



Approved:


_____        _____
Cobb, Richard G., Civ AFIT/ENY (Chairman)              Date

_____        _____
Reeder, Mark F., Civ AFIT/ENY (Member)                 Date

_____        _____
Black, Jonathan T., Civ AFIT/ENY (Member)              Date

AFIT/GA/ENY/11-M14

**Abstract**

Numerous wing manufacturing techniques have been developed by various universities for research on Flapping Wing Micro Air Vehicles. Minimal attention though is given to repeatability of wing aerodynamics and dynamic response, which is crucial to avoid asymmetric flapping. Thus the focus of this research becomes twofold. First, repeatable wing manufacturing techniques are developed to ensure flapping wings have similar aerodynamic and dynamic characteristics. For this purpose, four wing designs were selected to not only test the aerodynamics of the different designs, but to also validate manufacturing techniques. The various wing designs are assessed using two methods: dynamic and aerodynamic data. Dynamic data, specifically the wing's structural dynamic response, is measured using a 3D laser vibrometer. From this vibration data, the wings natural frequency modes can be determined which should correlate strongly within the various wing designs if the manufacturing techniques are repeatable. Next, using a piezoelectric flapping actuator, the four wing designs are flapped with force data collected. This data is then used to determine the aerodynamic characteristics of each wing. From the two methods of wing evaluation, it was found that the wings manufactured using a three-layer carbon layup showed greater structural dynamic modal repeatability as compared to one-layer carbon wings. Additionally, Wing Design 3 flapped with tfhe most efficiency with a significantly higher lift to drag ratio as compared to the other wing designs. From this research, the wing manufacturing techniques are quantitatively shown to be repeatable while an optimal wing design based on the maximum lift-to-drag ratio is found which can be used for future research.

iv

**Acknowledgments**

First, I would like to thank my thesis advisor Dr. Richard Cobb for his guidance, insight, and support in my research. Additionally, to Maj. Michael Anderson for his mentorship and partnership in developing FMAV wings and testing procedures. To Maj. Ryan O'Hara for his assistance in testing the FMAV wings. Furthermore, I thank Dr. Peter Collins and Mr. Charles McNeely of the AFIT Department of Electrical and Computer Engineering for assisting with the laser micromachining. Finally, to Dr. Greg Parker for funding this research and providing necessary support and materials. I would not have been able to complete my research without all of your help and for that I am very grateful.

<div align="right">Nathanael J. Sladek</div>

**Table of Contents**

# List of Figures

## List of Tables

# FLAPPING WING MICRO AIR VEHICLE WING MANUFACTURE AND FORCE TESTING

## Introduction

### 1.1 Motivation

Human fascination with flapping flight is not a recent development. Lenardo da Vinci designed one of the earliest ornithopters in the 15th Century but was unsuccessful in its implementation. For the next several centuries, flapping as a viable means of thrust and lift generation was neglected with manned atmospheric flight utilizing large Reynolds number aerodynamic principles to generate lift and chemical combustion to produce thrust [20]. With the progression of technology and miniaturization of electronic components, manufacturing of low Reynolds number unmanned air vehicles has become feasible within the last two decades as suggested by the RAND Corporation and MIT Lincoln Laboratory [14,6]. This prompted the Defense Advanced Research Projects Agency (DARPA) in 1996 to create the Micro Air Vehicle Program (MAV) initiative. The goals of this program are listed in Table 1.

**Table 1: MAV Requirements as Specified by DARPA [6]**

| Parameter | MAV Value |
|---|---|
| Size | <15 cm |
| Weight | 10-100 grams |
| Useful Payload | 1-18 grams |
| Endurance | 20-60 minutes |
| Airspeed | 30-65 km/hr cruise, hover is tradeoff with endurance/range |
| Range | 1-10 km |

Other MAV requirements and future goals are listed in Unmanned Aircraft Systems Roadmap [22].

Researchers at Cranfield University in the UK have created additional practical requirements for a MAV. Since MAVs are by definition small and would consequently have minimal energy storage capacity, they are not well suited to fly outdoors in what can be a very turbulent environment. Limiting the flight envelope then to indoor, the following requirements result: low speed, high agility, zero acoustic signature, vertical takeoff and landing, and autonomous flight [37].

In looking at MAV design, simply miniaturizing existing aircraft to meet the above requirements is not feasible. This stems from the fact that MAVs generally operate in a completely separate realm of aerodynamics due to their small size and low velocities [20]. Thus, MAVs fall into an aerodynamic class all its own with much to be learned. Thankfully, nature has already optimized micro air vehicles with the evolution of birds and insects, which become the instinctual inspirational candidates for the design of MAVs.

Numerous universities have undertaken the DAPRA challenge to produce a viable MAV with varying courses to that end. Significant fundamental research has been performed on how birds and insects generate lift and thrust. At a cursory glance, one would assume birds and insects flap very similarly. However, birds primarily flap in a vertical plane with minor changes to relative angle of attack of the wing. This results in birds having limited hovering ability. Conversely, insects flap principally in a vertical plane with significant changes in wing pitch during the flapping stroke enabling hover

[27]. This difference is where MAV design splits into designing bird or insect based MAVs which require different flapping mechanisms altogether.

Looking at the insect based flapping research, the flapping mechanism predominately rely on brushless DC motors or a piezoelectric motor with linkages transferring the motion of either force generator to the wing [4]. Wing manufacture and type varies significantly in terms of how repeatable the wings are, whether the designed wings are nature-inspired, and the materials utilized to build the wings. Researchers at Harvard University suggest that use of composites "provides a substantial performance improvement for microbotics" and that such materials are very advantageous over MEMs techniques [31]. As such, Harvard uses carbon fiber for vein structure and polyester for the wing membrane [32]. University of Florida has followed a similar path in manufacturing MAVs with carbon fiber also forming their wing structure and Capran for the wing membrane [23]. Some studies have also been performed on wing optimization and stiffness [3,19]. Also, in much of the aerodynamic testing, an additional hurdle is accurately resolving force measurements. Many researchers are resigned to developing their own strain gauges [17,29].

Although the kinematics of flapping wing motion has ben extensively researched, effectively replicating nature's fliers in terms of wing motion and dynamic response is a large field of continued research. In developing FWMAV wings, repeatability of the manufacturing techniques of MAV wings with consequent validation techniques has not been adequately explored in the literature. However, a critical step in developing viable MAVs is to manufacture wings with consistent dynamic and aerodynamic characteristics, which requires new manufacturing techniques.

**1.2 Research Goals and Focus**

The purpose of this research is to assist AFRL in ultimately developing an insect sized MAV capable of sustained hover and maneuverable flying. To this end, several intermediary goals are set. First, the need to develop repeatable wing manufacturing techniques is vital to ensure flapping wings have similar aerodynamic characteristics. For this purpose, four wing designs are chosen to not only test the aerodynamics of the different wing designs, but to also validate manufacturing techniques. These wing designs all have the same planform area and basic wing structure. With repeatable wings, this then avoids unintentionally imparting asymmetrical aerodynamic forces on the MAV. Additionally, these techniques could be utilized to develop optimal wing designs for testing. Through confidence in the manufacturing process itself, distinctions in the aerodynamic data between optimized wings would be due to wing design and not to manufacture variations.

These techniques need to rely on easily available materials and equipment. Thus, cured carbon fiber is used for wing structure and Kapton plastic for the wing membrane. Aluminum blocks are also used for wing molds. The carbon, Kapton, and aluminum wing molds are cut with a laser to ensure repeatability with the carbon cured in a programmable autoclave.

The next goal is wing evaluation. Repeatability of the wings is assessed using two methods: through dynamic and aerodynamic data. Dynamic data, specifically the wings' vibrational response is measured using a 3D laser vibrometer. From the vibrational data, frequency response functions can be generated which can be used to determine the natural frequencies of the wings. If the manufacturing techniques are repeatable, the

frequency of the wings modes should correlate strongly between each test for each wing design.

In order to gain reliable aerodynamic data, careful selection of the force/torque transducer must occur to accurately measure the milli-Newton flapping forces. Thus, a commercially available transducer with the lowest found resolution is selected to measure flapping forces. Prior to using this transducer, validation occurs to determine axis interactions, uncertainty, and noise thresholds. With the values known, aerodynamic testing can occur.

Utilizing a piezoelectric flapping actuator, the various wing designs with distinct manufacturing techniques are tested. This data is then used to determine how aerodynamically similar the individual wings perform.

Finally, with validated repeatable manufacturing techniques among various wing designs, an optimal manufacturing technique can be determined. Additionally, an optimal wing design is found which could be furthered refined in future research.

This thesis will first explore previous research on FWMAVs to include flapping motion kinematics and aerodynamics of insects, mechanical flappers, wing design and manufacture along with testing procedures. Next, the manufacturing techniques developed to create wings for this research will be explained along with how the wings were tested. The transducer validation procedures will be discussed along with data presented. Data will also be presented for structural dynamic and aerodynamic testing. Finally, an optimal wing manufacturing technique and wing design will be discussed.

**Literature Review**

## 2.1  Aerodynamics and Kinematics of Nature's Micro Air Vehicles

It seems prudent in order to gain an understanding of low Reynolds number aerodynamics, to first examine nature's MAVs. Through evolutionary processes, natural selection has developed a plethora of optimally designed fliers in birds and insects of varying size. These masters of flight can seemingly effortlessly take off and land vertically, hover to some varying degree, and are very maneuverable and efficient fliers. Yet a thorough understanding of the aerodynamics of insects and birds flight is not currently available. Several trends though, have been repeatedly observed and reported in the literature.

As mentioned previously, birds fly fundamentally differently than insects, flapping primarily in a vertical plane with small variations to pitch during wing stroke. Insects, conversely, dramatically change wing pitch during flapping to generate lift and thrust which also enables hover [25]. Since this research will primarily attempt to emulate the flapping motion of insects, the aerodynamics of ornithopter flapping will not be discussed.

Insect flight appears to be characterized by unsteady and nonlinear aerodynamics as suggested by recent research. This is how lift generation can be explained. Relying on traditional aerodynamic theory suggests insects should not be able to generate the lift forces they are producing. In exploring the unsteady aerodynamics of insect flapping, the wing stroke of an insect is divided into four distinct kinematic motions to include: two translational phases and two rotational phases. Translation is further characterized by the

upstroke and downstroke where the wings travel through the air with high velocity and angle of attack. During wing rotation, the wings quickly rotate, pronating during the downstroke and supinating during the upstroke, and then reverse direction [7].

Within the upstroke and downstroke, several flapping kinematic characteristics can be defined to include: stroke amplitude, wing beat frequency, wing angle of attack, stroke plane angle, downstroke/upstroke ratio, wing tip trajectory and timing for wing rotation. The value of these parameters differs from insect to insect and from wing to wing for a specific insect. That is, during a certain task, one wing could have certain kinematic characteristics while the other wing or wings could have different parameters. Typically though, during flapping, the wingtip of a given insect follows a figure-eight-like pattern, which is thought to optimize lift and thrust during the wingstroke. Figure 1 shows wingtip patterns for various insects [4].
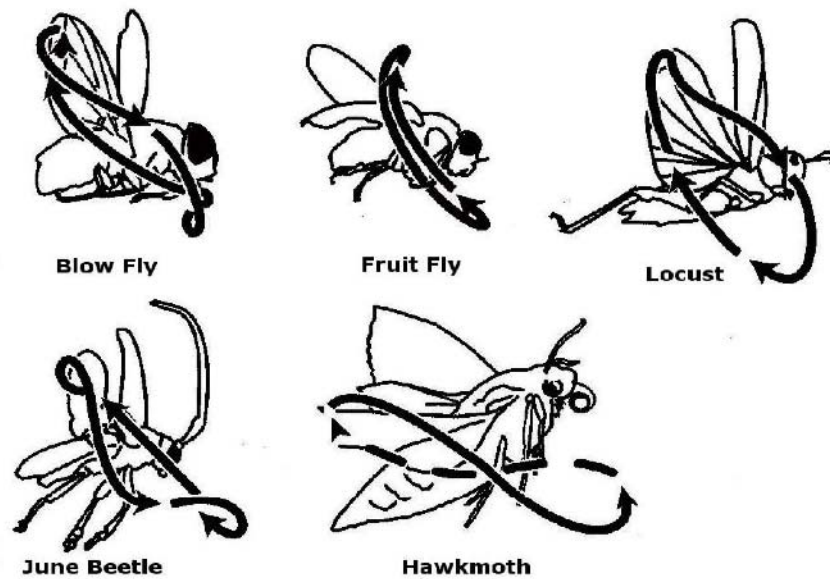


**Figure 1: Wingtip Paths of Various Insects [4]**

The path of the wingtip is calculated through the vector sum of the flight, flapping, and downwash velocities. It is essentially the path tangent to the relative wing velocity. Lift is perpendicular to this vector while drag is parallel [9].

Upon further examination of wingstroke pattern, several conclusions result. First, one of the original trends in flapping motion and consequent unsteady aerodynamic effect to be discovered was clap and fling. This phenomenon is seen during wing rotation in which the wings "clap" together during pronation quickening the production of circulation in the proceeding downstroke. Although seen in some insect species, this unsteady aerodynamic effect cannot be applied generally to insects [7].

Using dynamically scaled models of hawkmoths, other lift generating means are found. With increasing angle of attack, greater levels of circulatory forces develop. Due to the existence of axial flow along the wing, the Leading Edge Vortex (LEV) is maintained resulting in a delayed stall effect [7].

Ellington proposes this same concept. Since the flight of insects is exclusively in the laminar flow realm, most of the lift generated by insects is attributed to the LEV. This results from the generally pointed leading edge of insects' slender wings. This LEV can in part explain the high maneuverability of insects because it enables lift generation at high angles of attack [9].

The concept of a delayed stall should suffice to enable insects to generate positive lift, however this method cannot account for the fact that insects are capable of producing lift values twice their body weight. To examine this feat, Dickinson et al constructed a dynamically scaled fruit fly model to explore other lift generation methods. In this, they discovered the existence of rotational circulation. Analogous to the Magnus effect

(production of lift by surface rotation), it was found that the lift force peaked at the termination of the half-stroke due to the rotation of the wing sucking air into its boundary layer thus generating circulation. That is, as the wing travels through the air, circulation and hence velocity increases on top of the wing. This creates a favorable pressure differential and resultant increase in lift. To take full advantage of this effect, the wing should pronate prior to the downstroke and supinate before the upstroke. If the wing reverses later than desired, a downward force (negative lift) results [7].

From their fruit fly model, Dickinson et al found an additional aerodynamic phenomenon called wake capture. They surmised that rotational circulation alone does not account for significant lift generation at the beginning of the upstroke. In wake capture, the wing takes advantage of the added vorticity of the air from the previous flapping stroke. This fact was proven by stopping the flapping of the wing at the end of the half stroke and determining if lift is still being generated. They found that there is a positive force generated several hundred milliseconds after flapping ceases. As with rotational circulation, timing is everything. Positive lift is created when wing rotation occurs prior to stroke reversal. If rotation does not take place until the downstroke, negative lift will result [7].

Singh and Chorpa correlated these findings through mechanical experimentation with their dynamically scaled Robofly model. They found that the LEV is the primary thrust generating mechanism suggesting that during the down and upstroke phases of the flapping, significant lift results from the LEV. The resulting pronation and supination generate lift from rotational circulation and that lift is also generated through wake capture as the wing passes through the previously created wake [25].

9

Relating the basic aerodynamic gauges as a whole to the aerodynamics of MAV flight, new equations must be developed. Turning first to the fundamental ratio of momentum to viscosity, the Reynolds number for a flapping wing is defined as

$$Re = \frac{\bar{V}_{tip}\bar{c}}{\nu} \tag{1}$$

where $\bar{V}_{tip}$ is the mean wingtip velocity, $\bar{c}$ is mean chord, and $\nu$ is kinematic viscosity [4].

Knowing the mean wingtip velocity equals $\bar{V}_{tip} = 2\phi f L^2$ where $\phi$ is the peak-to-peak wingtip amplitude, f is the wing beat frequency, L is wing length and the mean chord equals $\bar{c} = 2L/AR$ where AR is the wing aspect ratio, Re can be redefined as [4]:

$$Re = \frac{4\phi f L^2}{\nu AR} \tag{2}$$

For better comparison between insect flapping speed, a dimensionless speed parameter akin to propeller theory is presented. This parameter is called the advance ratio or J and is defined as

$$J = \frac{V}{2\phi f L} \tag{3}$$

where V is the flight velocity [10]. This ratio is zero during hover since V=0, with an upper limit of 1. Additionally, as the advance ratio increases to achieve optimal motion,

10

the tilt of the flapping plane increases from zero for hover to some larger value depending on the thrust to lift ratio. Figure 2 demonstrates this for a bumblebee [10].



Hover
*J*=0

1 m s⁻¹
*J*=0.13

2.5 m s⁻¹
*J*=0.32

4.5 m s⁻¹
*J*=0.58
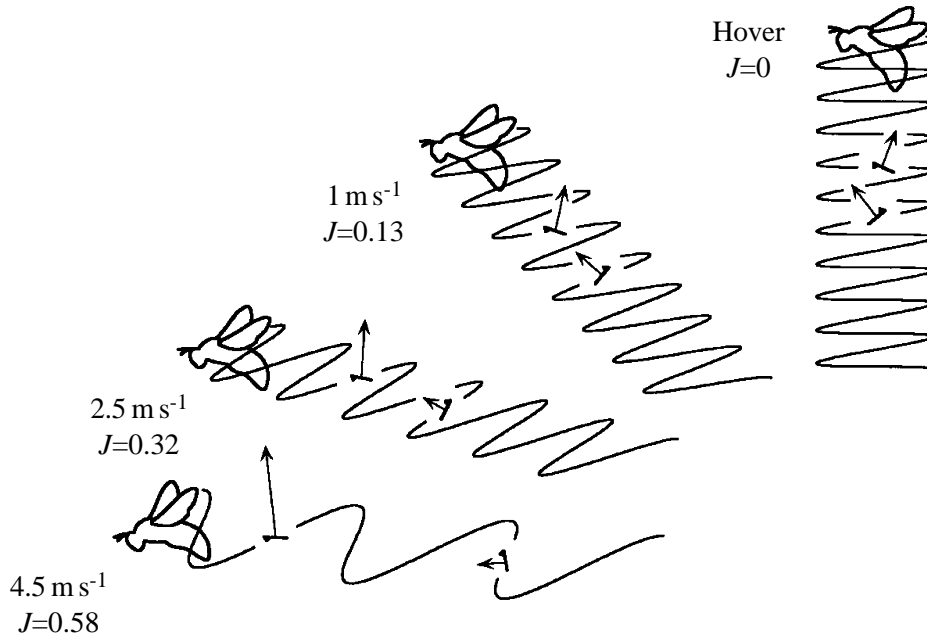
**Figure 2: Relative Orientation of a Bumblebee as Advance Ratio Increases [10]**

The literature also cites that the magnitude of the lift generating mechanisms varies depending on Reynolds number. Using the Robofly, Birch et al found that axial flow, which maintains the LEV, is absent at a Re of 120 [2]. A decrease in the lift coefficient for Re in the 10,000 to 50,000 was observed by Ellington and Usherwood [8]. This suggests a decrease in LEV strength at larger Re and furthermore that the LEV is not well understood [25].

Replicating rotational circulation, wake capture, and maintaining the LEV to delay stall are critical to a viable MAV design. As seen from Dickinson et al, timing of

rotation is of great importance when maximizing lift. In order to achieve this specific

timing, the kinematics of an insect's thorax must be accurately mechanized [4].

## 2.2 Mechanizing the Thorax

The process of applying the knowledge of how insects fly into man-made devices

to replicate that motion is extremely complex. In this effort, not only must some device

produce sufficient force at a high frequency to create the flapping motion, that force must

be efficiently transferred to the wings. The complexity increases significantly as greater

miniaturization is desired.

In considering how flapping motion can be created, it is first beneficial to return

to the examination of insects. The force moving the wings up and down is simply the

muscular contraction and expansion of the thorax. As Figure 3 shows, as the thorax

compresses, the wings are forced up due to the linkages. The opposite is true as the

thorax expands [37].
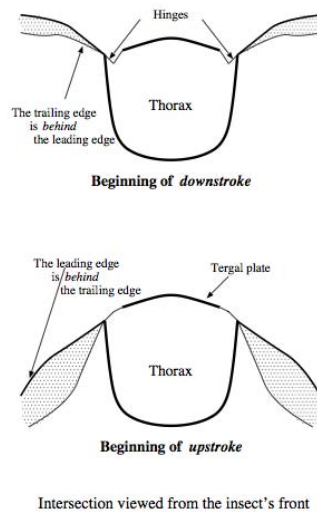


**Figure 3: Compression and Expansion of an Insect's Thorax [37]**

This compression and expansion can be mechanically replicated through a variety of methods. Most commonly used is a brushless DC motor with crank and rocker linkages. Additionally, if miniaturization is desired, a piezoelectric motor can be utilized with some form of a crank and rocker. Table 2 shows some of the advantages and disadvantages of various actuators [4].

**Table 2: Qualitative Summary of Rotary Actuators [4]**

| Rotary Actuator | Advantages | Disadvantages |
|---|---|---|
| Brushed DC Motor | Simple operation with no drive electronics required | Size and mass may be an issue |
| Brushless DC Motor | Miniature size and mass | Drive electronics required |
| Piezoelectric Motor | Miniature size and mass with high torque at all speeds | Product choice is limited High voltage and driver electronics required |
| Micro Internal Combustion Engine | High power density and efficiency | Novel technology currently under development |

In actuator selection, it is crucial to consider maximum stress/torque, maximum frequency/angular velocity, maximum energy density, efficiency, mass and volume [4]. As with all engineering, there is a tradeoff between certain characteristics of all actuators. Although piezos provides high torque despite their smaller size, they require high voltage. Many researchers have utilized the brushless DC motor for its ease of application and widespread availability.

Looking at more quantitative criteria for flapping mechanism, Ellington provides some useful equations. Since a particular flapping mechanism is most efficient at resonance, it should typically flap at this value. This is similar for insects with little deviation from the optimal flapping frequency. Therefore, an efficiency factor can be

13

applied to a particular flapping mechanism using Equation 4. Flapping mechanisms

should be designed so that Q is maximized [10].

$$Q = 2\pi \frac{peak\ kinetic\ energy\ of\ oscillator}{energy\ dissipated\ per\ cycle} \tag{4}$$

For practical MAV testing, flapping mechanisms should be designed such that the

mass that could actually be supported by the flapping itself is not exceeded. As shown in

Ellington, the mass that could be lifted by a MAV using a particular flapping mechanism

is found using Equation 5 [10].

$$m = 0.387 \frac{\phi^2 f^2 L^4 C_L}{AR} \tag{5}$$

Mass (m) has units of kg, $\phi$ radians, f Hz, and L meters where $C_L$ is the coefficient of lift.

To create a mass specific power requirement, the following equation is used with units of

W/kg [10].

$$P_{sp} = 14fL \sqrt{\frac{\phi C_L}{AR}} \tag{6}$$

These equations provide valuable general guidelines when designing a flapping

mechanism [10].

Turning now to current research on flapping designs, several designs are analyzed. The University of Florida uses a 15W brushless DC motor with a 57/13 reduction ratio planetary gear head, a 256 counts-per-turn encoder and an EPOS 24 controller. This setup provides continuous feedback to the motor allowing for precision control of flapping frequency. This design flaps two wings simultaneously [36].

The flapping motion itself is created by a reciprocating crank-slider, which transfers the motion to the wings using linkages. Since a single rotational source is used, asymmetry between the individual wings is minimized. The gear head shaft is capable of outputting 124 revolutions per second resulting in a flapping frequency up to 124 Hz. This high frequency flapping is one of the significant advantages of using a DC motor for force generation. The bandwidth of this type of system is typically very large and not flapping frequency limited, but rather amplitude. Flapping amplitude is adjusted using various slots resulting in potential angles of $\pm10°$ to $\pm60°$. This type of design relies on ball bearings and lubrication to reduce friction between components. As such, components are prone to wear and tear, but the mechanism is designed such that worn pieces can easily be replaced. This particular flapper does not actively control angle of attack. The setup of this flapper is shown in Figure 4 [36].
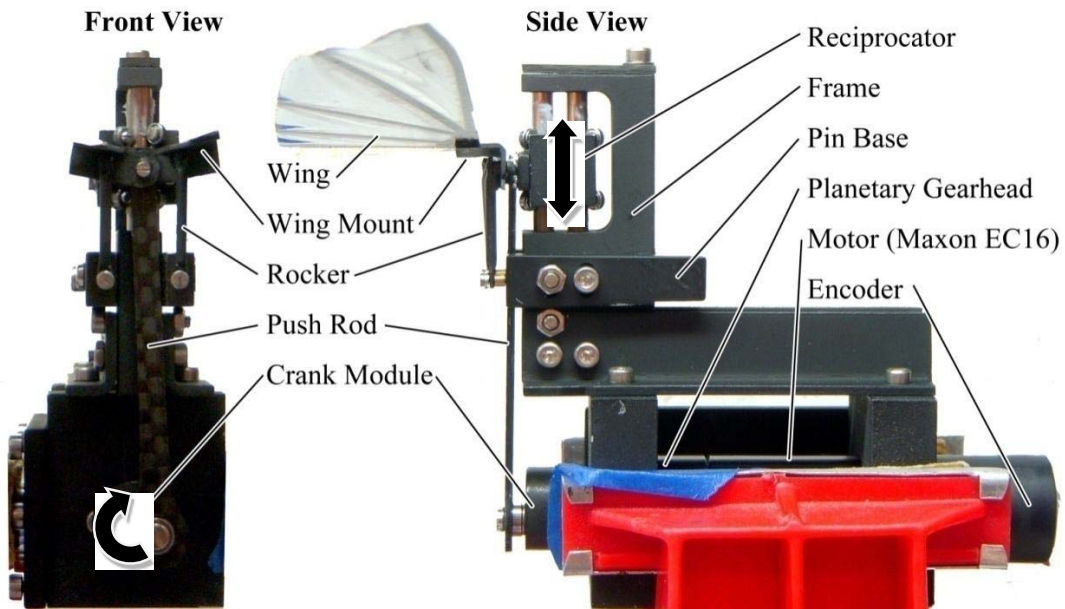
**Figure 4: University of Florida Flapping 1 DOF Flapping Mechanism [10]**

Similar flapping mechanism setups are found in [21,25].

Kumar et al designed a 3 DOF flapping mechanism with adjustable pitching angle. This design also utilized a DC motor to achieve a maximum flapping frequency of 35Hz. Additionally, the linkages result in a flapping amplitude of approximately 85 degrees and pitching amplitude of 60 degrees [17].
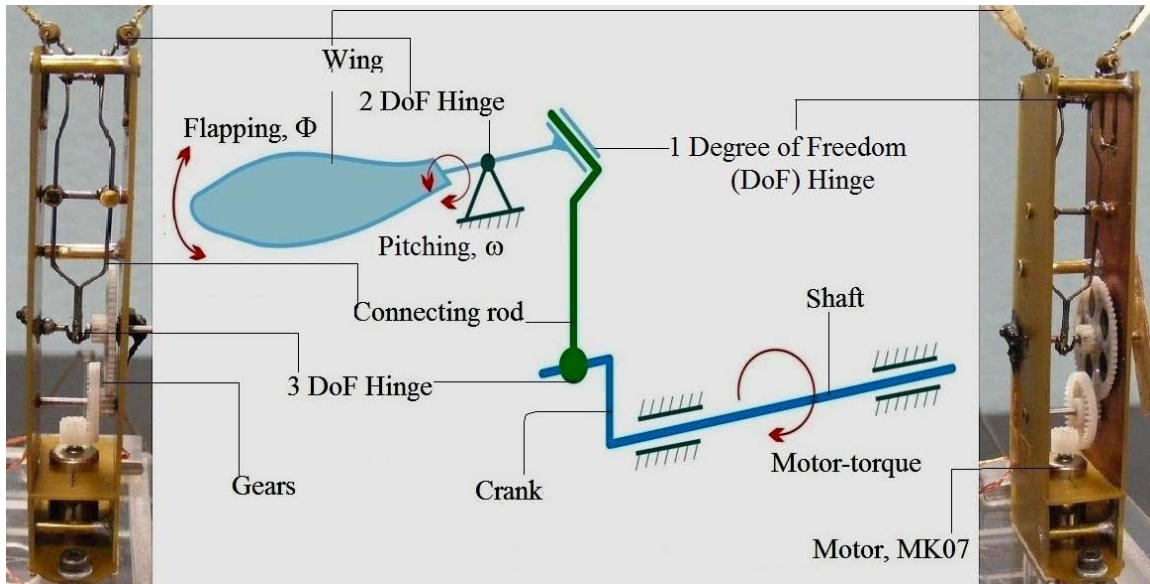
**Figure 5: Kumar et al 3 DOF Flapping Mechanism [17]**

A similar setup to this design is found in [4, 30, 37].

Up to this point, the examined flapping mechanisms have relied on a DC motor and crank slider to achieve flapping and some linkage constraint to force pitching. Researchers at Harvard University explored a different route. Using piezoelectric motors as their force generator and a four bar linkage for transfer of motion, they can achieve greater mimicking of nature. For this setup, wing rotation is achieved through the dynamics of the wings being tested [31].

Returning to Figure 3, the compression and expansion of the thorax is linearly actuated. In the same way, the displacement resulting from the movement of a piezo would cause these same contractions and expansion with proper linkages. In Harvard's flapper, all the displacement of the piezo is used to generate the maximum wing stroke. Maximizing wing stroke will in turn maximize the instantaneous wing velocity. The basic four bar linkage is shown in Figure 6 [31].

17
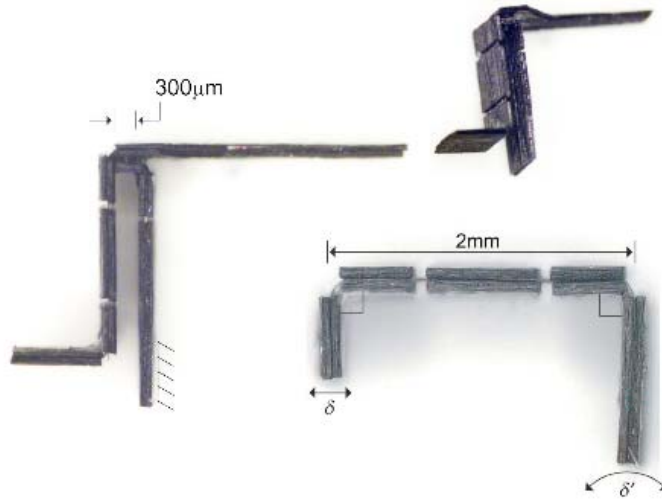
**Figure 6: Four Bar Linkage for Harvard's Flapping Mechanism [31]**

Utilizing an in house manufactured bimorph piezoelectric optimized for the specific flapping goals (required energy density), very efficient flapping motion can occur through simply adjusting frequency and amplitude with the input voltage. The linkages themselves are constructed using Smart Composite Microstructure as discussed in [34]. Manufacture of the piezoelectric motors themselves can be found in [33]. Figure 7 below shows a piezo, the linkages, and entire flapping setup [31].
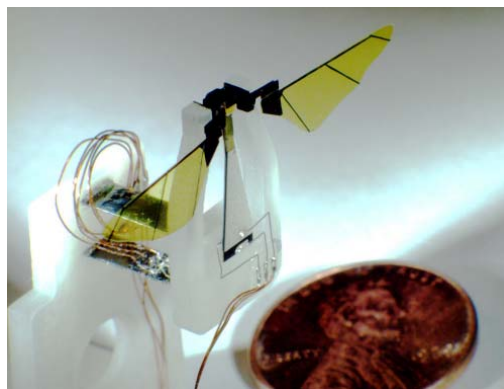


**Figure 7: Harvard Flapping Mechanism [31]**

Beneficial equations in designing a piezoelectric flapping system are found in [31]. Additionally, in Wood et al, a more detailed description of the micromachining process and four-bar linkage is given. A paper outlining the principles of using lasers to micromachine materials is found in [28]. Woods' work is the inspiration for the larger piezoelectric flapping found in Anderson et al, which is used in this testing. Anderson also provides a series of equations describing the kinematic motion of the flapper [1].

With flapping mechanisms explored, the next crucial step in emulating the flapping motion of insects is wing design and manufacture.

## 2.3  Micro Air Vehicle Wing Design and Manufacture

Designing a flapping mechanism to mimic the thorax is only half the challenge when creating mechanical fliers. Although these devices can provide some precise articulation forcing the wing to pitch at certain times within the stroke, replicating the aerodynamics and dynamics of an insect wing is a very daunting challenge.

In determining the most effective way to create MAV wings, several helpful references can be found. First, looking at the basic wing structure, the veins of the wing serve to support the membrane providing rigidity but can also elastically transmit force. Although many insects' wings have a myriad of veins, including the entire vein structure in the design is not necessarily required. The basis for this argument is examination of a fruit fly wing, which has a relatively simple vein structure as shown in Figure 8 [37].
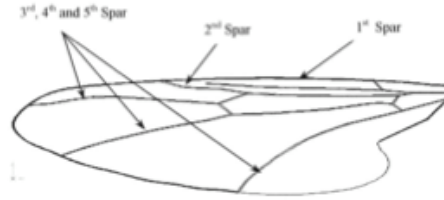
**Figure 8: Fruit Fly Vein Structure [37]**

The vein structure needs to apply sufficient resistance as to prevent the membrane from tearing but also enough flexibility to move with the inertia of the membrane. The vein structure also must be strong enough to withstand the bending and twisting of the wing during flapping. Additionally, to ensure rotation at the end of the half stroke, the center of mass of the wing should be located behind the torsional axis [37].

Examining the spars, the following characteristics are proposed by Zbikowski and Pedersen: high specific strength, low specific modulus, low elastic modulus. In essence, the veins should be able to significantly deform without failure and be able to withstand repeated deformation without fatiguing. These researchers suggest using copolymers to meet this purpose [37].

In designing MAV wings, there is an apparent balance between rigidity and flexibility as in the wing design of aircrafts. A flexible wing will conform to the inertial loads delaying stall. Through testing, a fixed rigid wing as defined by Viieru et al, will stall between angles of 12 and 15 degrees while a flexible wing will stall between 30 and 45 degrees. Although this research will not utilize fixed wings, the same concepts can still apply [29].

Hu et al found a similar result testing both flexible and rigid membrane wings of the same design. They found that the flexible wings had improved overall aerodynamic

performance than the rigid wings in terms of lift to drag ratio. However, the rigid wing exhibited better overall lift production [12].

Researchers at the University of Washington examined actual insect wings to determine the flexibility. Using the forewings of 16 insects, they measured the flexural stiffness along the spanwise and chordwise directions. They found that spanwise stiffness was best correlated with wingspan and chordwise stiffness with chord length. Spanwise stiffness was also 1-2 orders of magnitude greater than chordwise flexural stiffness. In their analysis, they also found that all insects had a group of thicker veins at the leading edge. This additional stiffness in the spanwise direction would limit bending along the span of the wing, but allow passively or through articulation, camber in the chordwise direction [3].

Wing dihedral is explored by Shkarayev and Silin. They tested dihedral angles of 0°, 8°, and 19° respectively for flapping frequencies ranging from 5 to 23 Hz. Their research showed that for increases in dihedral angle, that the lift force generated increased significantly with a marginal increase in thrust. They also researched the effect of wing stiffness on lift production. As found in Hu et al, the stiffer wings produced more lift, however the propulsive efficiency decreased significantly. The flexible wings were 1.5-2 times more power effective than the rigid wings [24].

With the process of wing design explored, the focus now turns to implementation. Several universities have developed MAV wings for testing using a variety of material and methods. Their processes will be discussed next.

At the forefront of MAV research is the University of Florida with their wing manufacture being a crucial component to their success. They have attempted to design

their wings will similar kinematic properties to those wings found in nature. More

specifically, with size comparable to a hummingbird, elastic modulus comparable to a

cicada, and flapping frequency and Reynolds number comparable to a hawkmoth. Table 3

summarizes the various insects they are trying to artificially emulate, and the properties

of their wings being tested [35].

**Table 3: Kinematic Properties of Various Insect Wings and MAV Wings [35]**

| | Hummingbird (Various species/ages) | Hawkmoth (Various species/ages) | Cicada (*Homoptera, Cicadidae*) | This work (Wing and flapper) |
|---|---|---|---|---|
| Morphological parameters | | | | |
| Wing length ($b$) | 37~100 mm | 35~150 mm | 45~55 mm | 75 mm |
| Chord length (c) | 9~25 mm | 9~46 mm | 14~18 mm | 25 mm |
| Aspect ratio ($2b^2/S$) | 7.0~8.0 | 5.8~6.0 | 8.0~8.6 | 7.6 |
| Wing weight | 50~300 mg | 50~4860[3] mg | 12~20 mg | 105 mg (average) |
| Single wing area ($S$) | 400~2500 mm$^2$ | 400~7500 mm$^2$ | 500~700 mm$^2$ | 1473 mm$^2$ |
| Structural parameters | | | | |
| Wing/feather $E$ | 2.5 GPa[4] | 47 MPa ~ 4.5 GPa | 3.7 GPa | 2.5~3.4 GPa |
| Wing/feather density | 1200~1400 kg/m$^3$ | 1200 kg/m$^3$ | 2300 kg/m$^3$ | 1600 kg/m$^3$ |
| Membrane thickness | N/A | 45~110 micron | 12.2 micron | 12~14 micron |
| Structure/skeleton $E$ | N/A | N/A | 1.9 GPa | 73.4 GPa |
| Structure density | 1000~1600 kg/m$^3$ | 1200 kg/m$^3$ | N/A | 1740 kg/m$^3$ |
| Kinematics parameters | | | | |
| Flapping frequency | 10~200 Hz | 8~30 Hz | 40~45 Hz | 5~45 Hz |
| Stroke amplitude | 144º~180º | 115º | N/A | 40º~90º |
| Reynolds number[5] | 7,000~15,000 | 5000~7000 | N/A | 1527~12,215 |

Ultimately, a Zimmerman wing planform with span of 150mm and root chord of

25mm was selected. Wings were manufactured using unidirectional carbon fiber with

0.8mm width to form the structure with Capran used as a membrane. A three-layer

carbon fiber wing mounting point to the flapper is also added to each wing. An example

wing is shown in Figure 9 [35].
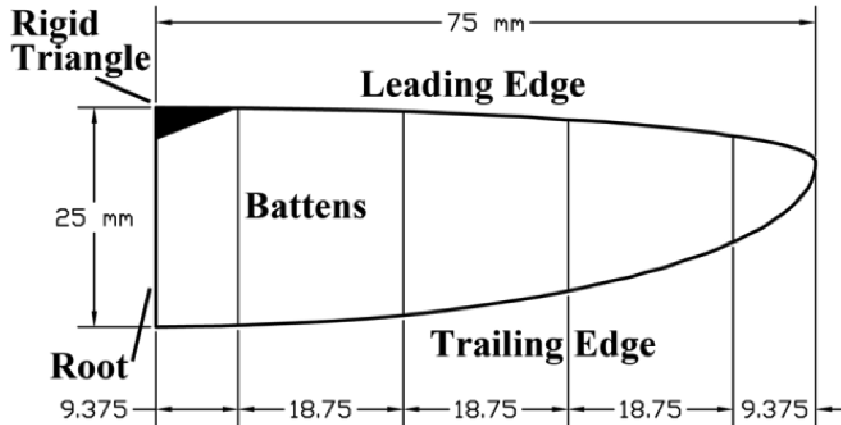
**Figure 9: Typical University of Florida Zimmerman Wing [35]**

To change the dynamic properties of the wing, more or less battens are added to the wing shown in Figure 9. In this way, the bending stiffness depends only on the main wing spar while torsional stiffness is a function of the battens [35].

Researchers at Harvard produce wings in a similar fashion. Using a 70μm thick ultra-high-modulus carbon fiber/epoxy composite sheet, they created very strong yet lightweight wings. The membrane used is 1.5μm thick polyester. Figure 10 shows one of their characteristic wings [31].
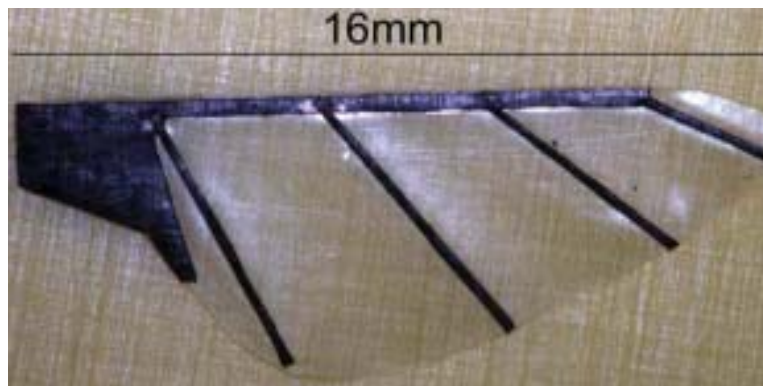


**Figure 10: Typical Harvard University Wing [31]**

Kumar et al manufactured wings in two distinct ways. First, using a main carbon spar with a thin sheet of balsa wood for wing membrane forms a wing weighing approximately 30mg. Additionally, the wing membrane is also manufactured by placing a very light grade of glass fiber fabric between epoxy resin layers. Carbon spars as before are used to provide structural rigidity. These wings weighed approximately 40 mg. The balsa wood wing, composite wing, and comparison to a locust wing, which was being mimicked, are shown in Figure 11 [17].
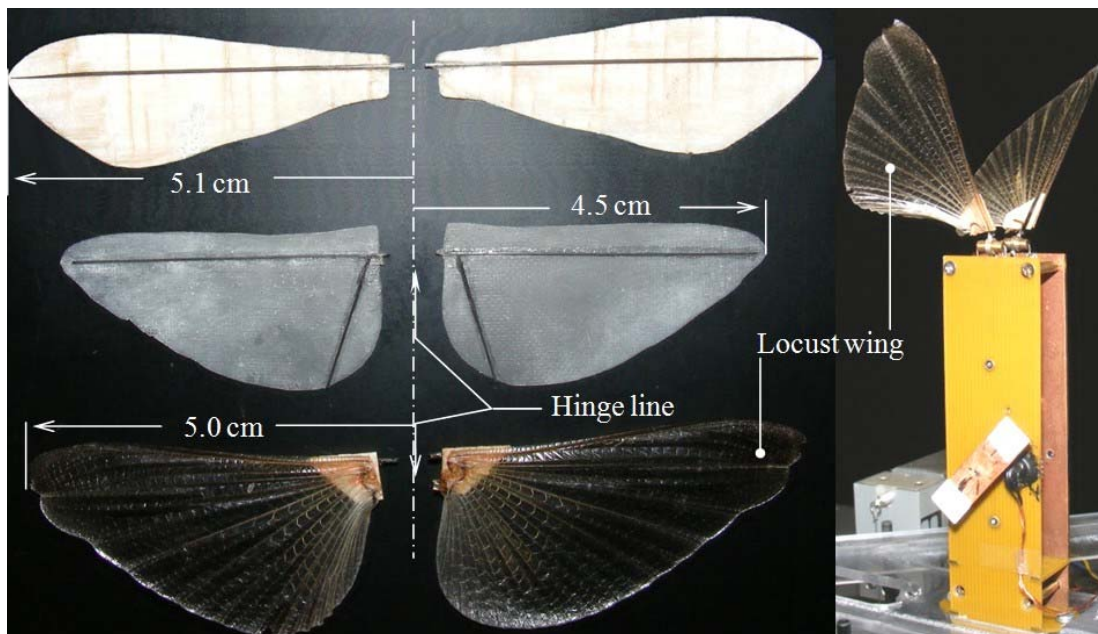


**Figure 11: Comparison of Balsa Wood, Composite, and Locust Wing [17]**

A similar wing structure design is found in Zdunich et al. For their wings, prepreg carbon fiber is cut into strips of appropriate size. The strips are layered on a flat plate to create the vein structure. Heat of 250 degrees F and a pressure of 13 psi are then applied concurrently to cure the carbon pieces together for 2 hours. The wing membrane consists

of 1 mil Mylar. An example of the carbon structure of the wing is shown in Figure 12 [38].



180 mm
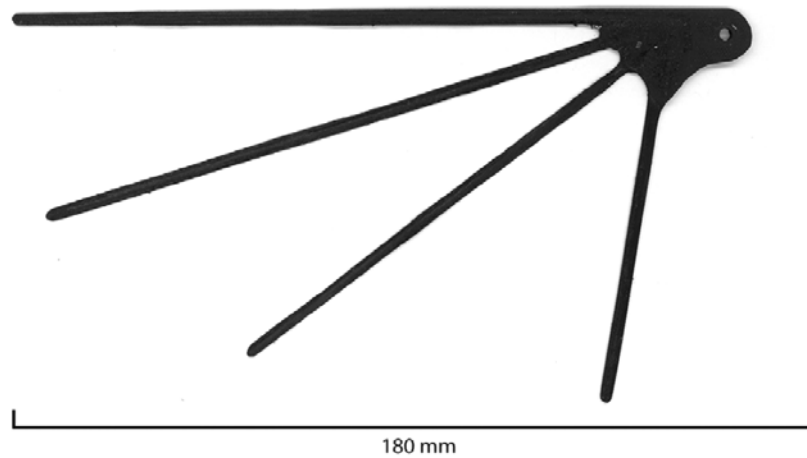
**Figure 12: Carbon Structure of Zdunich et al Wing [38]**

Instead of using composites to form the wing structure, Craparo and Ingram use foam placed over an inner and outer spar. The foam itself is cut into various sections with each wing comprised of six foam sections. Using various foam sections provides the advantage that the wing can effectively flex with the aerodynamic loads. Additionally, this type of wing is straightforward and simple to construct [5].

Although the individual foam airfoils are rigid, the outer spar is not. This spar is a 76µm thick C-section. Conversely the inner spar is a 1/16 inch diameter steel rod. Figure 13 shows the layup of this wing [5].
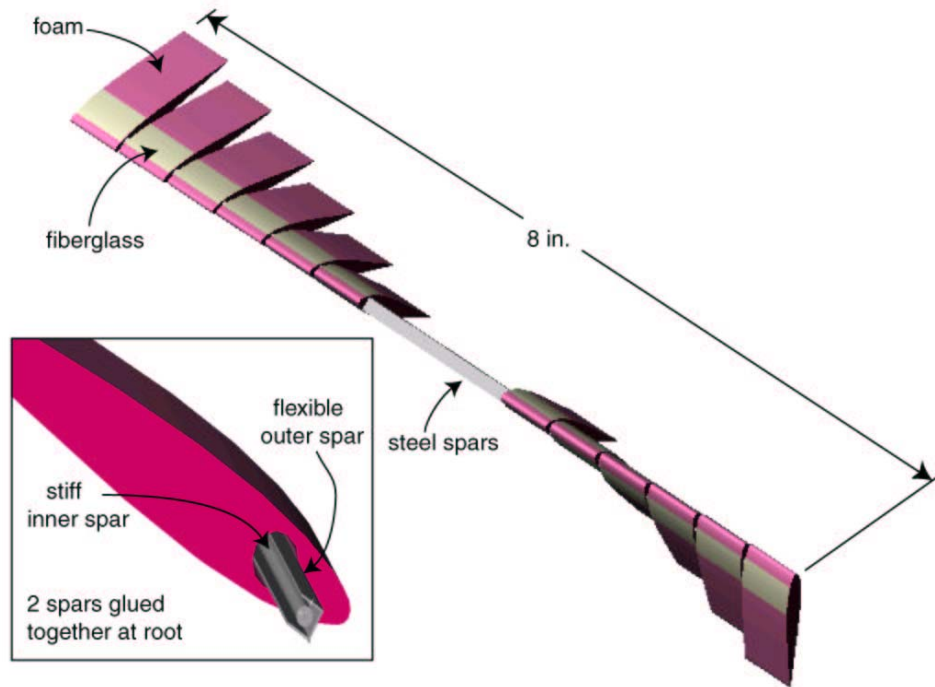
**Figure 13: Flexible Foam Wing [5]**

With methods to design and manufacture MAV wings, the next step becomes how to accurately test the wings and turn that data into useful aerodynamic data.

## 2.4  Testing of Micro Air Vehicle Wings

In typical aerodynamic investigations, the test object is placed onto a wing tunnel sting with a built-in force transducer, the tunnel runs at some representative velocity, and force and torque data is collected. For larger MAVs, especially those that do not flap but use a propeller to generate thrust, this would be a viable option. However, for testing MAV wings, which can generate forces in the millinewton range, traditional methods are no longer sufficient to capture the forces being generated.

26

Looking at research in measuring the forces generating by MAV flapping motion, there are two primary paths: specialized force/torque transducer or particle image velocimetry. Researchers have also started to use computational fluid dynamics as more refined modeling becomes available. More information on CFD modeling can be found in [18,27].

First, examining methods utilizing force transducers, Kumar et al constructed their own three-degree of freedom balance. Utilizing a platform that is secured to pins on six three-gram force load cells, they achieved a force resolution of 2mg or 0.01962mN. A picture of this design is shown in Figure 14 below. More information on this setup can be found in [16].
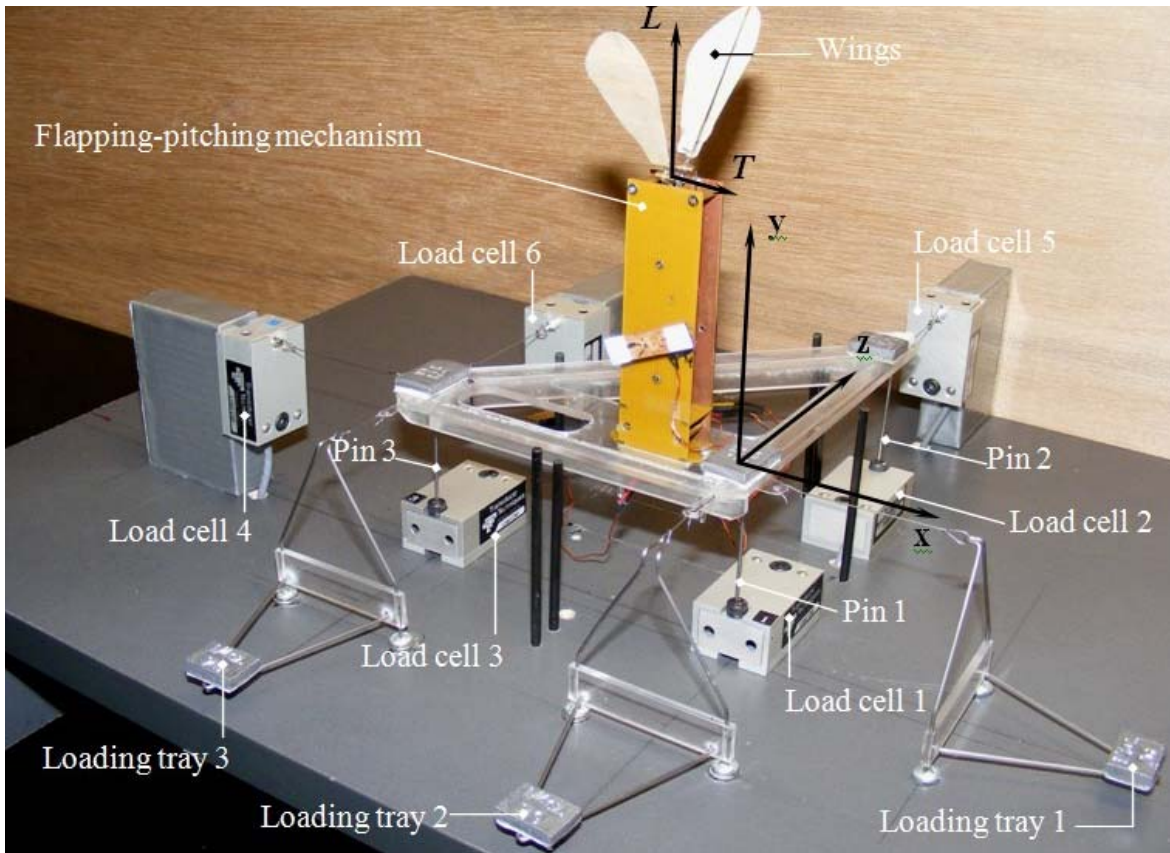


**Figure 14: Kumar et al Force Transducer [17]**

A simpler approach is found in Hu et al. They designed a mechanism that would simply measure the normal force or lift by using a lever. The lever can only pitch up and down about the pin joint. With the MAV fixed to one end with a known distance L, a mass located on the right was slid along the lever until the lever equilibrated. Another known mass was placed on the left side of the lever at some known distance $L'$ and during flapping the deflection of the lever from its previous equilibrated state is measured as $\theta'$. Using the following equation, lift can be found [2]:

$$Lift = \frac{mgL'cos\theta'}{L} \tag{7}$$

Rotating the MAV 90 degrees, this mechanism could also measure side force. It was found that a 0.02 gram mass was able to cause the lever to rotate thus the resolution of this system is 0.02 grams or 0.196mN [13].

Harvard University with its very small wings and consequent small forces, also resorted to a custom built force sensor. In designing the sensor, considerations were made such that the bandwidth of the sensor itself is 5x greater than the maximum flapping frequency. Additionally, the desired resolution was 1% of the weight of the entire flapping assembly. Using two parallel cantilever steel beams with semiconductor strain gauges, the sensor has a 400Hz resonant frequency and a resolution of approximately 10μN. Greater detail of this setup can be found in [32].

Looking at more conventional methods using commercially available force transducers, University of Florida utilized a 6 degree of freedom ATI Industrial

Automation Nano17. In their setup, this transducer is mounted underneath their flapping mechanism. This transducer has a specified resolution of 0.319g or 3.127mN for the x, y, and z axes. Prior to data acquisition, the sampling rate is set to correspond to 500 samples per flapping cycle as dictated by the flapping frequency. Samples are then averaged to obtain representative force values [35].

Since a mechanical flapper is being utilized which ultimately causes vibrations, the transducer would record these values. However, since the mechanical system conserves momentum, the time average of these vibrations would equal zero [35].

In measuring the forces produced by flapping MAVs, another common approach is to use Particle Image Velocimetry (PIV). In Sallstrom et al, a stereoscopic LaVision PIV system is utilized with two cameras with 2048 x 2048 pixel resolution with 7.4 x 7.4 $\mu m^2$ sensor pixel size. Full resolution images can then be captured at 14 Hz. A Nd:YAG laser system is used to create the laser light sheet. Seeding is performed using olive oil with a particle size of 0.25 μm. The terminal velocity of the particles is computed to be 1.7 μm/s or 6 orders of magnitude lower than the flow velocity. To validate results from the PIV, force measurements are also taken. PIV was well corroborated by the force data and thus seen as a viable method to indirectly measure forces [23]. PIV is also used by researchers at Purdue University and University of Dayton as discussed in [13,11].

Through examining the literature, valuable insight is gained specifically in the different types of flapping actuators, wing design and manufacture, and testing techniques. These three components are critical to this research and what the rest of this thesis will focus on.

## Methodology

### 3.1  Wing Manufacture

At the onset of this research, the structure of the wings consisted of unidirectional, uncured carbon fiber cut with an X-ACTO knife. These pieces were laid arbitrarily over Kapton plastic on a flat plate of aluminum covered with a sheet of Teflon. Another plate of aluminum with a sheet of Teflon was placed over the carbon/Kapton layup, the two plates were clamped together using nuts and bolts, and the assembly was then placed into an oven to cure. Although an effective means to produce wings, there was no repeatability, thus the process required significant refinement. This section will discuss the various methods utilized to manufacture wings with the most successful methods presented in sections 3.1.4  Wing Manufacture Method Three and 3.1.5  Wing Manufacture Method Four.

### 3.1.1  Cutting the Wing Components

Four wing designs of varying shape were selected to provide a means to develop repeatable techniques for wing manufacture. In designing the wings, considerations are made such that the wing shape is the primary variable. Testing would then distinguish the effects of lift and drag on the various wing designs. With this in mind, the surface area of each wing design is held constant and purposefully chosen to be smaller than that of a hawkmoth but larger than a fruity fly. The design area selected is 369 mm$^2$. Additionally, all the wings have the same overall dimensions in wing vein structure width with the primary spar having a width of 0.75 mm and protruding veins tapered from 0.5 mm to 0.35mm. These overarching design decisions are made with the intent that all the wings

30

will then have approximately the same mass. The membrane material for wing manufacture is 7.5μm Kapton plastic and the vein structure consists of 80μm unidirectional carbon fiber.

Wing Design 1 consisted of a rectangular shape and served as the proof of concept to develop the manufacturing process while the other three designs were bio-inspired. Design 2 is an ellipse, chosen primarily for its consistent curvature but is also seen in nature in the Odonata Lestes species. Design 3 combines the straight primary spar of the rectangular wing design while adding curvature at the wing tip similar to the ellipse wing. The overall shape of this design is seen repeatedly in nature as well with species in the Hymenoptera family. The final wing design, like the previous, has a long straight spar but the tip has a much more dramatic curvature. This wing has a fairly symmetric distribution of surface area like the ellipse, but is shorter. This design is inspired from the Manduca sexta [25]. The membrane and wing structure of each wing were drawn in SolidWorks and are shown in Figure 15 below.
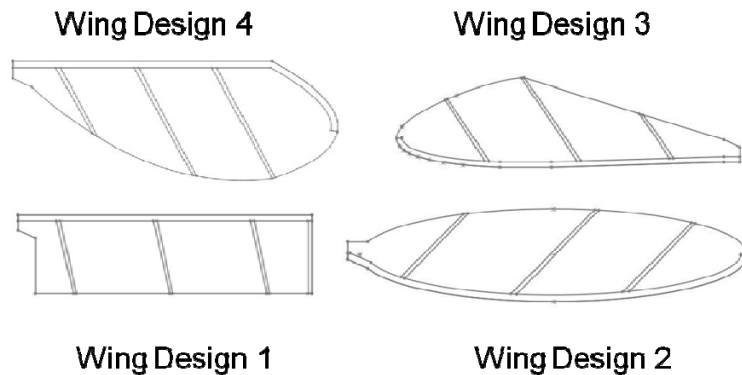


**Figure 15: SolidWorks Drawings for Wing Structure and Outline**

To ensure repeatability of cut components, an Epilog 30 Watt Fibermark Ytterbium air cooled laser operating at a wavelength of 1062nm is utilized. The proper speed, power and frequency settings of the laser must be determined to ensure proper cutting of the components. The variables in this process are speed, power and frequency. The primary consideration when determining these settings is cutting the material properly instead of simply ablating away material. Ablation occurs when the power settings of the laser are too high or the speed is too low and the laser dwells over a specific point for an improper duration. As a result, ablation causes the cut edges to char with an inconsistent distribution of remaining surface material. To counteract these negative effects, numerous passes by the laser must be utilized to obtain a clean cut.

In determining the proper settings, a test shape was chosen and then cut. This process is semi-empirical through noting which settings achieve the desired result but ultimately relies on trial and error. Once settings for one pass are found to not simply burn the material being cut, the number of passes to cut through the material is determined. In performing these experiments, using the highest power to speed ratio is desired since the duration to cut the material will be minimized. In determining the optimal settings for the laser, there presumably are other combinations that would work, but once a clean cut is achieved in an acceptable amount of time, those settings are then used.

Optimal cut settings were found for one-layer Kapton plastic which serves as the wing membrane and one-layer of unidirectional prepreg uncured carbon fiber, which provides the wing structure. These settings are listed below.

**Table 4: Epilog Laser Settings**

| Material | Power | Speed | Frequency | Passes |
|---|---|---|---|---|
| Kapton | 4 | 10 | 1 | 9 |
| 1 Layer Unidir PrePreg Uncured Carbon | 11 | 10 | 20 | 16 |

The process of taking a file drawn in SolidWorks, to cutting it on the laser requires a few intermediary steps. First, the specific SolidWorks files are saved as 2D drawings using the .DWG format and consist of a wing membrane outline and wing structure outline. The software used to interface with the laser is CorelDraw. Using the default import settings, the complex geometry of the wing outline and structure for the various wing designs is imported into CorelDraw. The CorelDraw files for the rectangular wings are shown below.
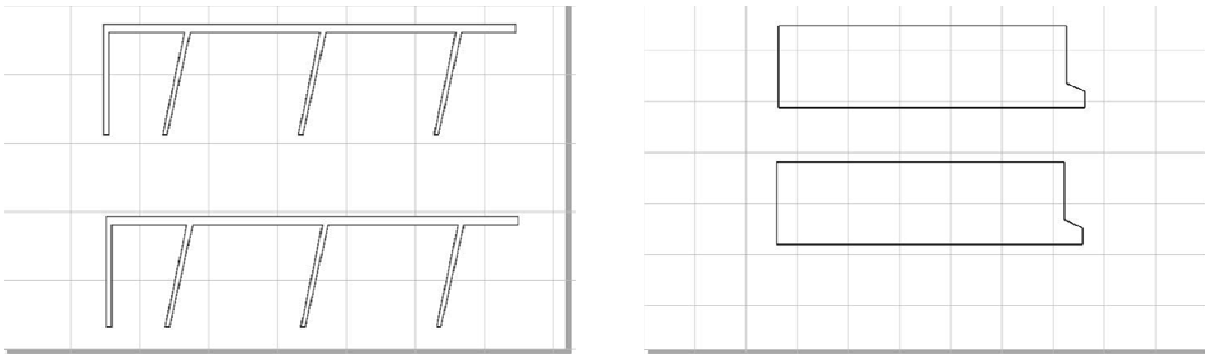


**Figure 16: Wing Design 1 CorelDraw Files**

With the necessary settings to cut the Kapton while using Wing Design 1 outline, experimentation can begin to determine the best procedure for cutting the desired shape. The Kapton was initially cut by taking a sample from a roll which is assumed to have uniform thickness, and then placed onto a glass plate for cutting. The Kapton was in no way secured to the glass plate but its inherent static properties were relied upon for it to lie flat on the glass pane.

In cutting the Kapton, inconsistencies developed with the laser not cutting through the entirety of the material evenly. Some places would have a nice clean cut, while others experienced significant superficial charring indicating improper cutting. Upon further inspection, it was discovered that the Kapton was not lying very flat on the glass plate and would wrinkle as the laser cut through it ultimately affecting the focus of the laser. To alleviate this problem, an additional glass plate was laid over the Kapton causing it to lie flat through the entirety of the cutting process. An additional glass plate was used since the laser energy would pass through it with little dissipation or damage to the glass. Prior to cutting, the laser must be focused on the cutting surface. With the addition of a second glass plate, the laser remained focused on the Kapton and not on the top glass plate. The previously determined settings also did not have to be changed. This new method proved extremely effective and resulted in near 100% consistency in cutting the Kapton for the wing membranes.

A similar layup is used to cut the carbon fiber. The uncured prepreg carbon fiber is stored in a freezer prior to cutting. A sample is then cut and placed onto a glass plate. Due to the epoxy in the prepreg carbon, the carbon sticks to the glass plate resulting in a flat cutting surface. This adherence is excellent for cutting the carbon, but will prove to be a nuisance when trying to remove the cut pieces from the glass pane as discussed in 3.1.3 Wing Manufacture Method Two Revised. Since this particular carbon is unidirectional, the entire wing structure, as a continuous piece of carbon cannot be cut. The carbon has stiffness parallel to the direction of the fibers and therefore must be cut in that direction. The main wing spar and individual veins are taken from the CorelDraw file and oriented parallel to each other as shown in the figure below. The carbon fiber is the

cut using the Epilog laser and aforementioned settings. Once cut with the laser, the components are removed from the glass pane using an X-ACTO knife. Like the Kapton, cutting the carbon in this manner produces near 100% consistency in getting a suitable cut.
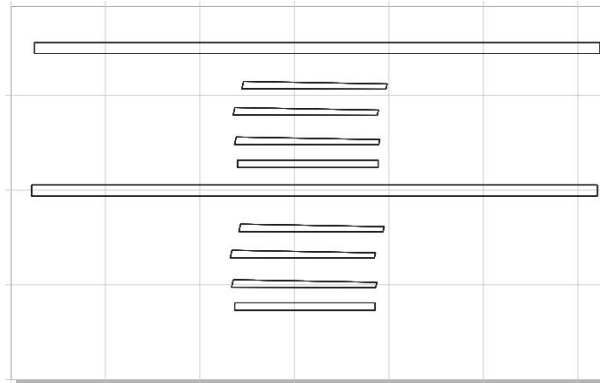


**Figure 17: Wing Design 1 Structure CorelDraw File**

With methods to cut the wing components, the next challenge becomes how to properly assemble the wings. The rectangle wing design is used for this purpose since its design makes it the easiest to cut and assemble. To this end, the SolidWorks drawing file with the wing structure overlaying the wing outline is printed to scale. This is placed under a piece of Teflon, which is semi-transparent. The wing structure components are then placed over the Teflon in their proper places as shown by the drawing. In this phase of manufacturing, the wing veins overlap the main spar producing a lap joint. With the structure in place, the Kapton outline is placed over the carbon. Similar to initial manufacturing, the wing is placed between two aluminum blocks tightened with nuts and bolts and placed in an oven to cure. The curing time history is shown in Figure 18. In essence, the oven ramps up at 2.5 °F/min until it reaches 350°F where it stays for 2 hours.
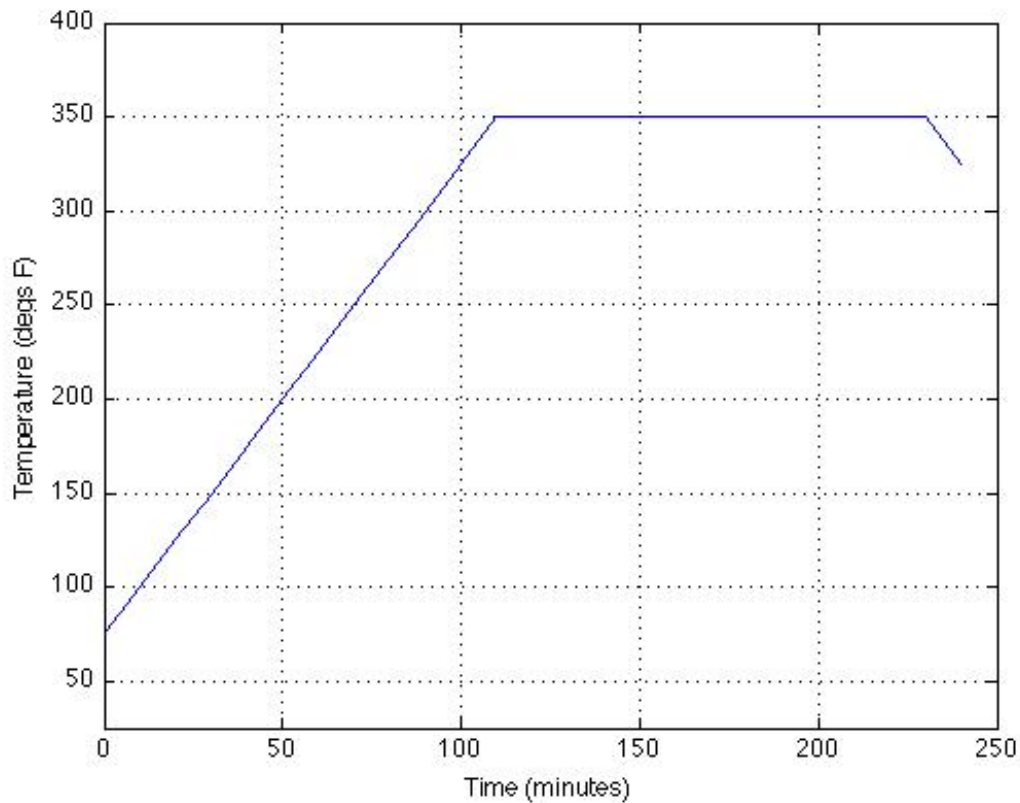
**Figure 18: Carbon Curing Temperature Profile**

This method was a very rudimentary step forward and proved to be exhausting and extremely time consuming. The natural adherence of the prepreg carbon aided in getting the lap joints to hold, but nothing was really holding the overall structure in place. Thus, the carbon components would repeatedly move out of proper position, especially when the Kapton was applied. This process was attempted several times with an average of one rectangular wing being assembled per hour (excludes cutting time of components). This process did provide greater repeatability, but allowed for significant variance in component placement.

36

### 3.1.2  Wing Manufacture Method Two

To solve the problem of the carbon components moving during placement, wing molds are used to assemble the wings. Using a quarter inch aluminum plate, individual 100mm x 50mm blocks were cut using a water jet. As with Method One, initial experimentation would begin with the rectangular design. The Epilog laser is again utilized to cut the prescribed mold into the aluminum. The settings to cut the aluminum were found in the user's manual and are Power = 100, Speed = 20, and Frequency = 20.

The exact same CorelDraw files used to cut the wing components are used to create the mold. The initial mold consisted of two passes for the wing outline and 5 passes for the wing structure. The five passes for the wing structure is determined through ease of placing the carbon components. A raster cut is used for the wing outline and wing structure. Figure 19 shows the mold for Wing Design 1.



**Figure 19: Wing Design 1 Aluminum Mold**

After cutting, the mold is cleaned with acetone and then mold release wax is placed inside the grooves and buffed with a cloth. The grooves are cleaned with a Q-tip. The rectangular wing carbon fiber components are then placed inside the mold and

overlaid with the Kapton wing outline. At this point, a butt joint is used between the wing veins and main spar to allow for a more even height of the carbon pieces. Nitrile gloves are worn during assembly to mitigate the effects of the tackiness of the carbon. This method is found to be more effective at holding the carbon components in place, but placement of the components is still very time consuming. Method Two allows for 2 rectangular wings to be assembled per hour.

Although a repeatable method to assemble the wings had been developed, after curing, only about 50% of the wings were viable due to issues with the carbon structure fully adhering to the Kapton. This problem was alleviated by gluing the carbon to the Kapton after curing, but then eliminated the repeatability aspect of the wing. Further refinement then of this method is required to improve the consistency of producing a testable wing.

### 3.1.3  Wing Manufacture Method Two Revised

Upon examination of the rectangle mold with carbon components already placed, it became apparent that the individual carbon pieces where not lying consistently flat in the mold. It was then believed that this was the explanation for the inconsistency of the carbon adhering to the Kapton. Thus, a reverse outline mold was made to push on the carbon. This mold was creating by using the laser to raster the entire area of an aluminum block except for the outline of the wing itself. The reverse and original molds are shown in the Figure 20.

**Figure 20: Reverse Wing Design 1 Aluminum Mold**

Using the reverse mold during assembly to push on the carbon did aid in getting the carbon to stay in place, it did not however meet its intended purpose. The carbon continued to sporadically adhere to the Kapton. It was then proposed that the grooves for the carbon were too deep. While allowing for greater ease in assembly, it appeared the carbon and Kapton did not consistently touch due to groove depth. The ability to precisely measure how much material the laser was cutting off with each pass was unavailable and thus calipers accurate to 1µm are used. It was determined that the laser was taking off 25µm per pass and that the grooves were in fact too deep. Knowing the thickness of the carbon fiber components to be 80µm, new molds are made using only three passes to achieve a depth of 75µm. Additionally, only one pass of the wing outline is performed as well. The new molds only proved slightly more effective at creating wings than the previous. The problem of the carbon not fully and consistently adhering to the Kapton persisted. The variability in the process now turned from assembly to curing.

The flat plate placed over the mold was secured using two 2" C clamps. The force applied by these C clamps would vary from curing to curing. To solve this problem, 7/16" holes were drilled into the molds and top plates. Quarter-inch hex cap screws and

corresponding nuts were used to secure the top plate to the mold. The nuts were then tightened using varying degrees of torque as applied by a torque wrench with torques values of 40, 50, 60 ft-lbs being applied. This setup is shown in Figure 21.
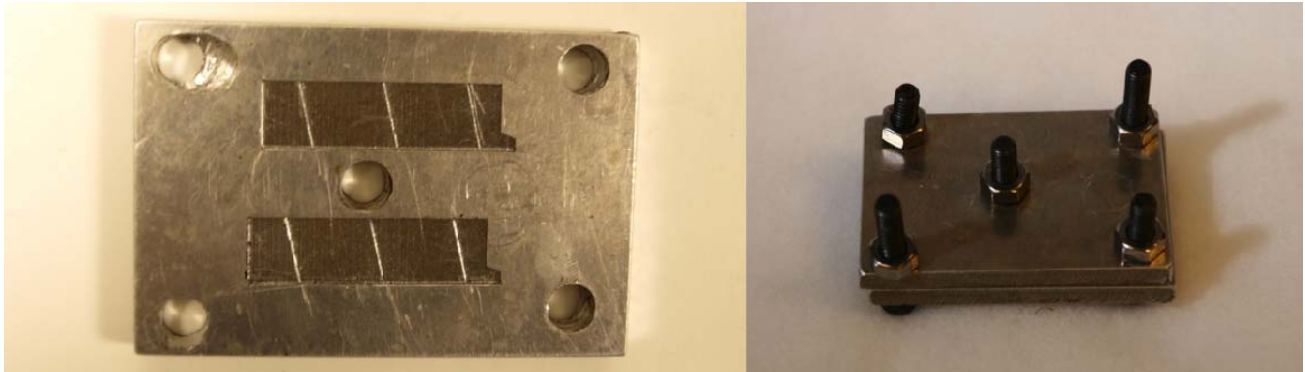


**Figure 21: Wing Design 1 Aluminum Mold with Holes**

There was no improvement in results. Only about 50% of wings cured were actually testable without requiring repair after curing. It was concluded that the variability in the manufacturing process is not a result of the process itself, but the variance of the epoxy in the prepreg carbon. It was reasoned that in some spots of the carbon there is more epoxy than others, which is why the carbon was sporadically adhering to the Kapton. Thus, an additionally adhesive membrane was needed to place between the prepreg carbon and the Kapton.

Additionally, at this point in the manufacturing process, all four wing designs were being assembled which lead to other significant issues. While cutting the one-layer unidirectional uncured prepreg carbon, it was found that due to the inherent tackiness of the carbon, it would adhere to the glass plate it was cut on. Although the cuts themselves were very clean and repeatable as seen by holding the glass plate up to a light source,

removing the curved spars of Wing Designs 2-4 from the plate became problematic. The

curved spars were weakest at the ends due to the orientation of the carbon. Combined

with the adherence of the carbon itself, many of the tips of the spars would break off

during removal.

The first method to alleviate these effects was to simply place the carbon in the

freezer to cool after cutting and then remove the pieces with an X-Acto knife. Using this

method, the curved main spars inconsistently would break at the curved tips. This fact

was simply accommodated by cutting more spars from Designs 2-4 than needed

assuming a 50% failure rate.

Additionally, in cutting the dramatic tip curvature of Design 4, it was found that

unidirectional carbon could not structurally support a design with much of the curvature

running perpendicular to the fiber direction. The straight main spar and curved end were

then divided into separate pieces aligned accordingly in the direction of the fiber. This

modified layup is shown below along with the other carbon fiber structure for the one-

layer wings. The upper left is for Wing Design 1, upper right is Wing Design 2, lower left

is Wing Design 3, and lower right is Wing Design 4.
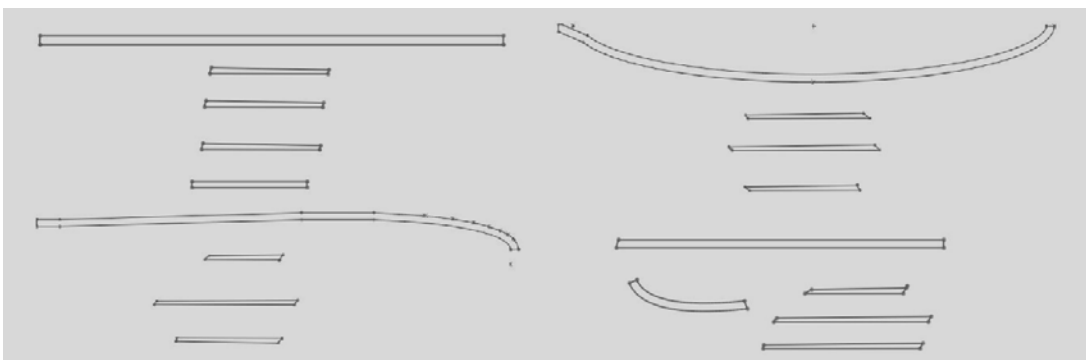


**Figure 22: Carbon Structure for One-Layer Wings**

The straight spar of modified Wing Design 4 was easily cut as expected. However, the separate curved portion of the main spar experienced many of the same problems as the other curved spars with tip breakage. With the requirement of an additional adhesive membrane, new practices would have to be developed to successfully remove the curved main spars as discussed in the next section.

### 3.1.4 Wing Manufacture Method Three

The adhesive membrane selected to place between the prepreg carbon and Kapton is Pyralux sheet adhesive (see www.dupont.com). It essentially consists of an adhesive engineered not to run at high temperatures with a paper backing. Initially, it is assumed the assembly process would consist of cutting the carbon components as before and Pyralux separately. To continue to ensure repeatability in the cutting process, the Pyralux is also cut with the Epilog laser. In this, a sample with the paper backing is placed on a glass plate. Like with the Kapton, to ensure the Pyralux lays flat, an additional glass plate is placed over its surface. However, cutting the Pyralux in this manner simply does not work. Unlike the Kapton, which resists melting at high temperatures, the Pyralux does not. Thus, as the laser energy passes through the top glass plate some of the energy is dissipated into heat. This heat is transferred to the surface of the Pyralux and results in charring and inconsistent cutting. Placing a secondary glass plate over the Pyralux is abandoned and instead it is simply taped to the underlying glass plate.

This method proves to be very effective at cutting the Pyralux when the following settings are used: Power = 12, Speed = 5, Frequency = 1, Passes = 1. However, once the

Pyralux cut is removed from the paper backing, it becomes extremely flimsy. Trying to place this flimsy membrane over the carbon structure in the mold becomes seemingly impossible and an alternative method is developed.

Instead of cutting the carbon and Pyralux separately, it is proposed to cut them simultaneously. The problem becomes creating one membrane. To solve this, a sample the same size as the carbon sample is cut from the Pyralux roll. The adhesive sheet is removed from the paper backing and placed over the prepreg carbon, which is already slightly adhered to a glass plate. The adhesiveness of the prepreg is again utilized by pushing with an aluminum block over the Pyralux, which then slightly adheres to the carbon. To achieve a more consistent membrane, a Weller WHA 900 Heat Gun is used to heat the Pyralux and essentially melt it to the carbon. Using a temperature of 1000°F and an initial fan speed of 0.5 and application angle of 0 to 45 degrees, the heat gun blows a steady stream of air onto the Pyralux. Once a white and black speckled membrane results, heat is applied at 90 degrees with a fan speed of 3 ramped up to 5. Heat is applied until the Pyralux changes color from a light cream to a yellowish cream. The desired carbon components are then cut from this membrane using the same laser settings to cut the carbon as before.

It was found that using the same cutting process as mentioned previously, the results improved slightly for the delicate ends of the curved main spars. This resulted from the Pyralux providing some additional strength in the direction perpendicular to the carbon fiber orientation. However, the results were not as repeatable as desired as components would still break while being removed from the glass plate.

Up to this point, the carbon/Pyralux membrane had been cut Pyralux side up with the tackiness of the carbon used to ensure the membrane lays flat on the glass pane surface. The solution then becomes the elimination of the carbon adhering directly to the glass surface. By placing the carbon/Pyralux membrane carbon side up and then placing the glue adhesive paper backing under the carbon, the tackiness of the carbon is no longer an issue. The difficulty is getting the Pyralux to thoroughly adhere to the carbon.

If the carbon were simply placed on a glass pane with the Pyralux placed over and treated with the heat gun, the carbon/Pyralux membrane would strongly adhere to the glass pane. Removing this layup from the pane essentially ruins the membrane, as it does not naturally want to be removed. Thus, the membrane is heat treated on a sheet of silicon in which the carbon does not adhere. This layup is then taped carbon side up to a glass plane with the glue adhesive paper backing acting as an intermediate layer between the membrane and glass pane. This entire process is shown Figure 23. Figure 23 A shows the Pyralux and prepreg carbon, Figure 23 B shows the Pyralux/carbon membrane, Figure 23 C is the layup on the glass pane, Figure 23 D is the individual carbon components with the Kapton membrane, Figure 23 E shows the carbon components in the mold, Figure 23 F is the addition of the Kapton membrane, Figure 23 G is the clamping style, and Figure 23 H is the final result with two Wing Design 1 wings.
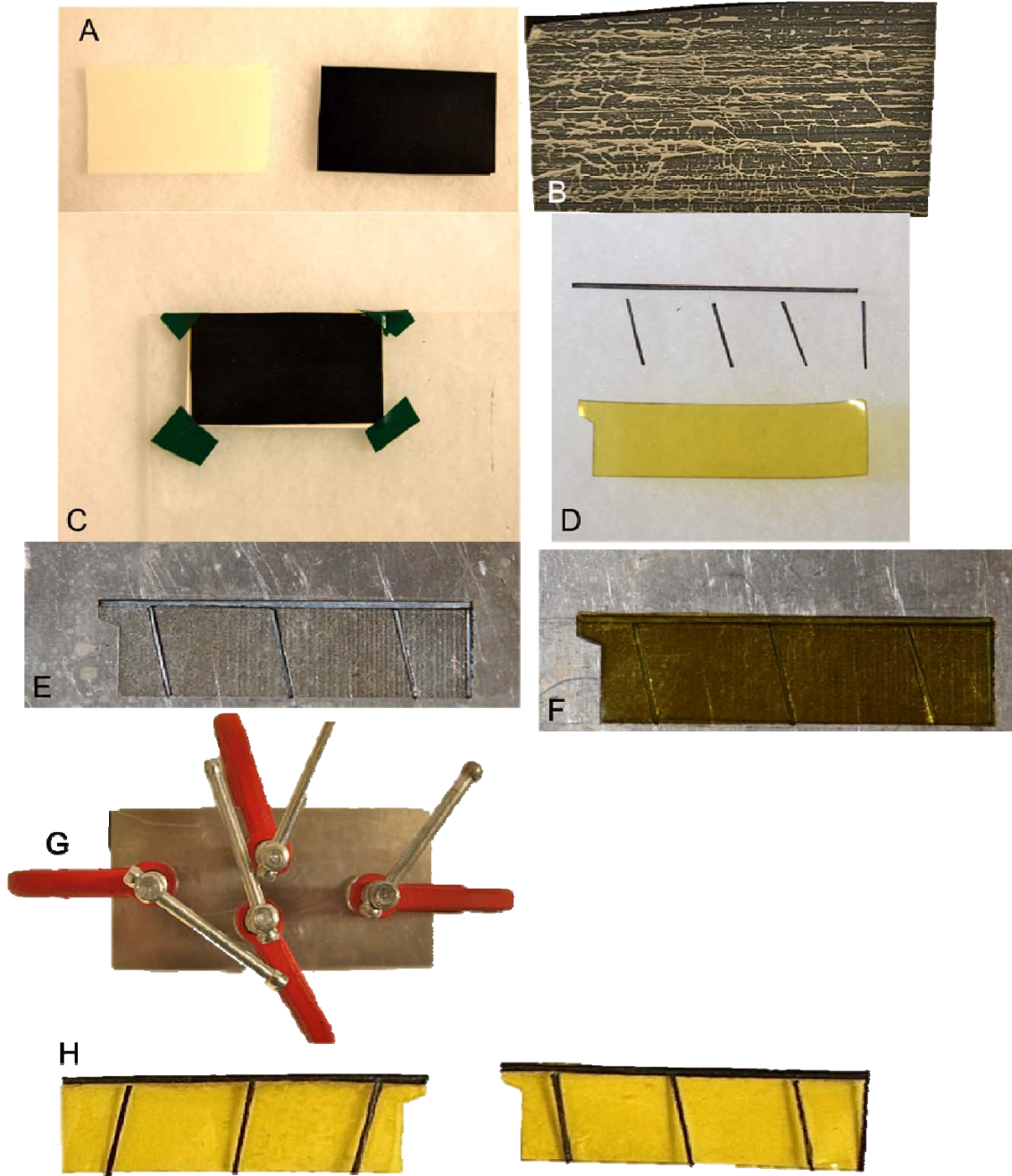
**Figure 23: One-layer Unidirectional Uncured Prepreg Carbon Layup**

This modified layup produces desirable results with very little tip breakage of the curved spars. Surprisingly, the veins have to be removed more delicately than with previous methods. Cutting the carbon in this manner produces consistent and repeatable results with extremely minimal re-cutting of wing structure components required.

To ensure the depth of the mold structure is no longer an issue, new molds are made with one rastered pass by the laser of the wing outline and one pass by the laser for wing structure. This results in an approximate wing structure depth of 25μm. The mold, as before, is pretreated with mold release wax. Additionally, a flat plate is again used to apply pressure to the carbon, Pyralux, and Kapton during curing and is also treated with mold release wax. This wax is applied each time to both the mold and top plate prior to curing. The plates must be thoroughly buffed otherwise wax residue will contaminate the Kapton and add useless mass to the wing. The entire assembly is secured using 4 2" C clamps and placed into an oven to cure.  This refined manufacturing process produces a near 100% success rate of testable wings with the carbon and Kapton adhering with very high consistency. These techniques produce extremely repeatable wings with an assembly time of approximately 1 hour for 12 wings.

### 3.1.5  Wing Manufacture Method Four

The previous wing manufacture methods have all pertained to one-layer of unidirectional uncured prepreg carbon fiber. The next techniques described pertain to the manufacturing of three-layer cured carbon fiber wings.

Three layers of 80μm unidirectional prepreg carbon are cut from a roll and oriented at 0°- 90°- 0°. The properly aligned layers are placed onto an aluminum plate

covered with a sheet of porous Teflon placed over a sheet of non-porous Teflon, the

carbon layup is covered with one sheet of porous Teflon, and the entire plate is wrapped

in non-porous Teflon and taped in the middle of the carbon layup (see www.dupont.com

for more information on Teflon). This layup is placed under vacuum and cured for 4

hours in an autoclave at a constant 100psi. This autoclave is located at the AFRL

Materials Lab. The carbon is cured using essentially the same cycle as shown in Figure

18. This process is shown in Figure 24.
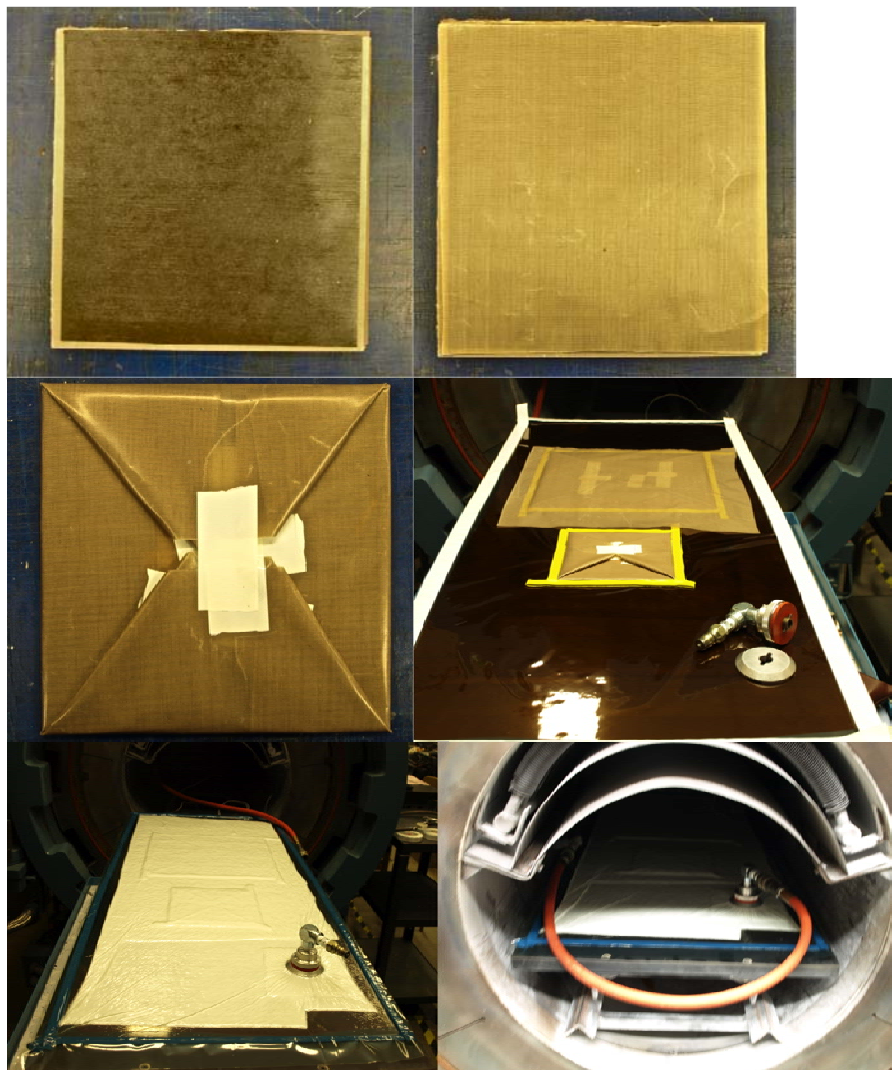


**Figure 24: Three-Layer Carbon Curing Process Layup**

With the cured carbon, techniques must be developed to not only cut the carbon itself, but also to properly place the Pyralux glue adhesive. As previously mentioned, once cut and the paper backing removed, the Pyralux wing structure outline becomes extremely difficult to place in the aluminum molds due to its flimsiness. The first solution attempted was to simply adhere the Pyralux to the carbon with a heat gun similarly to Method Three. The only difference from Method Three is that more heat is required since the cured carbon is not as permeable as the uncured carbon used in Method Three. The carbon/Pryalux membrane is then taped to a glass plate and cut Pyralux side up. A clean consistent cut is achieved with this method, but since 75 passes with the laser are required to cut through the carbon, much of the Pyralux has ablated on the veins at this point. The second solution was to simply flip the membrane over with the carbon side up. Cutting the membrane with this method produced inconsistent cutting results. Since the Pyralux comes in contact with the glass plate, charring around the edges again results and much of the Pryalux is still ablated away as the glass heats up.

Knowing that the Pyralux does not burn to its paper backing when cut, the final solution was to adhere the Pyralux to the carbon as before with the heat gun, and cut the membrane with carbon side up. However, rather than having the Pyralux contact the glass, it contacts the paper it was removed from. Thus the top layer is carbon, then Pyralux, then the paper backing as with Method Three. This entire layup is then taped to a glass plate and placed under the laser for cutting with the following settings: Power = 5, Speed = 10, Frequency = 1, and Passes = 75. The entire layup process is shown in Figure 25. Figure 25 A shows the Pyralux paper backing, Pyralux, and cured three-layer carbon, Figure 25 B shows the Pyralux/carbon membrane, Figure 25 C is of the entire layup on

the glass plate, Figure 25 D is the excess Pyralux/carbon while Figure 25 E is the cutout

of Wing Design 4, Figure 25 F shows the placement of the cutout onto the Kapton, Figure

25 G is of the clamping setup, and Figure 25 H is the result with two three-layer wings of

Wing Design 4.
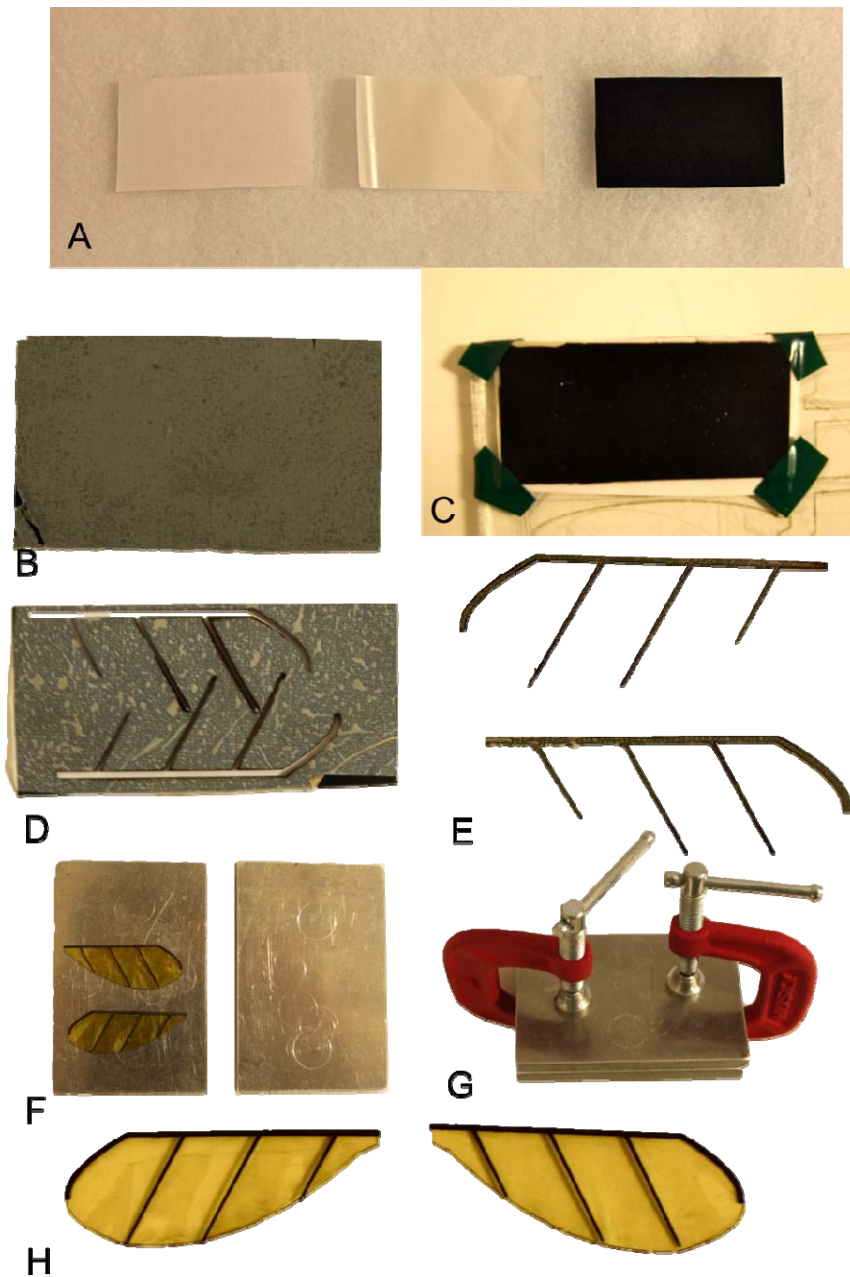


**Figure 25: Three-Layer Cured Carbon Wing Layup Process**

This method produced very consistent cutting with a few caveats. It is imperative that the Pyralux essentially be melted onto the carbon and turned from a cream to a yellowish color when heat is applied. This ensures the Pyralux is thoroughly adhered to the carbon. Additionally, once cut with the laser, the cut out must be removed promptly to allow for a clean removal from the excess carbon/Pyralux membrane. It was found that if these procedures were not followed, the Pyralux would adhere to the excess around the cut and leave gaps in the adhesive on the carbon. Following all these steps, an excellent three-layer carbon with Pyralux backing structure could be cut very consistently with a near 100% success rate.

To assembly a three-layer wing, two methods are attempted. First, 2 flat plates of aluminum are treated with mold release wax. The cut out carbon structure is then placed onto one of the plates. The Kapton outline is placed over this structure. This technique does produced testable wings, but unwanted wrinkling of the Kapton does occur. To mitigate this, the Kapton is applied to the aluminum plate first. Due to the static properties of the Kapton, it lies very flat on the plate. The carbon structure is then placed by hand over the Kapton. Since the carbon outline and Kapton are both cut very precisely, proper alignment can occur without the use of molds. This method virtually eliminates any wrinkling of the Kapton, and produces a highly repeatable and relatively easy to assemble FWMAV wing.

Although more time is required to cut the components of the three-layer carbon wings, its ease of assembly makes it superior to the one-layer carbon wings in manufacturability only. Repeatability testing will determine though which method is ultimately more consistent.

50

### 3.2 Transducer Validation Testing Procedures

The force and moment transducer utilized for this research is the ATI Industrial Automation Nano-17R (www.ati-ia.com). This transducer has three primary components: Net F/T Transducer, Transducer Cable, and the Net Box. The Net F/T Transducer measures forces and torque loads, converts these loads into electrical signals, and relays this analog signal over the Transducer Cable. The Transducer Cable also provides power to the transducer itself. The Net Box is used to power the transducer and acts as the interface between the transducer and a computer. Since this transducer outputs an analog signal, an analog-input version of the Net Box is used. An Ethernet cable is plugged into the Net Box and into the computer used for data acquisition and post processing. The components are shown in Figure 26.
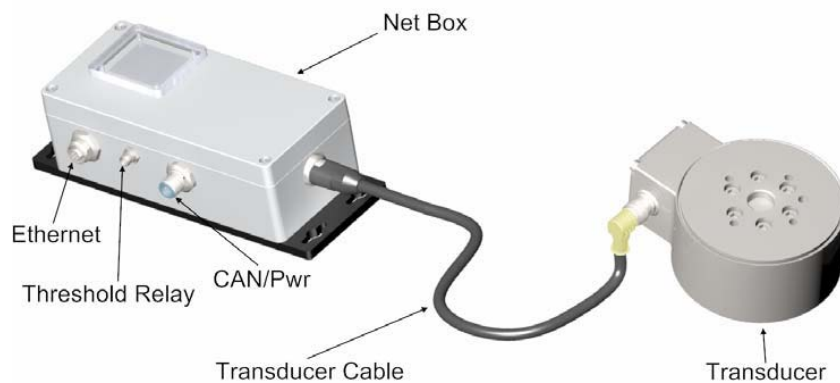


**Figure 26: Nano-17R System Components (www.ati-ia.com)**

This particular transducer is typically used in automated robotics applications to measure the load's the wrist of a robotic arm experiences during operation. Although not specifically intended to measure mN forces, the manufacturers specifications deem it

possible to do so. The manufacturers specifications for this transducer are summarized below.

**Table 5: Summary of Nano-17R Sensing Properties (www.ati-ia.com)**

|  | Fx | Fy | Fz | Tx | Ty | Tz |
|---|---|---|---|---|---|---|
| Sensing Range | 12N | 12N | 17N | 120N-mm | 120N-mm | 120N-mm |
| Resolution | 1/320N | 1/320N | 1/320N | 1/64N-mm | 1/64N-mm | 1/64N-mm |

As a result of the resolution of this force transducer being 3.125mN and the expected measured forces in the millinewton range, validation needs to occur to quantify the uncertainty of the measurements, determine axis interactions, and characterize the signal noise. This validation will therefore ensure greater reliability of the results and that this transducer is suitable to measure the minute forces generated by FWMAV.

Validation utilized three known weights 9.8mN, 19.6mN, and 98.1mN or 1 gram, 2 grams, and 10 grams respectively. This validation only characterized the forces applied, as only the forces obtained during flapping would be analyzed. For flapping motion testing, the positive x-axis will point upward, the positive z-axis will point toward the wing, and the positive y-axis completes the right-hand rule. Thus, the x-axis will measure lift and the z-axis will measure drag. The axes for validation testing are aligned such that the positive of the axis being tested points upward.

The rapid prototype apparatus used to test the flapping motion is also used for validation. Pieces are also rapid prototyped to hold the weights and interface with the transducer. The weight holders and transducers interface pieces are all specifically designed for proper axis alignment so that each weight acts along one axis. The top of

Figure 27 shows the transducer without the transducer interface while the bottom shows

the transducer with the interface.
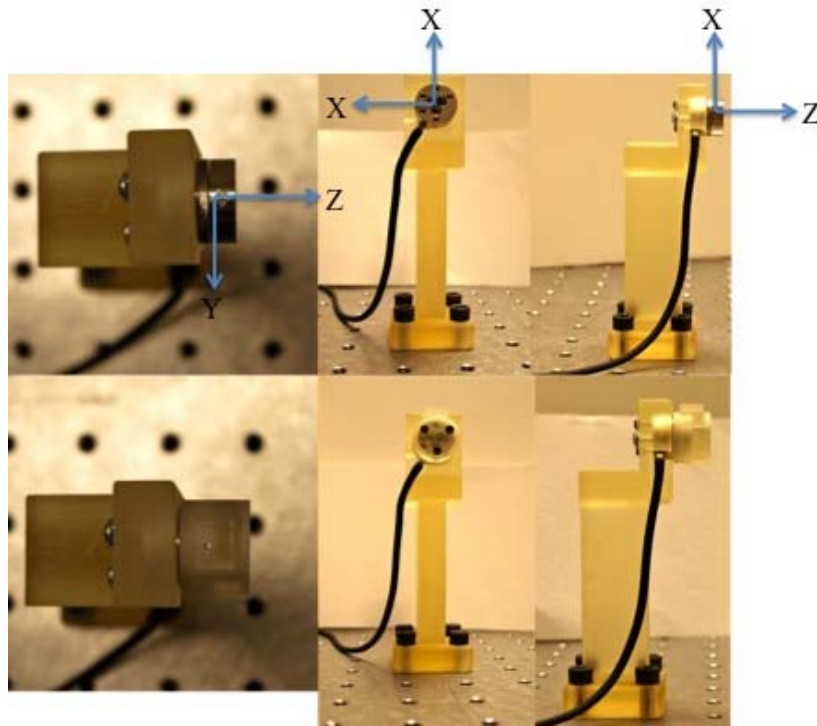


**Figure 27: Transducer Validation Setup**

The transducer interface shown in the bottom half of Figure 27 is the same one

that will be used for flapping tests. Two other transducer interfaces are required to

properly align the axes for testing. All three are shown in Figure 28 with the x-axis

interface on the left, y-axis in the middle and z-axis on the right. The x and y axis

transducer interfaces are both rigidly attached to the transducer with 3, 2mm diameter hex

cap screws. The z-axis interface uses a slip fit attachment with 0.5mm tolerance.

X-Axis    Y-Axis    Z-Axis

**Figure 28: Transducer Interfaces**

The rapid prototype pieces with and without the weights are shown in Figure 29. These pieces interface with the transducer apparatus using a slip fit with 0.05mm tolerances.
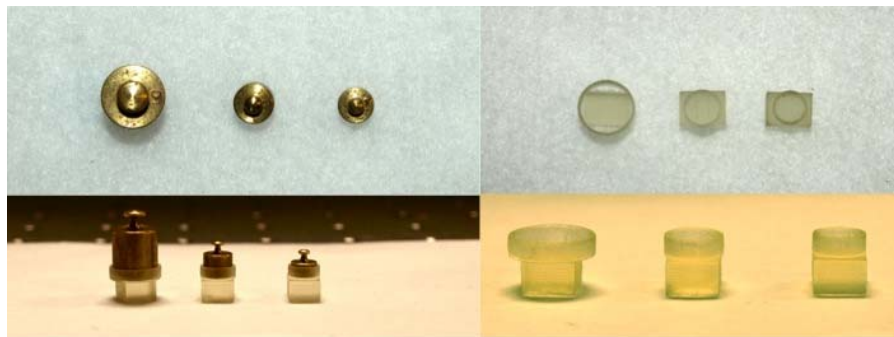


**Figure 29: Weight and Weight Holders**

Each validation test conducted consisted of a tare and then actual test where the weight is placed in the weight holder. Each phase consisted of a sample taken at 1kHz for approximately 20 seconds. The values from the tare test are averaged and the tare average is then subtracted from each test value. This counts as one test. Table 6 below summarizes the testing schedule. The 30 1g tests are actually broken into 3 sets of 10 tests. Only one set of 10 tests is presented in the results for each respective axis while all 30 tests are used to compute uncertainty and quantify signal noise. Additionally, examining the tare and consequent test values for the axes where the force is not directly

applied, that is, looking at the y and z axes while Fx is being applied etc, will be used to determine if axis interactions are occurring. If axis interactions are in fact taking place, there should be significant differences between the tare and test values for the axes not being validated.

**Table 6: Summary of Validation Testing Procedures**

| X-Axis | | | |
|---|---|---|---|
| Mass | 10g | 2g | 1g |
| Number of Tests | 10 | 10 | 30 |
| Y-Axis | | | |
| Mass | 10g | 2g | 1g |
| Number of Tests | 10 | 10 | 30 |
| Z-Axis | | | |
| Mass | 10g | 2g | 1g |
| Number of Tests | 10 | 10 | 30 |

It was noted that during testing, that when a new setup is completed, i.e. going from the x-axis setup to y-axis setup, the recorded values tended to drift. Thus, the balance is allotted approximately an hour between setups to equilibrate. This greatly improved the consistency of the results and is also applied during wing testing.

For each test completed, the interface box attached to the transducer via an Ethernet cable, provides force and torque values in terms of counts in a .csv file. A Matlab mfile is written for post processing of each data set which coverts the measured values into forces and moments while accounting for the tare of each respective axis.

For the purposes of computing statistical data for each data set, the following equations are used to compute mean, standard deviation, and normalized standard deviation.

Mean
$$\bar{x} = \frac{1}{n}\sum_{i=1}^{n} x_i \qquad (8)$$

Standard Deviation
$$s = \left(\frac{1}{n}\sum_{i=1}^{n}(x_i - \bar{x})^2\right)^{\frac{1}{2}} \qquad (9)$$

Normalized Standard Deviation
$$z = \frac{s}{\bar{x}} \qquad (10)$$

## 3.3 Laser Vibrometer Testing Procedures

With repeatable wing manufacturing techniques, validation of the repeatability of

wing dynamics can now be evaluated. Although wing dynamic response covers a wide

range possible of testing procedures, the first three structural dynamic modes of a wing

are determined for comparison and analysis. The wing modes are found using a Polytec

PSV 400-3D laser vibrometer with built-in data management system with data collected

at 2kHz (www.polytec.com/psv3d).

A 0.25V band-limited white noise input signal is input to a Bogen HTA-125 High

Performance Amplifier, which results in an input frequency from 0 to 0.4 kHz with a

bandwidth of 0.78125 kHz. This signal is then relayed to a Briel and Kjaer DK-2850

Naerum shaker. A wing is clamped at its tip and then secured to the shaker using a nut.

The dynamic response was measured at four test points. One point is placed at the tip of

the screw protruding from the shaker where the wing clamp is secured. This point moves

with the shaker and acts as a reference point. Three points are then determined for each

wing. For continuity between the testing of each wing, the points are placed in the same

positions relative to the wing structure. That is, one point is placed at the tip of the middle

wing vein (Point 1), while the other two points are placed at the wing spar and vein intersection of the top (Point 2) and bottom veins (Point 3). Four wings of each design and type were tested using the laser vibrometer. Figure 30 shows the testing setup for the 1-layer carbon Wing Design 3 wing.
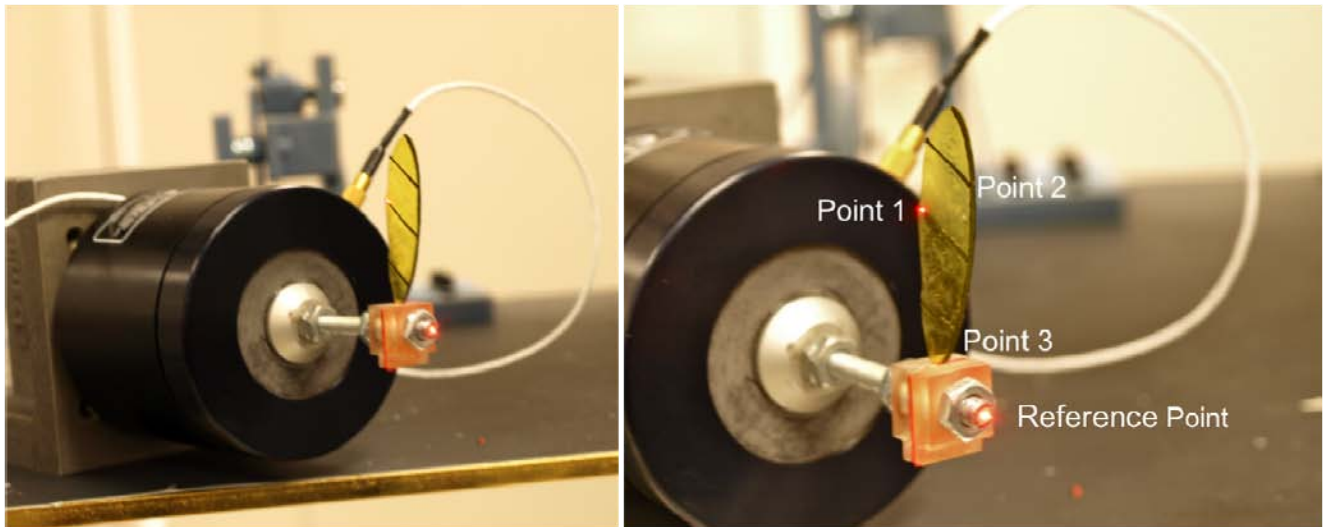


**Figure 30: Laser Vibrometer Setup**

The laser vibrometer determines the wing's natural frequencies at these specific points only, which is then assumed to be the global modes of the individual wing. During testing, the various resonant frequencies for each test point were essentially equal with only magnitude varying. Test Points 2 and 3 are then used for comparison purposes only to Point 1 to ensure continuity among the values. However, between changing the tested wing of the set being tested, the three test points are utilized to ensure the wing is positioned the same way in the clamp as the previous wing with only very minor corrections being made to Points 1-3 on the respective wing. This process produces greater standardization between wing testing especially in how the wing is secured in the clamp. If a wing is placed lower or higher in the clamp as compared to the other wings,

this would affect the vibrational response of the wing as the cantilevered boundary condition of the wing would be altered. This in turn would affect the vibrational response of the wing. Since the frequency response data collected between the various test points is essentially the same, only data at test Point 1 is presented.

During testing, 10 tests are performed and averaged. Within the Polytec data management system, a frequency response function (FRF) is generated by taking the ratio of the average output response collected by the laser vibrometer to the average input excitation voltage to the shaker. The laser vibrometer determines the output response by measuring the change in velocity of the 3 test points as compared to the reference point. The peaks of the FRF are the natural frequencies (modes) of the wing. Additionally, during testing a coherence plot is generated to ensure the quality of the data collected. The FRF data is saved to a text file and then imported into Matlab. For simplicity, the bounds of the peaks are manually inputted into a Matlab mfile, which then uses the max command to find the magnitude peak and corresponding frequency. Figure 31 shows a representative FRF plot with the data between the red o's representing the bounds to find the max values. The frequency peaks as mentioned previously are the modes of the respective wing and what are presented in the results section.
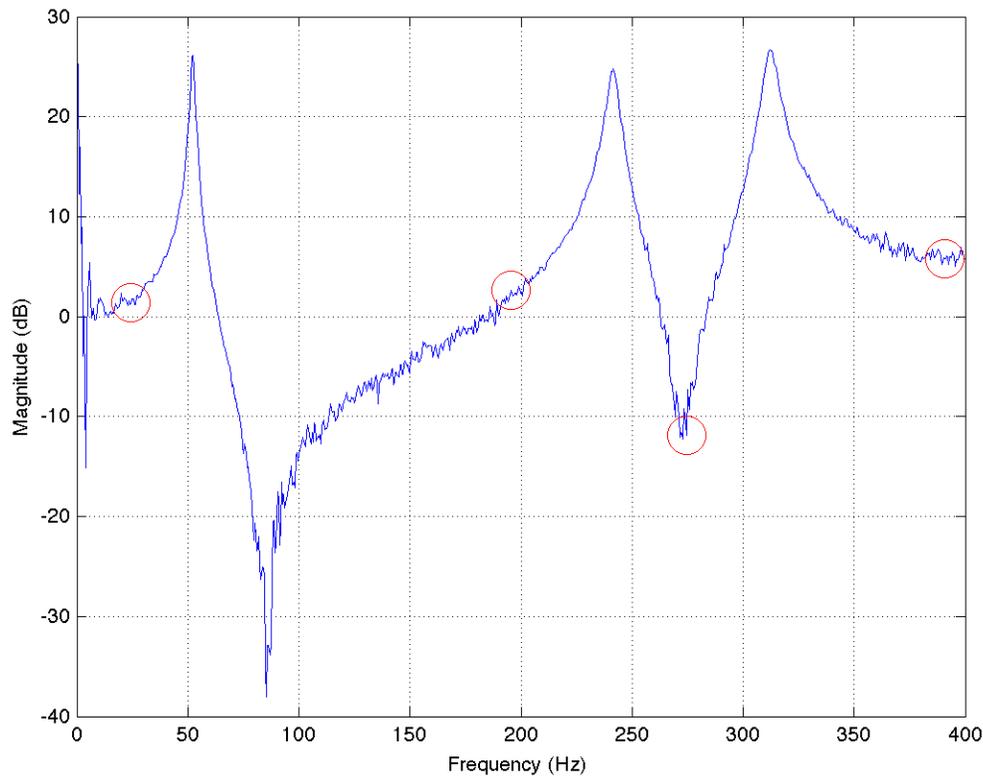
**Figure 31: Example Frequency Response Function with Bounds**

## 3.4  Micro Air Vehicle Wing Testing Procedures

### 3.4.1  Wing Flapping Mechanism

With wings ready for testing, a pivotal step in their testing is a flapping mechanism capable of flapping, with wing attached, at a frequency close to the resonance of the wing. Through previous research, the flapping motion performed by an insect can be reduced to crank-slider linkage. Through further simplification, a fourth link is used in place of the slider to create a simple four-bar mechanism. Substituting a PZT bimorph cantilever actuator (piezo) for the driving link in the four-bar mechanism, a piezo-driven

59

flapping mechanism results where amplitude and frequency can be varied through the
input voltage. Figure 32 shows the kinematics of this flapping mechanism.
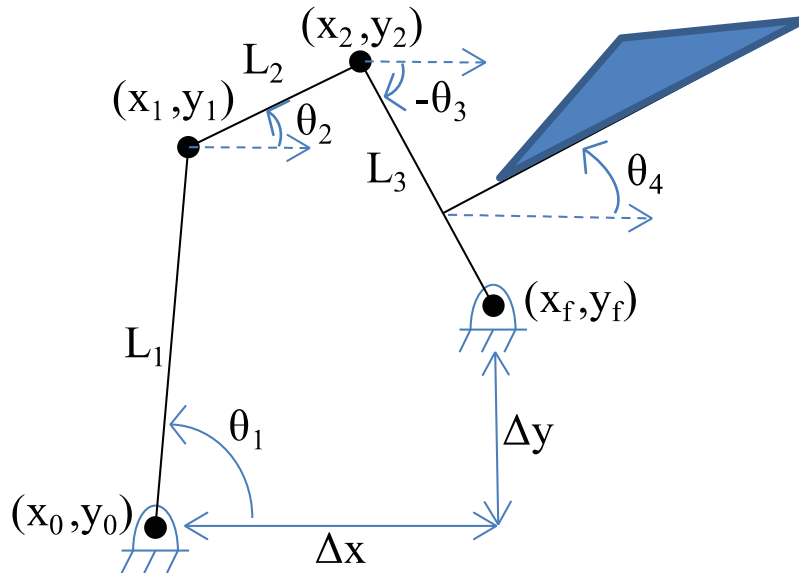


**Figure 32: Kinematics of Flapping Actuator Used for Wing Testing [1]**

This particular flapping mechanism is designed to have a maximum flapping
stroke of ±60°. The piezo actuator is an Omega Piezo, OPT 39.5/2.1/0.6 with the linkage
designed assuming a 1.0 mm piezo deflection. Equations were developed to represent the
motion of the flapping actuator and simulated in a Matlab mfile. The actuator deflection
simulation is shown in Figure 33.
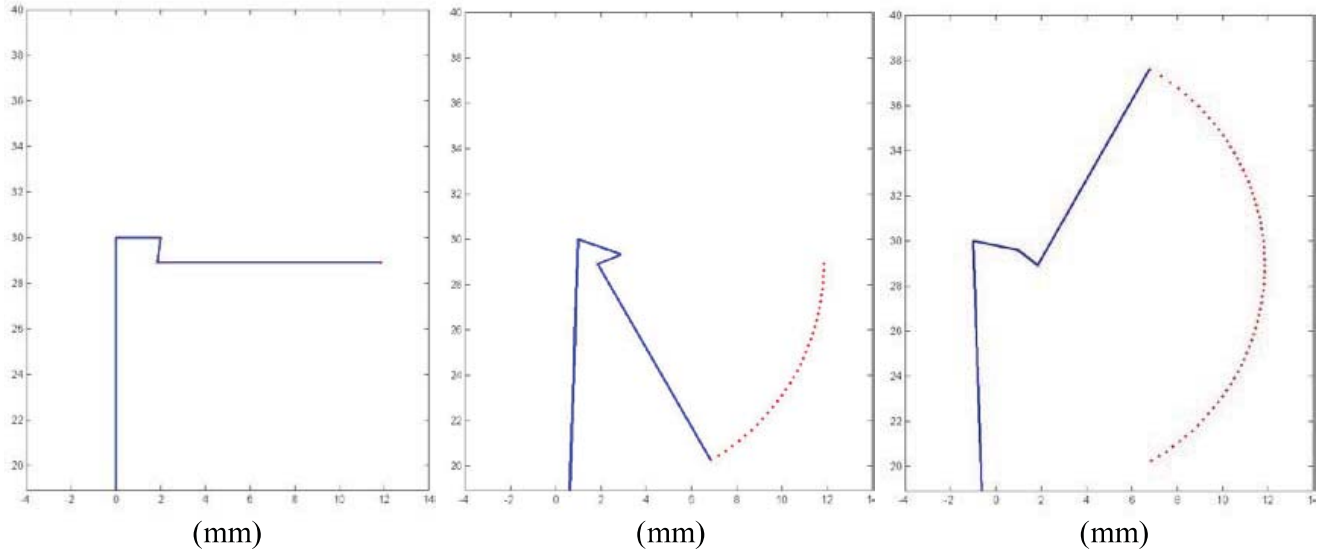
**Figure 33: Flapping Actuator Deflection Simulation [1]**

The linkages themselves consist of 100μm carbon fiber with the joint flexures created by sandwiching Kapton between two pieces of carbon fiber. Since the focus of this research was wing flapping and not the flapping mechanism itself, a general summary was given. For more information on the flapping mechanism please see [1]. The flapping mechanism used for testing is pictured in Figure 34.
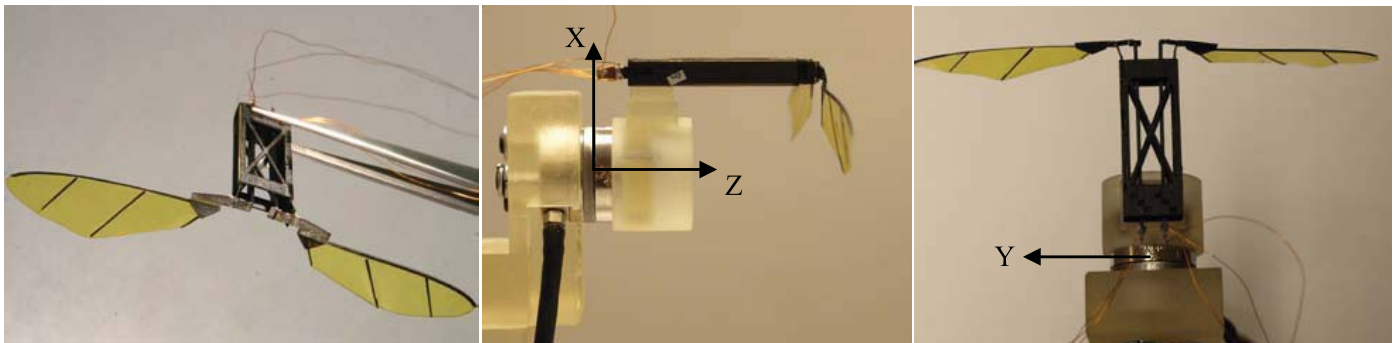


**Figure 34: Wing Testing Setup**

To generate sufficient forces which can be measured by the transducer being utilized, two flapping mechanisms are used to essentially double the applied forces.

### 3.4.2 Wing Testing

The wings are glued to the wing holder joints of the flapping mechanism using Cyano Acrylate super glue. Every effort is made to align each wing the same on each wing holder joint and ensure the mean chord of the wing is parallel to the ground.

Prior to collecting force data, initial vibration data must be collected. Using the same procedures as discussed in 3.3 Laser Vibrometer Testing Procedures on page 56, the first mode resonant frequency of the flapping mechanism with wing can be determined. This is then the first mode natural frequency of the system. The vibration response is measured at the wing holder joint as shown in Figure 35.
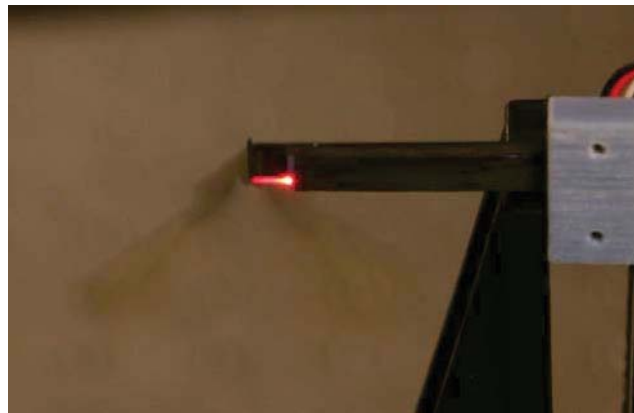


**Figure 35: Example Placement of Laser for Laser Vibrometer Testing to Determine System First Mode Resonance**

For simplicity, the first mode resonant frequency of only one flapping mechanism with wing is found and assumed to be the same resonant frequency for the other flapper

on the opposite side. This resonant frequency is then input into the Matlab wing testing mfile. This mfile creates an array with two parts. The first part varies the flapping frequency from 80% of first mode resonance of the system to 110% of first mode resonance of the system. Flapping amplitude is held constant for this portion. The second half of the array consists of varying amplitude from 85% to 100% of the amplitude used in the first half of the array. Flapping frequency during this portion is held constant at 110% of the first mode resonant frequency of the system.

Since Simulink will automatically linearly interpolate between array points, only the initial and final conditions of a particular test point have to be specified at a particular time. This array is loaded into a Simulink model. Within the Simulink model, a wing bias block is created. Prior to testing the wings with the test array, each individual flapping mechanism is connected to a signal generator. This generator is used to visually verify the first mode resonant frequency and determine if any bias in the input voltage is needed to obtain a symmetric flapping stroke centered around the tip of the piezo actuator. With determined bias values, the Simulink model is executed and then uploaded to dSpace. dSpace provides a computer based interface compatible with Simulink to convert from an analog to digital or digital to analog signal. The signal output from dSpace is relayed to a 30:1 amplifier, which connects to the flapping actuator. The Simulink model can be viewed in Figure 36.
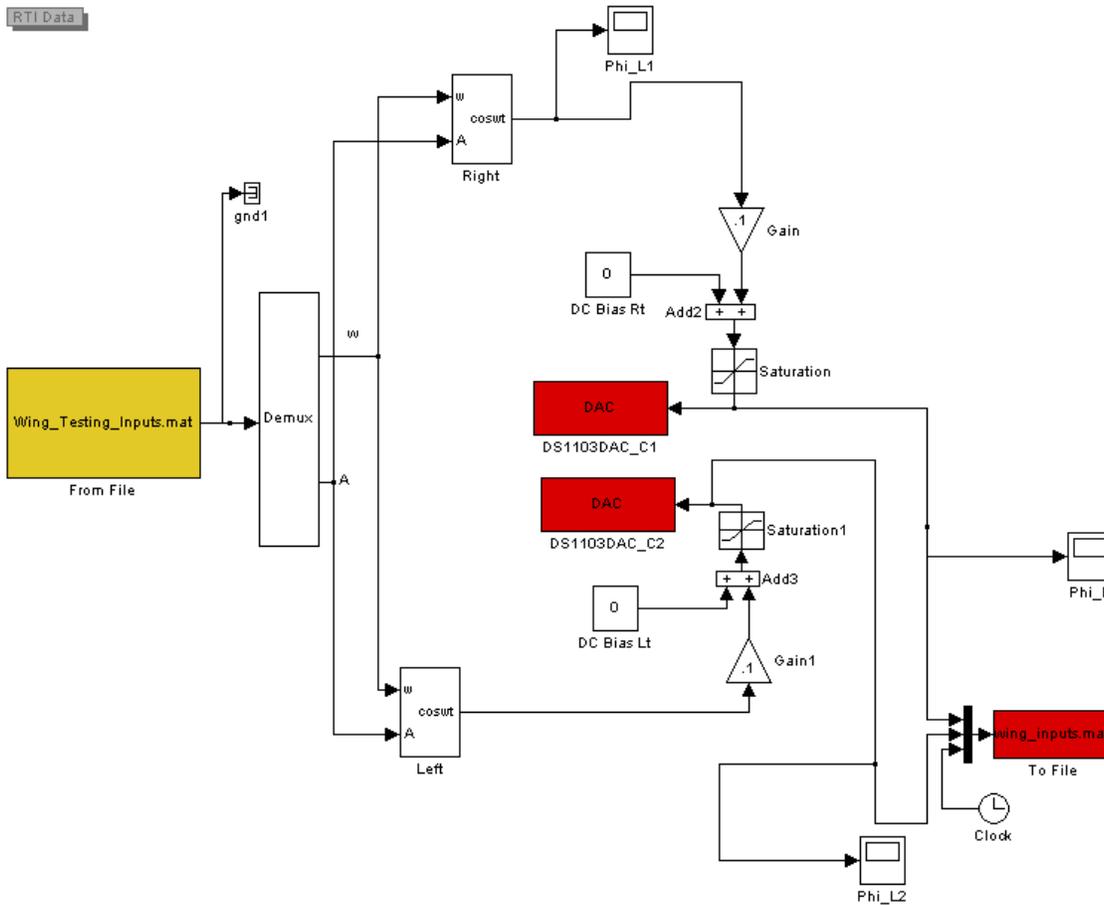
**Figure 36: Simulink Model**

To automate post processing of the data, known voltage, amplitude and frequency values at specific times must be known. This is why dSpace is used to send the input voltage to the flapping mechanisms as opposed to simply using a signal generator.

The dSpace signal input to the flapping mechanisms is shown in Figure 37 where x is time and y is amplitude or frequency. The ten second period of zero amplitude corresponds to where an initial tare is taken. Additionally, the periodic five-second zero amplitude points correspond to additional tares. Thus, a tare value is obtained prior to any flapping. This ensures better accuracy of the data.

64
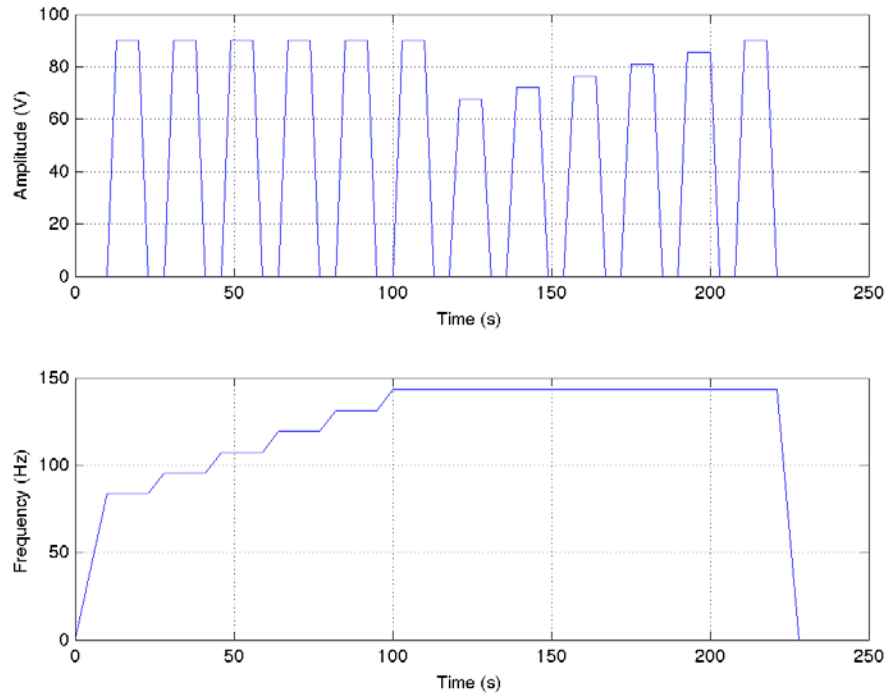
**Figure 37: Wing Testing Input Profile**

Data is collected at 1kHz using the ATI Nano-17R Transducer. Prior to running repeated tests under the same conditions for each wing, trial tests are run to ensure all the proper settings, specifically that first mode resonant frequency, is occurring. Resonance is when the wing should be flapping most efficiently with highest amplitude and thus generating the most lift or force in the x direction. With confirmation of maximum force generation at first mode resonance, consecutive testing can begin.

With a particular test set completed, a Weller WHA 900 heat gun is applied to the wing holder joint for approximately 60 seconds at 1000 degrees F at a fan speed of one. This the heats up the super glue, and the wing comes off easily with a X-ACTO knife. The wing holder joint is carefully sanded with 200 grit sandpaper, a new wing is glued

on, and the testing process repeats. Note there is no difference is testing procedures

between wing types.

<center>**Analysis and Results**</center>

## 4.1  Transducer Validation Results

### 4.1.1  Axis Interactions

A significant question that this validation hoped to answer was axis measurement interaction. Through looking at the measured tare values of the axes where a force is not being applied and the consequent measured test values of those same axes, one can compare the values to ensure they are approximately the same. Since each axis is theoretically solely measuring noise during validation of the other respective axes, two mean noise values can be obtained. These values correspond to Test 1 and Test 2. The data for this table comes from the 4.1.2  X-Axis Validation Results presented in the next sections. Table 7 shows that interactions are not occurring.

<center>**Table 7: Axes Interaction Summary**</center>

|  | Fx Applied | Fy Applied | Fz Applied |
|---|---|---|---|
| X-Axis Tare (mN) | 6.684 | -0.287 | 0.769 |
| X-Axis Test Value (mN) | -2.766 | 0.039 | 1.136 |
| Difference (mN) | -9.451 | 0.326 | 0.590 |
| Y-Axis Tare (mN) | -0.105 | 0.244 | 0.606 |
| Y-Axis Test Value (mN) | 0.301 | -9.261 | 0.919 |
| Difference (mN) | 0.406 | -9.505 | 0.313 |
| Z-Axis Tare (mN) | 0.323 | -0.286 | 1.571 |
| Z-Axis Test Value (mN) | -0.038 | -0.330 | -8.357 |
| Difference (mN) | 0.361 | 0.054 | -9.928 |

Since the values are changing in the fractions of mN range, one can assume that very little axis interaction is occurring and that the variation is due to signal noise. With this result, the signal noise can then be quantified which is presented in the 4.1.6 Quantifying Signal Noise section.

### 4.1.2  X-Axis Validation Results

As mentioned previously, the x-axis of the transducer will be used to measure lift. Quantifying the uncertainty of the measured values in this axis is crucial to having confidence is the presented lift values. In Figure 38 below, the measured values for the 1g test are shown. The blue x's represent a data point for each test while the red dashed line is the expected value of -9.81mN.
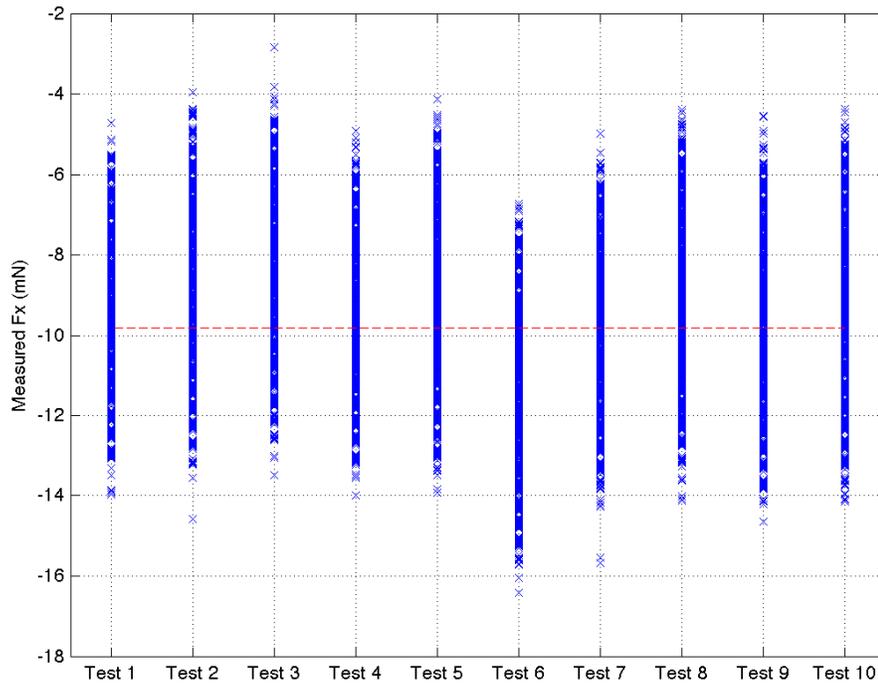


**Figure 38: X-Axis Validation Measured Fx**

As expected, the measured values are generally centered on the expected value line. The broad range of values of approximately 10mN can be attributed to the sensing range of the transducer itself. Since the applied force is only 3x the minimum sensing range value, variation is expected. What is crucial though is the average of these measurements and the consistency therein.  Table 8 lists the average of each test and the associated percent error from the expected value.

**Table 8: Summary of X-Axis 1g Validation Fx Values**

|         | Average (mN) | Percent Error (%) |
|---------|--------------|-------------------|
| Test 1  | -9.40        | 4.09              |
| Test 2  | -8.86        | 9.73              |
| Test 3  | -8.57        | 12.63             |
| Test 4  | -9.61        | 2.07              |
| Test 5  | -9.10        | 7.23              |
| Test 6  | -11.39       | 16.11             |
| Test 7  | -9.78        | 0.29              |
| Test 8  | -9.03        | 7.94              |
| Test 9  | -9.75        | 0.56              |
| Test 10 | -9.45        | 3.66              |

These ten tests produce an overall average measured force of -9.50mN, which corresponds to a percent error 3.16%. Although there are obvious outliers in the data, taking an average over several tests does produce positive results. Wing testing will take place in the same manner where several tests will be averaged to increase reliability.

The standard deviation of the data is also analyzed. A favorable standard deviation ensures that despite outliers being measured, the data set as a whole is mostly comprised of values close to the mean. Table 9 shows per data set, the percentage of data between one and two standard deviations.

**Table 9: Summary of X-Axis 1g Validation Standard Deviations**

|         | One SDev (%) | Two SDev (%) |
|---------|--------------|--------------|
| Test 1  | 68           | 95           |
| Test 2  | 70           | 97           |
| Test 3  | 70           | 95           |
| Test 4  | 69           | 95           |
| Test 5  | 67           | 95           |
| Test 6  | 66           | 95           |
| Test 7  | 70           | 95           |
| Test 8  | 68           | 96           |
| Test 9  | 69           | 96           |
| Test 10 | 65           | 95           |

Looking at the 10 tests collectively, 68% of the data is within one standard deviation of the mean while 95% is within two standard deviations; statistically speaking, these are both good values and suggest that the data is normally distributed. From Table 8 and Table 9 it can then be concluded that this transducer can accurately resolve approximately 10mN with consistency and reliability in the x direction.

The other two axes for the 1g x axis validation are now analyzed. The plot below shows the measured force values as represented by the blue x's with the red dashed being the expected value of zero. Any measured value in this case can be assumed to be predominately signal noise since the weight is aligned with the x axis of the transducer. This is confirmed in the 4.1.6  Quantifying Signal Noise section. This data will then help to quantify the noise of the transducer.
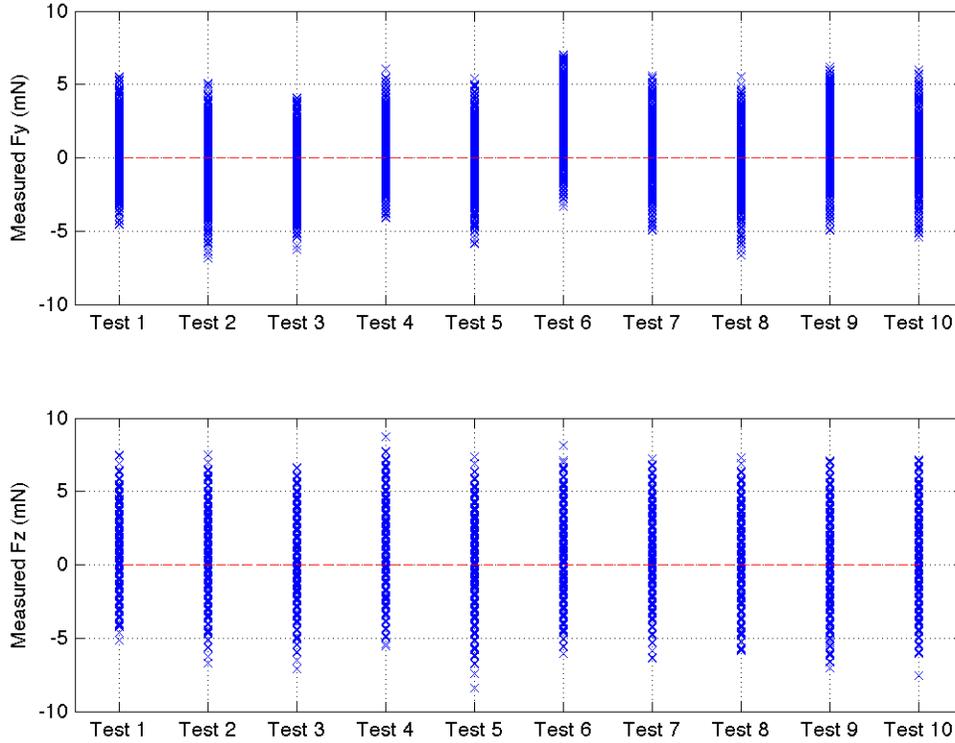
**Figure 39: X-Axis Validation Fy and Fz Measured Values**

The measured values are generally centered on the expected value of zero. Assuming no axis interactions, the noise for the axes not being validated can be obtained. The table below shows the average value from each test.

**Table 10: Summary of Force Measurements for the Y and Z Axes**

|         | Fy (mN) | Fz (mN) |
|---------|---------|---------|
| Test 1  | 0.14    | 1.17    |
| Test 2  | -0.89   | 0.82    |
| Test 3  | -0.69   | 0.62    |
| Test 4  | 0.68    | 1.45    |
| Test 5  | -0.15   | 0.34    |
| Test 6  | 2.04    | 1.12    |
| Test 7  | 0.53    | 0.99    |
| Test 8  | -0.45   | 0.62    |
| Test 9  | 0.90    | 0.49    |
| Test 10 | 0.26    | 0.66    |

71

The average noise in the y direction is then 0.24mN while the average noise in the z direction is 0.83mN. These values are both significantly below the sensing threshold of the transducer itself of 3.12mN by a factor of 13 and 4 respectively. Since one of the primary concerns in testing FWMAV is producing force values above the noise threshold, this data provides encouragement to that affect. Looking at the data from the 2g and 10g, similar noise values are obtained. In the y-axis, the average measured noise was 0.33mN and 0.19mN respectively while for the z-axis, the average measured noise was 0.65mN and 0.21mN for the 2g and 10g tests.

With the increase in mass for the 2g and 10g tests, the percent error went down significantly as expected for the measured values in the x-axis. For the 2g tests, the average measured value percent error dropped to 2.04% while for the 10g tests, the average dropped error dropped to 0.13%. Normalizing the standard deviations using the expected mass, the variability in the data was also reduced as the mass increased. For the 1g test, the normalized standard deviation was 0.26, for the 2g test 0.12, and for the 10 g test the normalized standard deviation was reduced to 0.025. Not surprisingly, as the force applied is increased, the transducer improves in resolving the values. Most importantly though, the transducer does consistently and with accuracy resolves 10mN of force in the x direction.

### 4.1.3  Y-Axis Validation Results

For wing testing, the y-axis will be measuring side force. Although not as pivotal as lift and drag, results should align with those of the other two axes. The plot below shows the results from the 1g tests when the mass is solely applied in the y direction. The

data looks very similar to that of the x-axis with better overall centeredness on the expected value of -9.81mN.
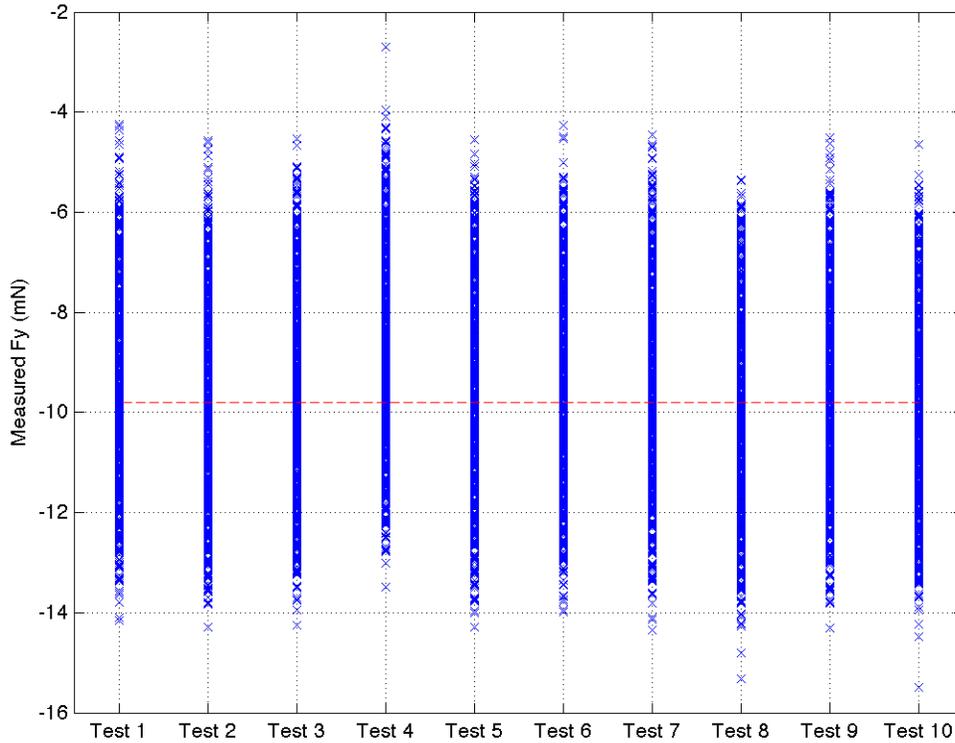


**Figure 40: Y-Axis Validation Measured Fy**

Looking at the actual mean values from each data set, the table below summarizes the results showing the percent error from the expected value as well. The average measured value for the y-axis validation is -9.79mN resulting in a percent error of 0.2%. The results of 1g y-axis validation are summarized in Table 11.

73

**Table 11: Summary of Y-Axis 1g Validation Fy Values**

|        | Average (mN) | Percent Error (%) |
|--------|--------------|-------------------|
| Test 1 | -9.69 | 1.20 |
| Test 2 | -10.07 | 2.67 |
| Test 3 | -9.94 | 1.32 |
| Test 4 | -8.95 | 8.72 |
| Test 5 | -9.79 | 0.20 |
| Test 6 | -9.70 | 1.16 |
| Test 7 | -9.68 | 1.34 |
| Test 8 | -10.19 | 3.84 |
| Test 9 | -9.80 | 0.15 |
| Test 10 | -10.15 | 3.43 |

This surprising accuracy variation could most likely be attributed to the balance being at a more equilibrated state either due to temperature variation or simply jostling caused by setup. When measuring such a small force, random variations in results are expected. The key to minimizing those variations is quantity of tests performed.

Looking at the standard deviation of the original data set, the standard deviation is very comparable to that of the x-axis 1g tests. The y-axis 1g tests had an average of 68% of the data within one standard deviation and 96% of the data within two standard deviations. This suggests that the spread of the data between axes is fairly consistent.

Examining the signal noise of the x and z axes, the plot below shows the measured noise from the 1g y-axis validation. As with the noise measured in the x-axis validation, the values are centered on the expected value of zero. The average of the x-axis noise is 0.50 mN while the z-axis average is 0.45mN.
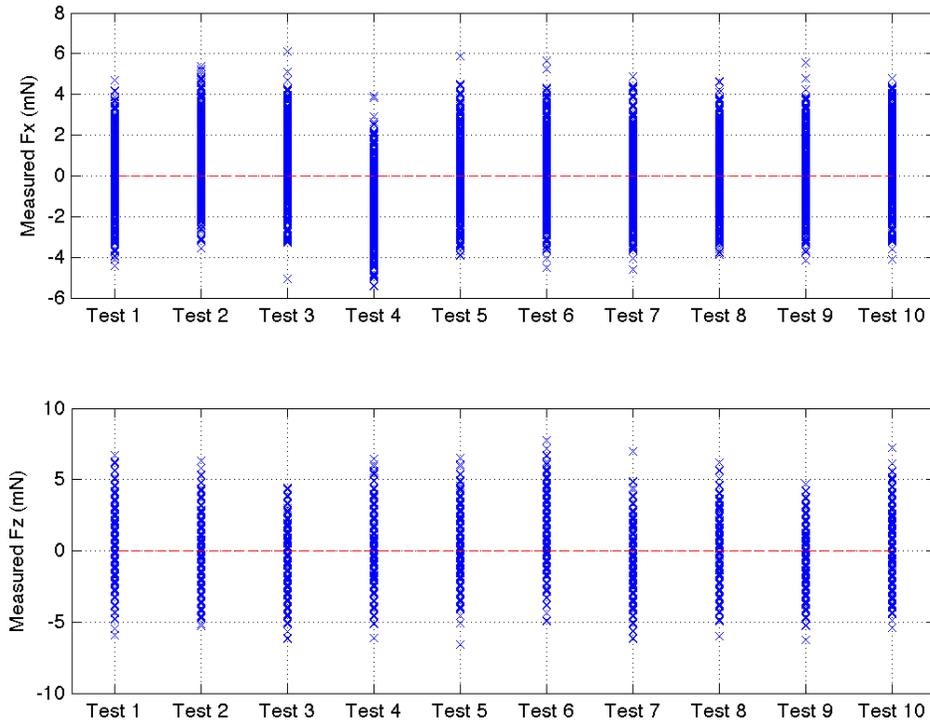
**Figure 41: Y-Axis Validation Fx and Fz Measured Values**

As with the x-axis validation values, these values are very encouraging in that the noise for this transducer is low relative to the expected force measurements in the millinewton range. This will then increase the overall confidence of the measured force values.

The accuracy of the y-axis actually decreases in the 2g and 10g mass tests. The averaged measured value for the 2g test is -19.34mN with a resulting percent error of 1.43%. With the 10g tests, the average measured value is -96.15mN and percent error of 1.94%. Since the 1g tests had a very low percent error, it somewhat skews the comparison to the other masses. The variation in percent errors speaks to the inherent

variation in measuring such small values. Minimizing outliers can only be achieved through repeated testing. A more thorough value for percent error from the 1g validation is obtained by analyzing all 30 tests as presented in 4.1.5  Measurement Uncertainty where the overall percent error is approximately 3.5%. Using this number, the deviation from the expected value for the 2g and 10g tests seems more reasonable.

### 4.1.4  Z-Axis Validation Results

The results of the 1g mass tests for the z-axis validation are very comparable to that of the x and y axes. The plot below shows the results of this test. One main difference between this data set and the others however is the discretization of the data shown by the white space between the groupings of x's. Upon further inspection, this trend does appear in the $F_z$ measurements for all testing regimes. It is so apparent in this figure because the figure is larger than the others. Since no filter is applied to any data set, the discretization is a result of the transducer itself.
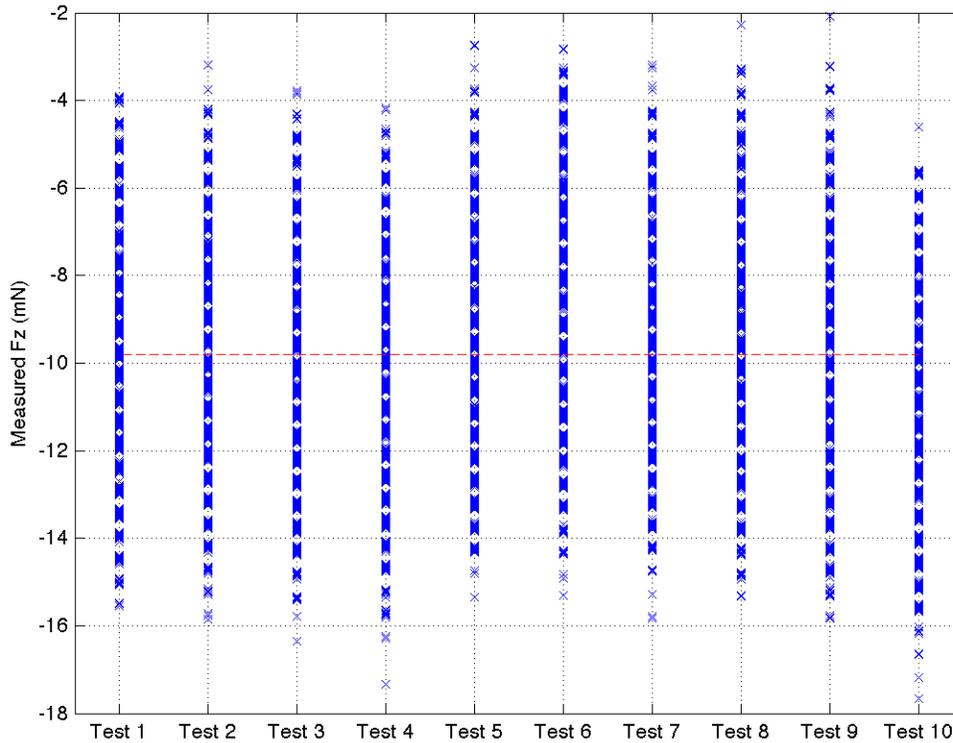
**Figure 42: Z-Axis Validation Fz Measured Values**

Upon inspection of the results of the 1g, it does appear that the discretization does not significantly affect the accuracy of the measured values. Table 12 summarizes the averages and percent errors from each test.

**Table 12: Summary of Z-Axis 1g Validation Fz Values**

|         | Average (mN) | Percent Error (%) |
|---------|--------------|-------------------|
| Test 1  | -9.62        | 1.87              |
| Test 2  | -9.76        | 0.45              |
| Test 3  | -9.94        | 1.40              |
| Test 4  | -10.39       | 5.30              |
| Test 5  | -9.29        | 5.31              |
| Test 6  | -8.80        | 10.24             |
| Test 7  | -9.40        | 4.19              |
| Test 8  | -9.50        | 3.15              |
| Test 9  | -9.86        | 0.51              |
| Test 10 | -10.96       | 11.70             |

This data set has an average Fz value of -9.75mN resulting in a percent error of 0.61%. This particular data seems to be comprised of a greater number of outliers than the comparable other sets. Since the outliers seem to be evenly distributed on around on either side of the expected value, a suitable mean value is still achieved.

More insight into the distribution of this data set can be gleaned from the standard deviation. As with the other data sets, this data is normally distributed with an average of 66% of the data within one standard deviation and an average of 96% of the data within two standard deviations.

It can then be concluded that the discretization of the data does not affect the mean value or the distribution of the values themselves. Thus the z-axis is suitable to measure drag. Looking at the signal noise during the z-axis validation of the x and y axes respectively, the average measured value is 0.59mN for the x-axis and 0.31 for the y-axis.

Finally, as expected, the accuracy of the measurements increases with applied force. With the 2g mass, the average measured value is -19.8mN with a percent error of 0.92%. For the 10g mass, the accuracy improves significantly with an average measured value of -9.98mN resulting in a percent error of 1.73%.

### 4.1.5 Measurement Uncertainty

The three important takeaways from this validation were variation in accurately measuring known forces, axis interaction in measuring those known forces and noise magnitude. Due to the inherent delicacy of the flapping mechanism, only 5 tests per wing set will be tested. Thus, uncertainty within an average of using only 5 tests must be determined. As shown in Table 6, 30 tests were performed for all the axes for the 1g

78

testing. To determine the uncertainty within 5 tests, a random number generator is created

which randomly selects 5 tests out of 30 and averages the error from the expected value

for those tests. This process is repeated until the mean of the average percent error

converges within 1E-9 using the following equation for convergence where $\bar{x}_k$ is mean of

the percent error up to trial k.

$$\left|\frac{\bar{x}_k - \bar{x}_{k+1}}{\bar{x}_k}\right| \tag{11}$$

The following plot shows convergence for the x-axis 1g validation test. The

average converged percent error is 5.134% with 16,077 trials to reach convergence.
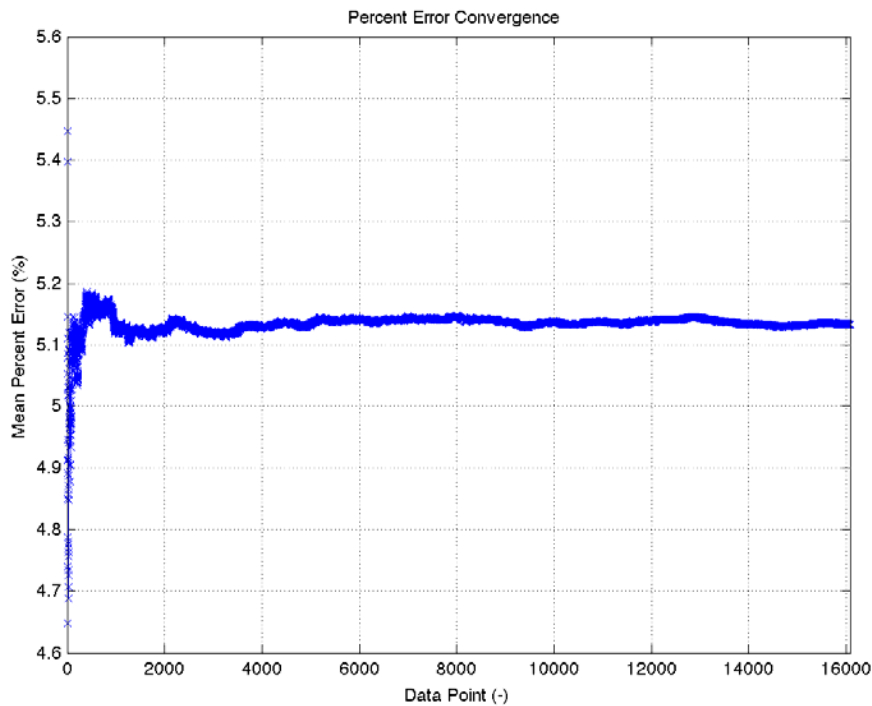


**Figure 43: X-Axis 1g Validation Percent Error Convergence**

This same process is repeated for the y and z axes respectively with the table below summarizing the results for the 1g validation testing.

**Table 13: Summary of 1g Validation Expected Percent Error**

|                        | X-Axis | Y-Axis | Z-Axis |
|------------------------|--------|--------|--------|
| Number of Trials       | 16,077 | 13,231 | 18,975 |
| Converged Percent Error| 5.13%  | 3.49%  | 5.00%  |

While the x and z axes are very comparable in their overall discrepancy from the expected force value, the y-axis is certainly more accurate. Looking at the data itself from the 30 tests, the y-axis has fewer outliers resulting in a lower overall percent error as compared to the other axes. The measured outliers ultimately distort the percent error for a given data set. The key to minimizing their effects is number of tests. Since wing testing is limited in the number of tests that can be performed due to the delicacy of the flapping apparatus, minimizing outliers is not an option through test quantity. The value of this table is then in that fact that if 5 tests are performed with forces ranging in the 10mN range, this is the uncertainty in each axis. This table does suggest that the y-axis will consistently produce the most accurate results and should therefore be used as the primary testing axis for future testing. Interestingly enough, despite the y and z axes having significantly lower percent errors for the 10 test previously presented, the overall percent errors are more comparable. This then reiterates the point that variation in the data and ultimately the results exists. Thus values can only be deemed accurate within some uncertainty bounds as computed above.

It should be noted that the entire process of computing a converged percent error is performed several times to ensure consistency of the results. Variation in the percent

error values occurs in the 2$^{nd}$ decimal place and thus the values shown Table 13 are deemed acceptable and statistically sound.

### 4.1.6 Quantifying Signal Noise

The process for computing the expected signal noise is the same as computing the percent error for each axis. Taking the force measurements from the various axes validations and using the data in the axes not being verified, an average signal noise value can be found. As before, trials are performed until the mean value converges within some specified realm. The convergence regime value used for the signal noise was 1E-8. Since the measured noise values are very small, obtaining convergence within the 1E-9 realm proved difficult. Despite this, variation of the noise values varies in the 3$^{rd}$ decimal place. Since each axis is solely measuring noise during validation of the other respective axes, two mean converged values can be obtained. These values correspond to Test 1 and Test 2.

**Table 14: Summary of 1g Validation Expected Noise**

|  |  | X-Axis | Y-Axis | Z-Axis |
|---|---|---|---|---|
| Test 1 | Number of Trials | 23,670 | 33,005 | 23,994 |
|  | Converged Noise Value (mN) | 0.153 | -0.193 | 0.071 |
| Test 2 | Number of Trials | 13,572 | 23,488 | 22,950 |
|  | Converged Noise Value (mN) | 0.516 | -0.355 | 0.311 |
| Mean Noise Converged Value (mN) |  | 0.334 | 0.274 | 0.191 |

The converged noise values are surprisingly well below the sensing range of the transducer which means that discernable measurements can be made in the mN range. The mean converged noise values for each axis are also comparable to each other.

To ensure that no electromagnetic interference is generating signal noise, a Fast Fourier Transform is performed on one test of 1g x-axis validation tare data for the x-axis. Figure 44 shows the result of the transform and that there are no conclusive peaks. This suggests that the signal is solely a result of the transducer and not outside electromagnetic interferences within the bandwidth of interest.
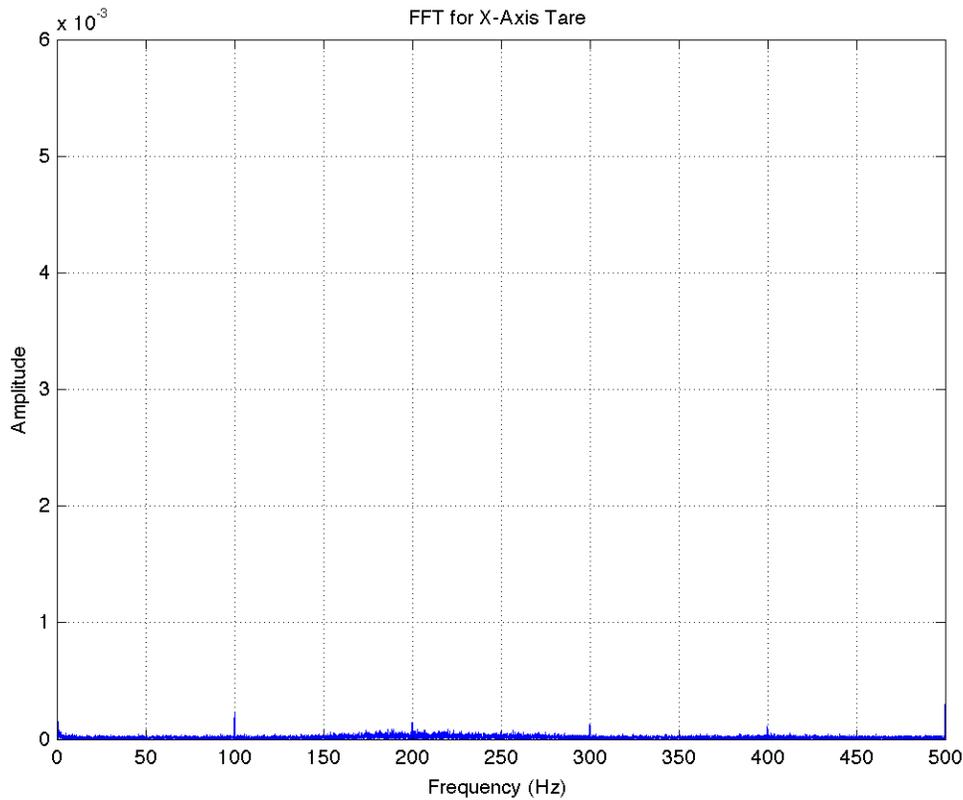


**Figure 44: Fast Fourier Transform X-Axis Tare**

Noise data is also collected with no force being applied to the transducer except the x-axis transducer interface. No tare is taken with raw data collected at 7kHz, which is the maximum collection rate of the transducer. The data is converted into forces in Matlab. This transducer utilizes a 16 bit A/D converter and has a maximum force load of

±12N. This equates to an A/D bit resolution of 0.3662mN. Figure 45 shows the first 50 data points collected. The error bars at each point correspond to the bit resolution. It quickly becomes apparent that all three axes are not meeting this minimum resolution. Looking at Fx and Fz, the jump between points exceeds the bit resolution for 40% of the Fx points and 50% for the Fz points. Conversely, for the y-axis, the minimum resolution between points is exceeded 15%. This data cites the fact that the transducer is consistently dropping a bit for the x and z axis data. With this information, the greater accuracy of the y-axis is explained. The manufacturer was unable to provide a concrete rational behind the dropping of bits. However, since the transducer is accurately resolving 1mN worth of force, this issue was not deemed detrimental to the results as a whole.
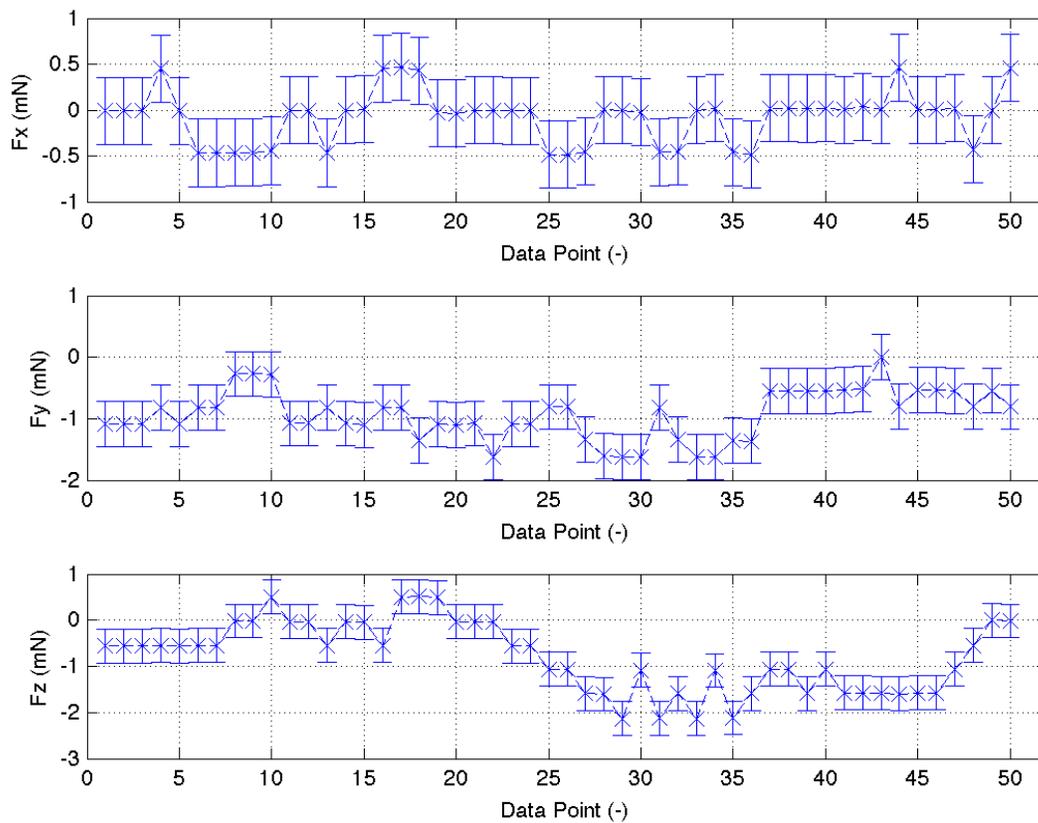


**Figure 45: Noise Data Collected at 7000 Hz**

### 4.1.7  Transducer Validation Conclusions

The conclusion that axis interactions are not occurring along with Table 14 and Table 13 form the crux of this validation since the primary concerns are axis interactions, deviation from expected value and signal noise. Although all axes are comparable in terms of accuracy and signal noise, the y-axis has a low uncertainty and acceptable noise level. Future testing using this transducer should consider utilizing the y and z axes to measure lift and drag since these axes perform slightly better overall in terms of uncertainty and signal noise. However, with the current test setup, this transducer is suitable to measure forces in the mN range. Most importantly though, this transducer should be able to resolve the forces generated for the wings being tested.

### 4.2  Laser Vibrometer Testing Results

### 4.2.1  One-Layer Carbon Wing Results

The first type of wings tested using the laser vibrometer are one-layer unidirectional carbon fiber wings. The manufacturing process for this type of wing allows for greater inherent variability in simply placing the carbon components. Thus, it is expected that the natural frequency modes would vary some. This is what Figure 46 shows with each different shape and color representing a different wing design being tested. For better comparison of frequency, frequency is placed on the x-axis while the particular wing corresponds to the y-axis.
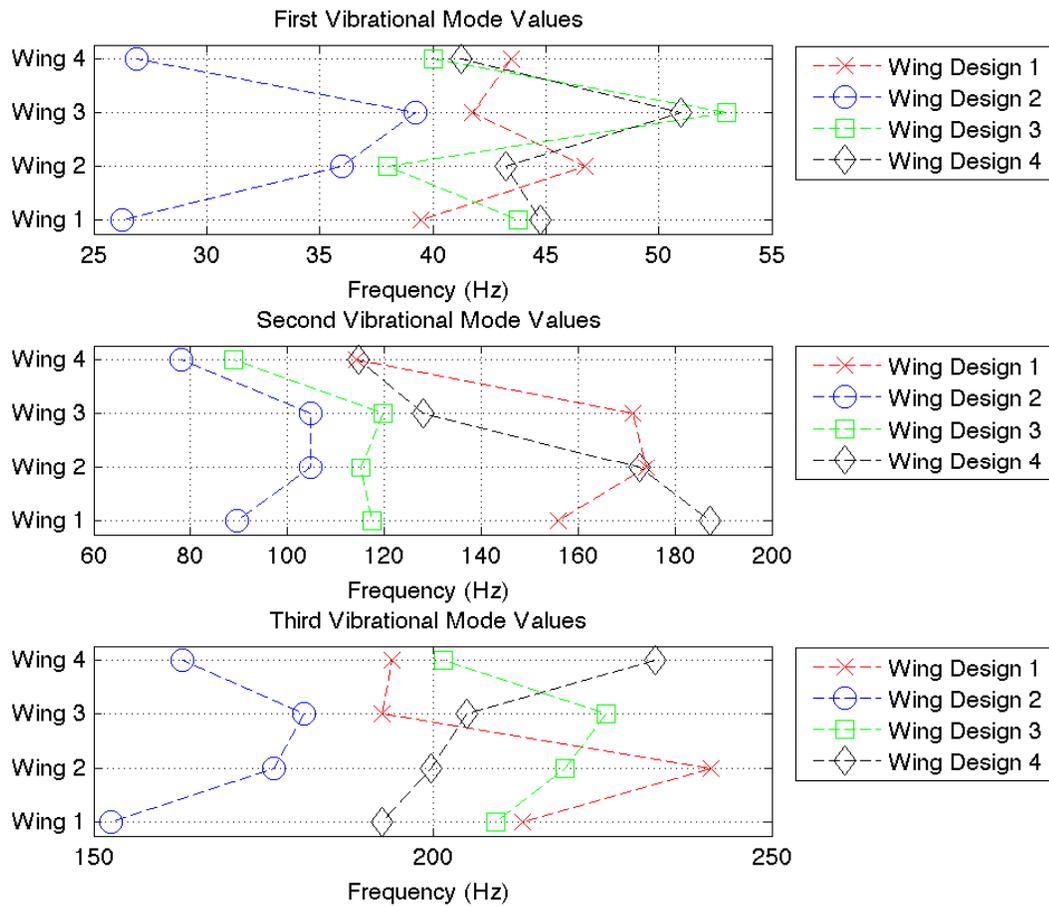
**Figure 46: Modes Comparison for One-Layer Unidirectional Carbon Wing Designs**

**1-4**

It is difficult to discern any noticeable trends from this data due to the large variation in data points.  It should be noted that all the values at a given mode fall within 1.5 standard deviations of the mean value at that mode. What is clear however is the significant spread in values for all wings at all natural frequencies citing poor structural dynamic repeatability in this particular manufacturing process.

Table 15 summarizes the statistical data from the laser vibrometer testing for the one-layer carbon wings. Looking at the normalized standard deviation, the variations in the different wings at the various modes quickly becomes apparent. From this table, it seems that no distinctive conclusions can be drawn about which wing is overall the most repeatable. Taking a mean of the normalized standard deviation though, Wing Design 3 has the overall lowest variations in mode frequency value with a mean value of 0.111. The only explanation for this result is random variability in manufacturing this particular type of wing. Since the individual carbon pieces, typically 4, are placed by hand into a mold, there is bound to be some large difference in the wing dynamics.

**Table 15: Summary of One-Layer Unidirectional Carbon Wing Designs 1-4**

**Statistics**

|  | Mode 1 | | | Mode 2 | | | Mode 3 | | |
|---|---|---|---|---|---|---|---|---|---|
|  | Mean | SDev | NSDev | Mean | SDev | NSDev | Mean | SDev | NSDev |
| Wing Design 1 | 42.87 | 3.06 | 0.071 | 153.87 | 27.58 | 0.179 | 210.18 | 22.61 | 0.108 |
| Wing Design 2 | 32.10 | 6.52 | 0.203 | 94.25 | 13.00 | 0.138 | 168.25 | 12.99 | 0.077 |
| Wing Design 3 | 43.68 | 6.65 | 0.152 | 110.37 | 14.67 | 0.13 | 213.94 | 10.67 | 0.050 |
| Wing Design 4 | 45.06 | 4.21 | 0.093 | 150.69 | 34.78 | 0.231 | 207.50 | 17.60 | 0.085 |

From this data, it is determined that the methods for manufacturing one-layer carbon wings could not produce a series of wings with essentially the same structural dynamic response.

Upon completion of the structural dynamic testing of all the one-layer carbon wings, one wing from each design is used to determine the mode shapes. Using the laser vibrometer as before, fifteen points are placed on the wing with the laser vibrometer scanning each point and then taking an average of five trials at each point. The average

FRF for each wing design for the one-layer carbon wings is shown in Figure 47. Based

upon the magnitude of the peaks of the average FRF, the contribution of each natural

frequency to the overall dynamic response of the wing can be found. Consistently among

all the wing designs, the $1^{st}$ mode has the highest peak, the $3^{rd}$ mode has the next highest,

and $2^{nd}$ mode has the lowest relative magnitude. This suggests that the $1^{st}$ and $3^{rd}$ mode

structural dynamics are dominating the vibrational response of each wing while the

effects of the $2^{nd}$ mode are being dampened by the other two modes.
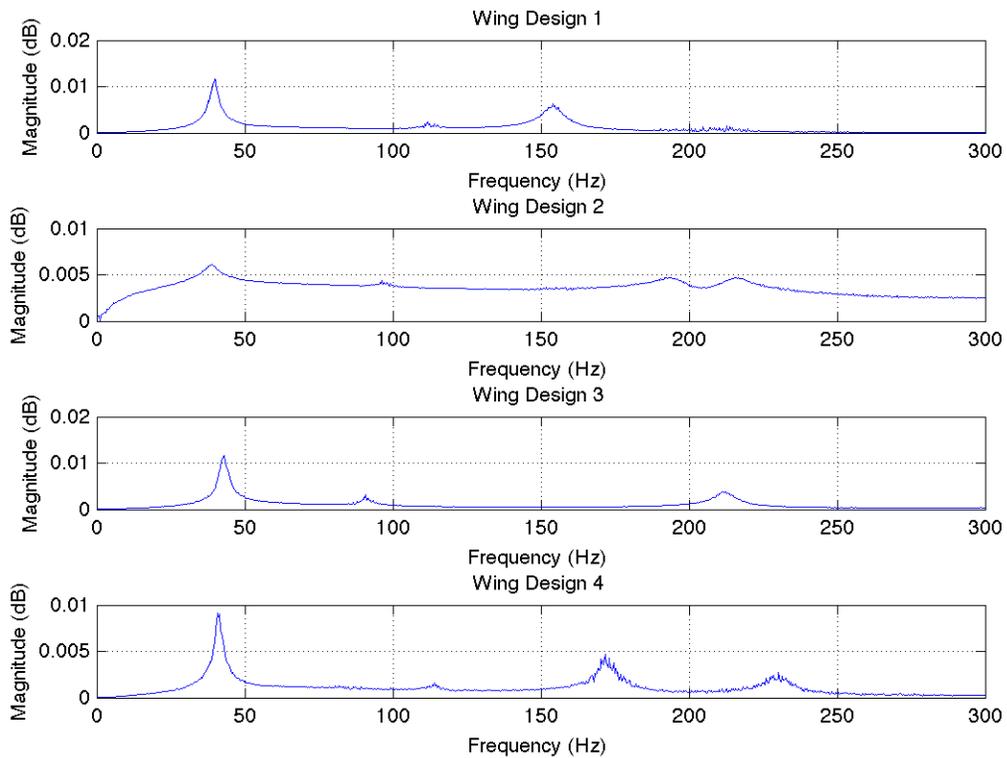


**Figure 47: FRF Average for One-Layer Carbon Wings**

From this data, the type of mode, torsion or bending, occurring at the first, second or third mode can be found using the Polytec animation software. This process is somewhat arbitrary as the particular mode type can be a combination of bending and torsion. The first mode of each wing was clearly bending. The ambiguity arose in determining the mode type of the second and third mode. A pictorial summary of the animation of the three primary modes for each wing design is shown in Figure 48.
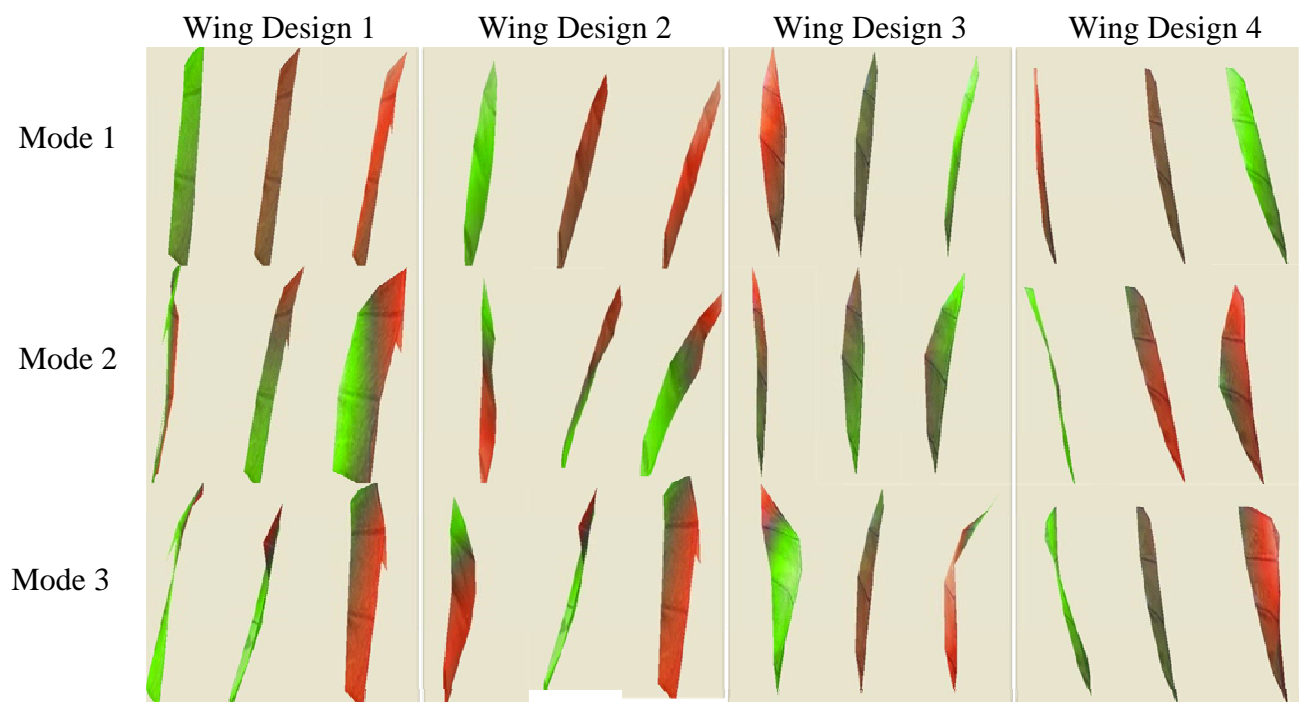


**Figure 48: Pictorial Summary of the Primary Wing Modes for the One-Layer Carbon Wings**

The results from analyzing the wing mode animations are shown in Table 16 with the mode types listed. Discussed in the

4.3 Wing Test Results section, Wing Design 3 and 4 have the greatest aerodynamic

efficiency while Wing Design 2 performed very poorly. Wing Designs 3 and 4 also have

the same 1$^{st}$ and 3$^{rd}$ modes, which as mentioned previously dominate the structural

dynamic response of the wing. It can then be speculated that a high magnitude torsional

3$^{rd}$ mode plays some role it achieving proper flapping rotation and thus better

aerodynamic characteristics.

**Table 16: Summary of Mode Types for One-Layer Carbon Wings**

|  | Mode Type 1 | Mode Type 2 | Mode Type 3 |
| --- | --- | --- | --- |
| Wing Design 1 | 1$^{st}$ Bending | 1$^{st}$ Torsion | 2$^{nd}$ Torsion |
| Wing Design 2 | 1$^{st}$ Bending | 2$^{nd}$ Bending | 3$^{rd}$ Bending |
| Wing Design 3 | 1$^{st}$ Bending | 2$^{nd}$ Bending | 1$^{st}$ Torsion |
| Wing Design 4 | 1$^{st}$ Bending | 1$^{st}$ Torsion | 2$^{nd}$ Torsion |

**4.2.2  Three-Layer Carbon Wing Results**

Looking at the laser vibrometer data from the three-layer cured carbon wings, the

results are significantly different than that of the one-layer wings. Figure 49 shows the

frequency and corresponding modes. The data points seem to be fairly well grouped

together with a much smaller spread in values. Furthermore, this is a consistent pattern

among all wings at all modes. From this data, it appears that this wing manufacturing

method produces more uniform results in terms of matching wing mode frequency

between wing sets. This conclusion can only be confirmed by looking at the statistical

data.
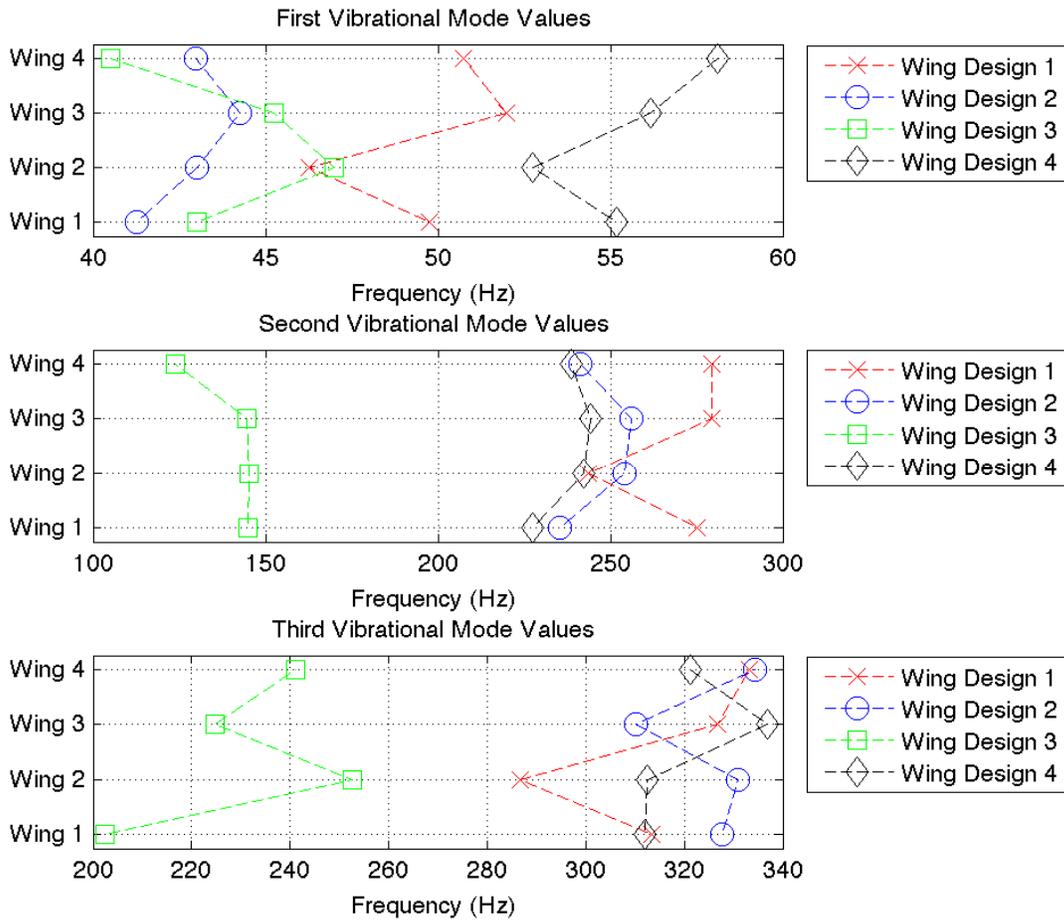
**Figure 49: Modes Comparison for Three-Layer Carbon Wing Designs 1-4**

The statistics of the three-layer cured carbon wings vibrometer data also cites to better repeatability in this manufacturing process. Looking at Table 17, the normalized standard deviations are about a factor of 3 less than those in Table 15. This is in part due to the larger mean values for the frequency modes themselves especially for the $2^{nd}$ and $3^{rd}$ modes, however, the normalized standard deviations is still small, implying reduced spread in the data values themselves.

**Table 17: Summary of Three-Layer Carbon Wing Designs 1-4 Statistics**

|  | Mode 1 | | | Mode 2 | | | Mode 3 | | |
|---|---|---|---|---|---|---|---|---|---|
|  | Mean | SDev | NSDev | Mean | SDev | NSDev | Mean | SDev | NSDev |
| Wing Design 1 | 49.68 | 2.47 | 0.049 | 269.43 | 17.40 | 0.065 | 315.06 | 20.59 | 0.065 |
| Wing Design 2 | 42.87 | 1.23 | 0.029 | 246.60 | 10.02 | 0.041 | 325.84 | 10.75 | 0.033 |
| Wing Design 3 | 43.94 | 2.82 | 0.064 | 139.62 | 10.42 | 0.075 | 230.19 | 21.69 | 0.094 |
| Wing Design 4 | 57.62 | 4.49 | 0.078 | 318.72 | 13.99 | 0.044 | 390.75 | 10.37 | 0.026 |

As with the one-layer carbon wings, an average FRF is obtained using the same process. Additionally, the $1^{st}$ and $3^{rd}$ mode natural frequencies of this wing type have significantly higher magnitudes than that of the $2^{nd}$ mode. Similar to the one-layer carbon wings, this again suggests the $1^{st}$ and $3^{rd}$ modes dominant the structural dynamics of the three-layer carbon wings.
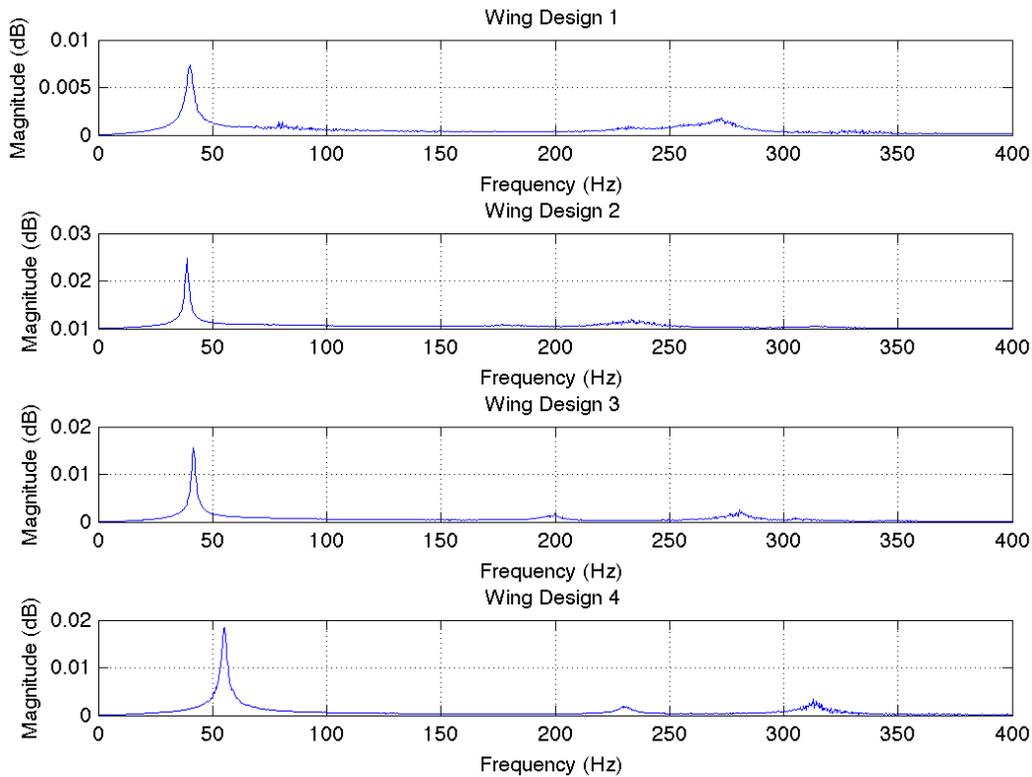


**Figure 50: FRF Average for Three-Layer Carbon Wings**

A pictorial representation of the animation generated from the average FRF is shown in
Figure 51. The results of the various animations are very similar to that of the one-layer
carbon wings and in fact almost identical.
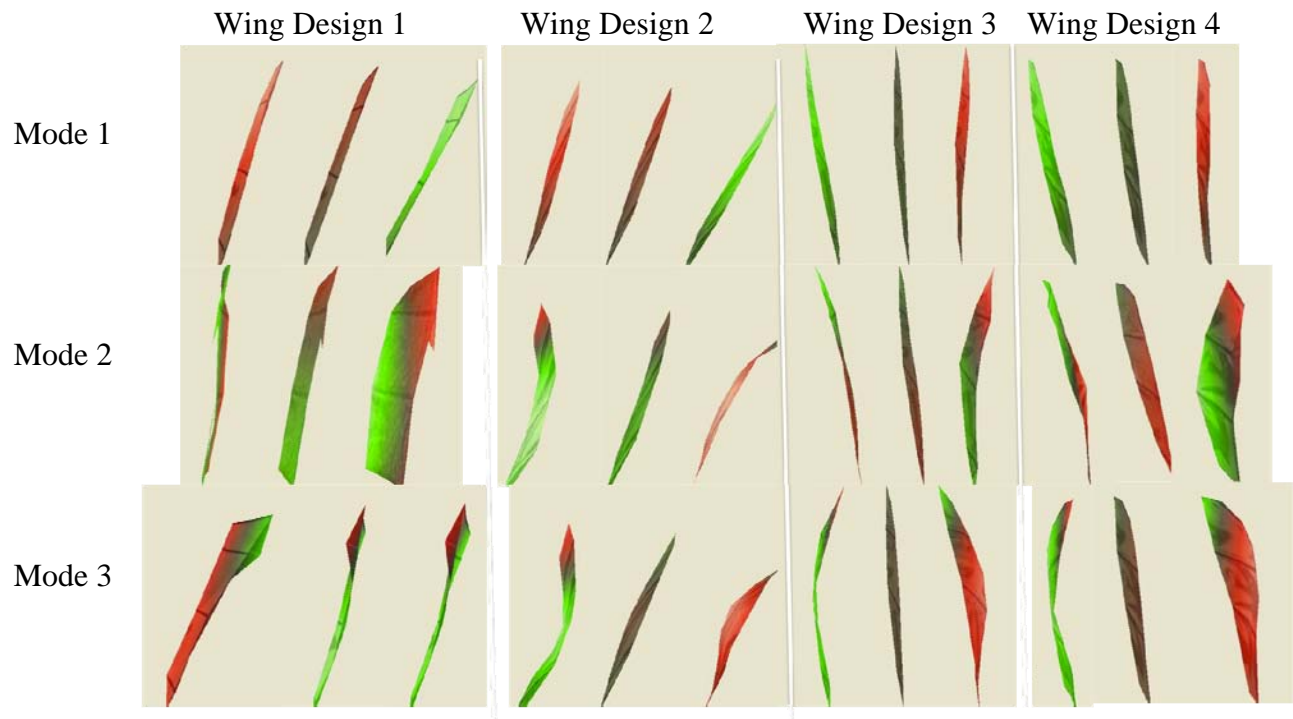


**Figure 51: Pictorial Summary of the Primary Wing Modes for the Three-Layer**

**Carbon Wings**

The results from analyzing the generated animations are shown in Table 18. Upon
determination of the specific wing mode type occurring at each natural frequency, the
only difference found from the results from the one-layer carbon wings is the 3$^{rd}$ mode
type for Wing Design 2 is 1$^{st}$ Torsion and oppose to 3$^{rd}$ Bending. This surprising result
could suggest that wing design is a significant contributor to the structural dynamic
response or that misinterpretation of the average FRF animations is very possible. Further
testing is required to drawn any further conclusions however.

**Table 18: Summary of Mode Type for Three-Layer Carbon Wings**

|  | Mode Type 1 | Mode Type 2 | Mode Type 3 |
|---|---|---|---|
| Wing Design 1 | $1^{st}$ Bending | $1^{st}$ Torsion | $2^{nd}$ Torsion |
| Wing Design 2 | $1^{st}$ Bending | $2^{nd}$ Bending | $1^{st}$ Torsion |
| Wing Design 3 | $1^{st}$ Bending | $2^{nd}$ Bending | $1^{st}$ Torsion |
| Wing Design 4 | $1^{st}$ Bending | $1^{st}$ Torsion | $2^{nd}$ Torsion |

### 4.2.3 Comparison of Laser Vibrometer Results

Using the normalized standard deviation in wing mode frequency to compare the manufacturing methods, the difference in repeatability readily become apparent as shown in Figure 52. The three-layer wing normalized standard deviation value is more consistent across the different modes. On average, the value for the normalized standard deviation is 56% less than the NSDev average for the one-layer wings. This suggests that the variability in the manufacturing of the three-layer carbon wings is less than that of the one-layer wings. The result is not necessarily surprising since the three-layer wings are essentially one piece of carbon, cut with a laser, and precisely placed over a piece of Kapton. This allows for less human variability in the process itself. The thee-layer wings, with its relatively small standard deviation becomes the superior manufacturing method from a repeatability in structural dynamic modes perspective.
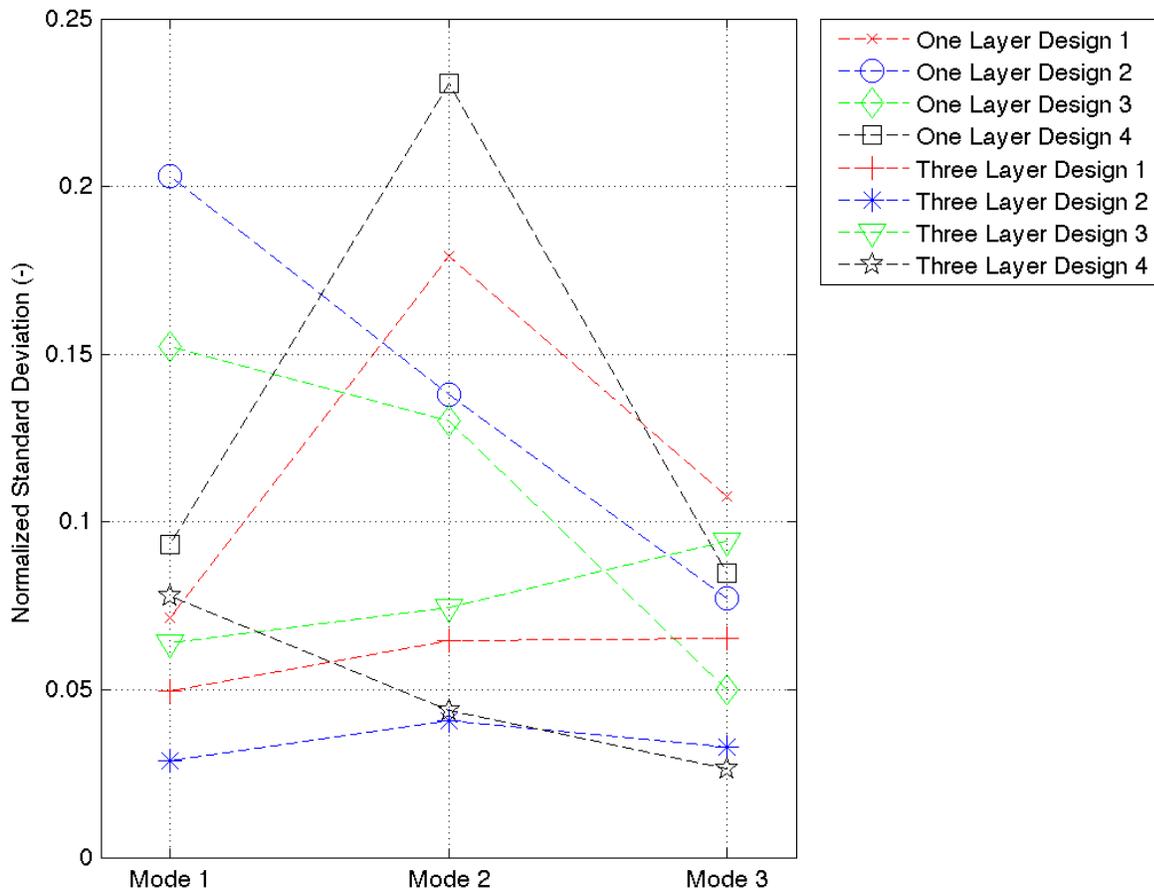
**Figure 52: Normalized Standard Deviation Comparison for Wing Modes**

Another important aspect of comparison is wing mass. The wings were weighed with the OHAUS Voyager Pro Model VP214CN scale, which is accurate to ±0.1 milligrams. The variation in mass should be very small since each wing design is made with the same materials in the same manner. The results from weighing four wings of each design of each type are summarized in Table 19. Note that the masses are in milligrams.

Looking first at the results from the one-layer carbon wings, there is noticeable variation in mass. The explanation can be found upon examination of the wings themselves. In the manufacturing process, mold release wax is placed in the joints of the

mold. The mold is buffed as much as possible, but buffing the joint grooves is problematic because the width is so small. This lack of buffing results in residual wax that then adheres to the Kapton during the curing cycle. Additionally, although every effort is made to not handle the wings with bare hands, fingerprints can be found on some of the wings. These two causes, because of the low weight of the wings, would affect the results in the fraction of milligram range as seen in the standard deviations listed in table. Overall though, the wing masses are similar with relatively small standard deviations.

**Table 19: Wing Mass Summary Comparison**

| | Wing 1 | Wing 2 | Wing 3 | Wing 4 | Mean | SDev | NSDev |
|---|---|---|---|---|---|---|---|
| One-Layer Wings | | | | | | | |
| Wing Design 1 (mg) | 11.3 | 11 | 10.7 | 10.5 | 10.87 | 0.350 | 0.0322 |
| Wing Design 2 (mg) | 10.4 | 10.5 | 10.5 | 11.3 | 10.67 | 0.419 | 0.039 |
| Wing Design 3 (mg) | 11.2 | 11.2 | 11.3 | 10.6 | 11.07 | 0.320 | 0.029 |
| Wing Design 4 (mg) | 10.1 | 10.2 | 10.3 | 10.1 | 10.17 | 0.096 | 0.009 |
| Three-Layer Wings | | | | | | | |
| Wing Design 1 (mg) | 20.3 | 20 | 19.5 | 19.5 | 19.82 | 0.395 | 0.020 |
| Wing Design 2 (mg) | 21.9 | 22.1 | 22 | 21.7 | 21.92 | 0.171 | 0.008 |
| Wing Design 3 (mg) | 21.4 | 21.2 | 21.2 | 20.9 | 21.17 | 0.206 | 0.010 |
| Wing Design 4 (mg) | 20.4 | 20.6 | 20.8 | 20.8 | 20.65 | 0.191 | 0.009 |

In contrast, the results of the three-layer carbon wings are more consistent and have a lower relative standard deviation. Upon inspection of these wings, there is no wax residue, but there is the occasional fingerprint which would affect the results. What is interesting though is that 3x the amount of carbon is being used as compared to the one-layer wings, yet the mass generally only increases by a factor of two. This speaks to the efficiency of the three-layer carbon layup and that enough pressure is being applied to

squeeze out excess resin. Additionally, from the one-layer carbon wings, the normalized standard deviation decreases by 57%.

From the results of the laser vibrometer and mass testing, it quickly becomes apparent that the three-layer wings produce greater consistency in both vibrational modes and mass. This type of manufacturing method would then allow a series of wings to be tested with approximately the same structural dynamic and mass characteristics.

## 4.3  Wing Test Results

Contrary to the expected force production of several mN, flapping wing testing resulted in forces in the 0.25-2.2mN range. From the transducer validation, this falls within its sensing range, but is greater than the noise threshold of the x-axis only by a factor of 3. Despite the mean force values at a minimum being approximately 3x greater than the x-axis noise values, Figure 53 shows the forces being produced are significantly greater than that. The different colored x's on the plot represents how the tare and force values are calculated. The first set of x's is the range over which the initial tare is taken. The second set is the range over which the first force value is calculated once the initial tare is subtracted. Each subsequent set represents a tare range and mean force range. Using these x's ensures that the tares and mean force calculations are occurring at the proper location within a given data set. Although this figure makes it appear that large instantaneous forces are being generated, the average value over each peak is representative of what is happening over the flapping stroke and is the data that will be presented.
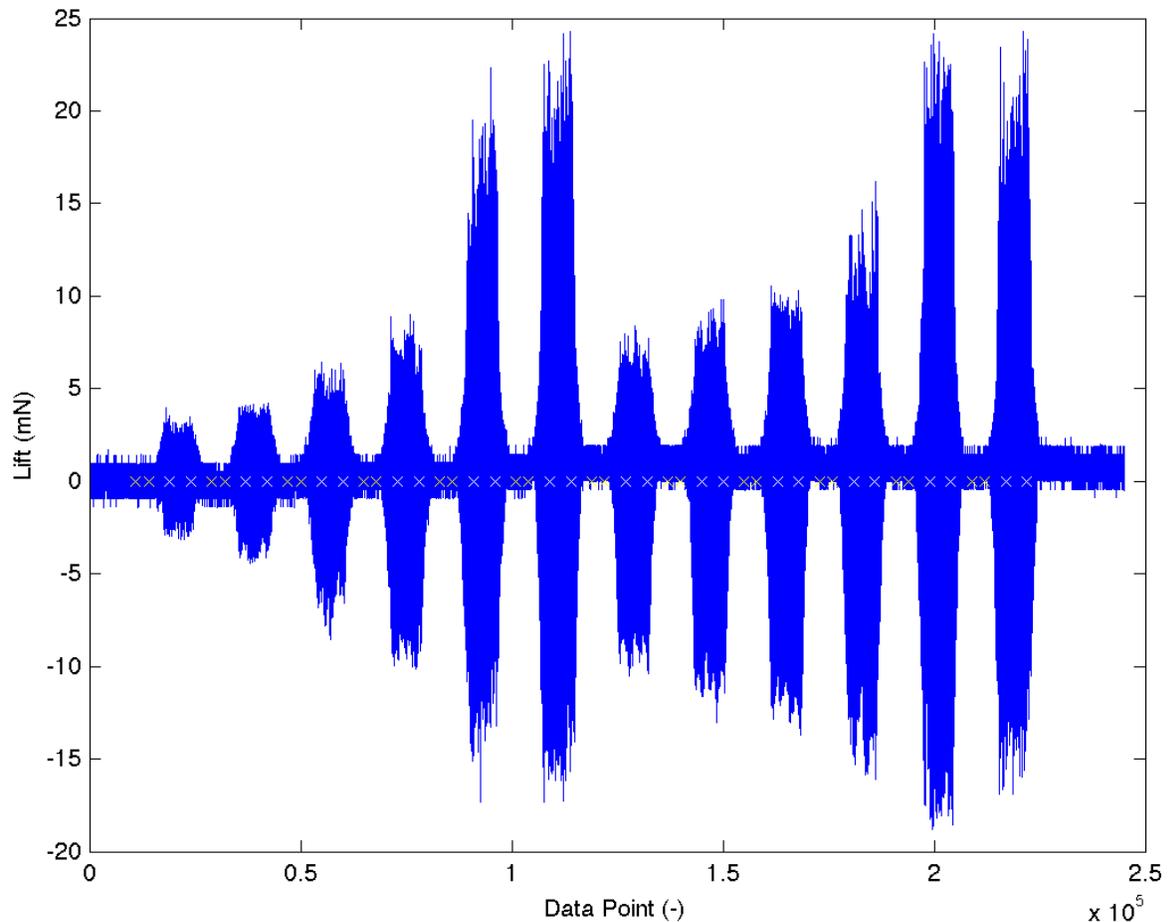
**Figure 53: Representative Fx Plot**

Another important consideration in flapping data is analysis of the stroke pattern to see whether the flapping upstroke and downstroke is mimicking that of nature or not. Taking the same data set presented in Figure 53 and using a 100 Hz lowpass software filter in Matlab, the following data results as shown in Figure 54. The flapping frequency for this portion of the data is 18 Hz. Since the x-values correspond to time, a flapping cycle should occur every 1/18 seconds or 0.0556 seconds. This trend is seen in the plot and correlated by the 18 Hz cosine wave. Since high speed video is not available to physically examine where within the flapping stroke the wing is at each data point, only

the overall shape of the flapping motion can be examined. With this in mind, as comparable to other research [25] the wing achieves some maximum lift (X=0 sec) during the upstroke prior to rotation where lift decreases dramatically (X=.01 sec). Lift then increases as the flapping velocity increase during the downstroke to reach some new maximum value prior to rotation (X=0.02s).
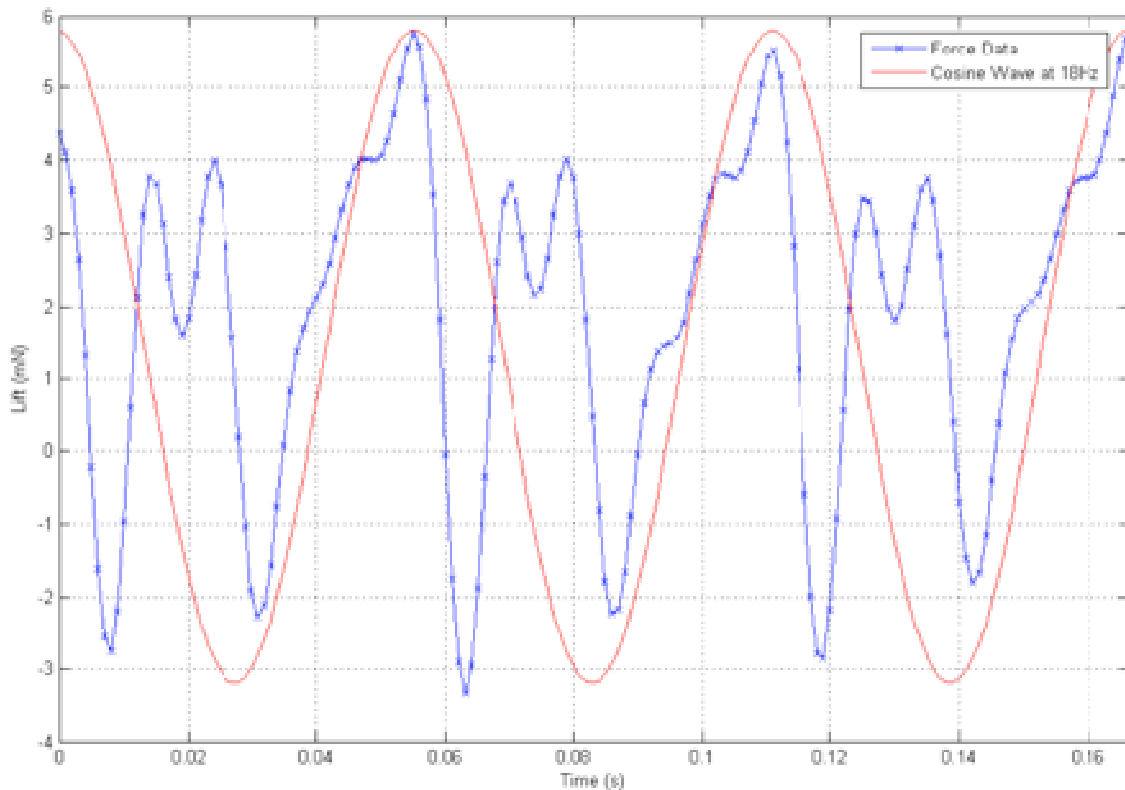


**Figure 54: Low Pass Filtered Data from Wing Design 4 Testing**

Finally, to analyze the frequency response of this data set, a Fast Fourier Transform is performed on the data shown in Figure 53. The first peak of the data should correspond to the previously mentioned flapping frequency of 21.6 Hz. As expected the first peak does corresponds to this value with subsequent peaks being periodic values of 21.6 Hz.
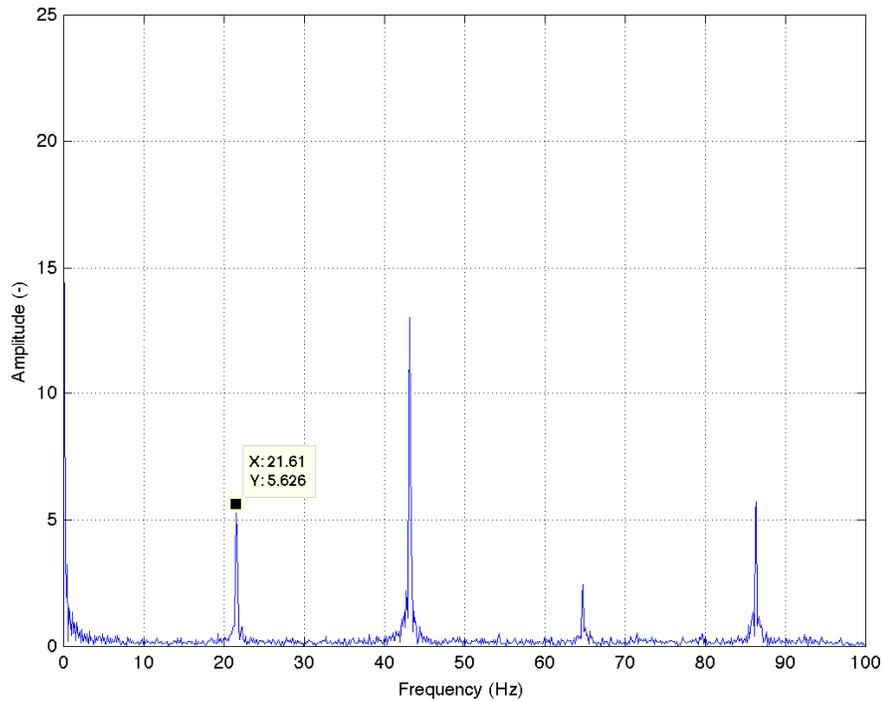
**Figure 55: Fast Fourier Transform of Wing Design 4**

To ensure continuity among flapping results, it was desired that only one double wing flapping actuator be utilized. Upon completion of testing the one-layer wings, the flapper was no longer functional. It was decided that a redesign was required to improve flapper robustness and ensure that the longevity of a flapper could be increased. Due to time constraints, data from the testing of the three-layer wings could not be included in the results presented here. However, three-layer flapping data can be found in a future paper by Sladek, Anderson, O'Hara, and Cobb.

Additionally, during testing of Wing Design 2, it quickly became apparent that the curvature of the wings was not sufficiently strong enough to endure the strain of flapping and thus very poor data was collected with no clear indication of first mode resonance.

Although reasonable force values were obtained, the flapping motion itself was erratic

and not conducive for further flapping out of concern for the flapping mechanism. Thus,

data for Wing Design 2 will also be omitted. This design is viable, just not for one-layer

carbon.

Finally, using the procedures described in 3.4.2 Wing Testing to find the first

mode resonant frequency, Table 20 shows the flapping frequencies used for testing of

each wing design.

**Table 20: Wing Flapping Frequencies Used for Testing**

| | Flapping Frequency (Hz) |
|---|---|
| Wing Design 1 | 19 |
| Wing Design 3 | 18 |
| Wing Design 4 | 18 |

Since this particular type of FWMAV testing is attempting to emulate a hovering

insect, an explanation of what the measured forces actually correlate to is required. Lift

values are the forces measured in the positive x-direction of the transducer. These values

do in fact correspond to the classical definition of lift and ultimately is what would allow

a FWMAV to hover. The force measured perpendicular to lift is typically drag, which

corresponds to the positive z-direction and would in fact be drag if hovering was not

being replicated. However, for this research an average drag value is simply a measure of

the asymmetry of the flapping stroke. Ideally, these values would be zero but as the

results will show, are small, but not zero. This could be a result of wing or flapping

mechanism kinematics. The wing that flaps most symmetrically though is better suited

for future testing and thus drag will still be used as a measure of performance.

### 4.3.1  Flapping Results from Wing Design 1

As shown in Table 20, testing for Wing Design 1 used a first mode natural frequency of 19Hz. During testing it was visually noted that this design experienced minimal rotation through the flapping stroke. As noted by previous research (see 2.1 Aerodynamics and Kinematics of Nature's Micro Air Vehicles section), proper rotation at key times during the stroke is key to maximizing lift. As such, the lift generation produced by this wing is marginal as compared to the other designs with drag also being quite high.

The result of Wing Design 1 testing is shown in Figure 56. This particular figure shows both the lift and drag values at a particular test point. The upper portion of the plot shows the frequency sweep where amplitude is held constant while the lower portion is the amplitude sweep where the frequency is held constant. The x's on the plot are lift values where average lift is represented by squares. The o's are the drag values with the diamonds showing the average value.
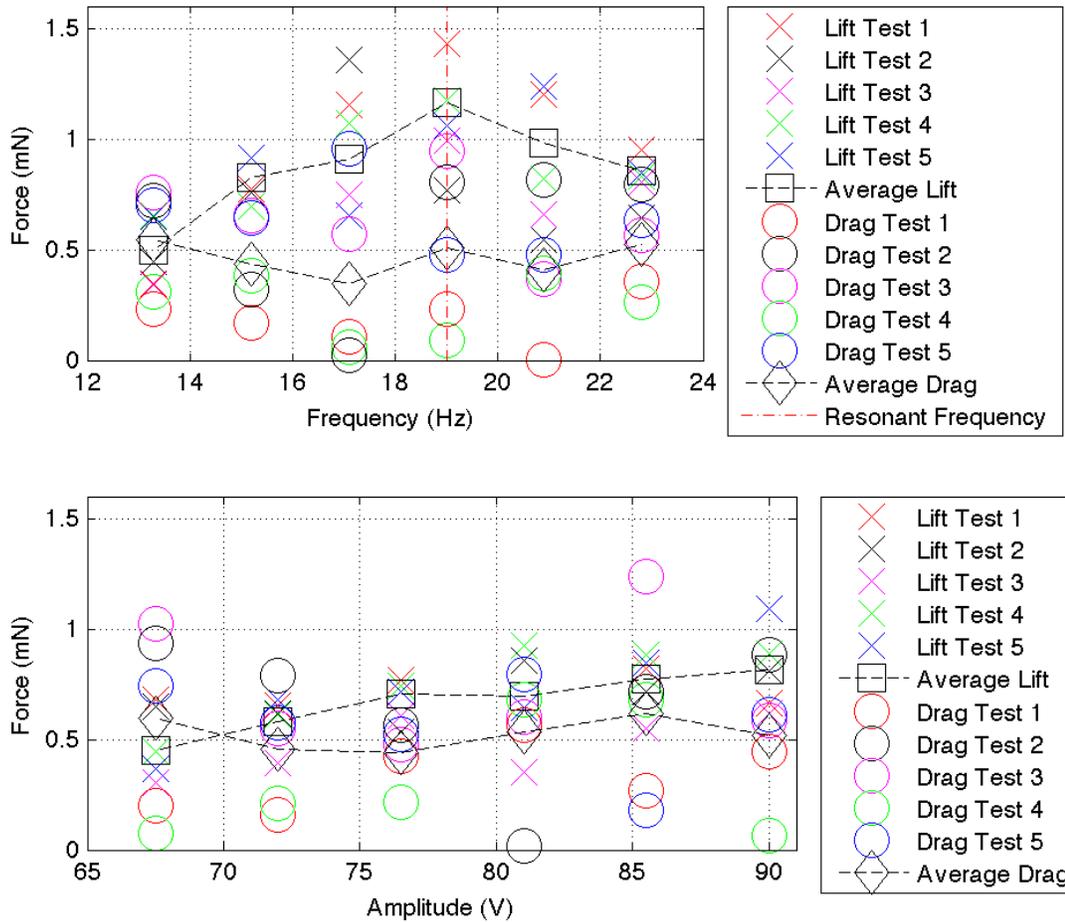
**Figure 56: Wing Design 1 Aerodynamic Results**

Despite minimal lift production, Wing Design 1 was not meant to demonstrate efficient aerodynamics therefore these results are to be expected. What can be analyzed however are the trends in the forces being produced. As the flapping frequency approaches the first mode, the aerodynamic efficiency of the wing should increase, reach the first mode flapping frequency, and then consequently decreases. This trend is apparent in the upper portion of Figure 56 where at the approximated first mode natural frequency of 19 Hz, the lift production is maximized.

At this value also, the difference between the average lift and average drag value should be maximized; that is when flapping at the first resonant frequency, L/D should be maximized. While lift is maximized at this point as expected, greater flapping asymmetry is occurring resulting in a higher drag value reducing the overall L/D. This is in part due to the Test 2 outlier value at this frequency but also cites to possible variation in measuring the force values.

Referring now to the amplitude sweep, it would be expected that as amplitude increases lift would increase as well. Since the flapping frequency is held constant at 1.2 times that of first mode resonance, as flapping amplitude increase the wing pushes on more air with a higher velocity. Looking at $\vec{V}_{\text{tip}}$ as defined in Equation 1 and using the standard definition of lift equal to $L = 0.5\rho\vec{V}_{tip}^{2}C_{L}S$ as the peak-to-peak amplitude increases, so will lift assuming a constant lift coefficient. This same principle cannot be applied to drag production since the drag values should ideally average to zero implying no flapping asymmetry or at least be constant. As amplitude increases, drag does appear to be fairly constant around 0.5 mN while lift linearly increases.

The final conclusion that can be drawn from this figure is repeatability in measured force values. The forces being produced at the last value of the frequency sweep should correspond to the last value of the amplitude sweep since at this point the flapping conditions are the same. Using the ratio of lift to drag, the percent difference between the two points is 13.7%. Since the forces being produced at the respective points are fairly small and approaching the minimum resolution of the transducer, this percent difference seems very reasonable and cites to repeatability in the measured values.

### 4.3.2  Flapping Results from Wing Design 3

Many of the trends found in the results of Wing Design 1, are also apparent in Wing Design 3 with the results shown in Figure 57. Testing for this wing design used a first mode resonance of 18 Hz. Examining the frequency sweep first, maximum lift production does not occur at resonance but rather at 16.2 Hz or 90% of resonance. There are two possible explanations for this. First, when estimating first mode resonance, there is some variability in the values due to the fineness of the sweep of input frequencies in which first mode resonance is determined from. In determining this value, an accurate value was found and assumed to be sufficient. Since for this particular plot, the force value at 16.2 Hz is very close to that of 18 Hz, it is possible that first mode resonance occurred at 16.2 Hz. As part of this explanation, accuracy of the balance is also a factor. Since the two force values at 18 and 16.2 Hz respectively are very close, it is possible that more lift was produced at 16.2 Hz but more tests would be required to determine that trend. One critical conclusion that can be gleaned from this testing is that numerous tests are required to accurately represent the forces being measured.

During testing it was also noted that the rotation of the Wing Design 3 was greater than that of Wing Design 1 with an approximated rotation angle of 45° during the upstroke and downstroke. As mentioned previously, wing rotation is critical to lift production and with this greater rotation it is not surprising then that Wing Design 3 produces greater lift than Wing Design 1.
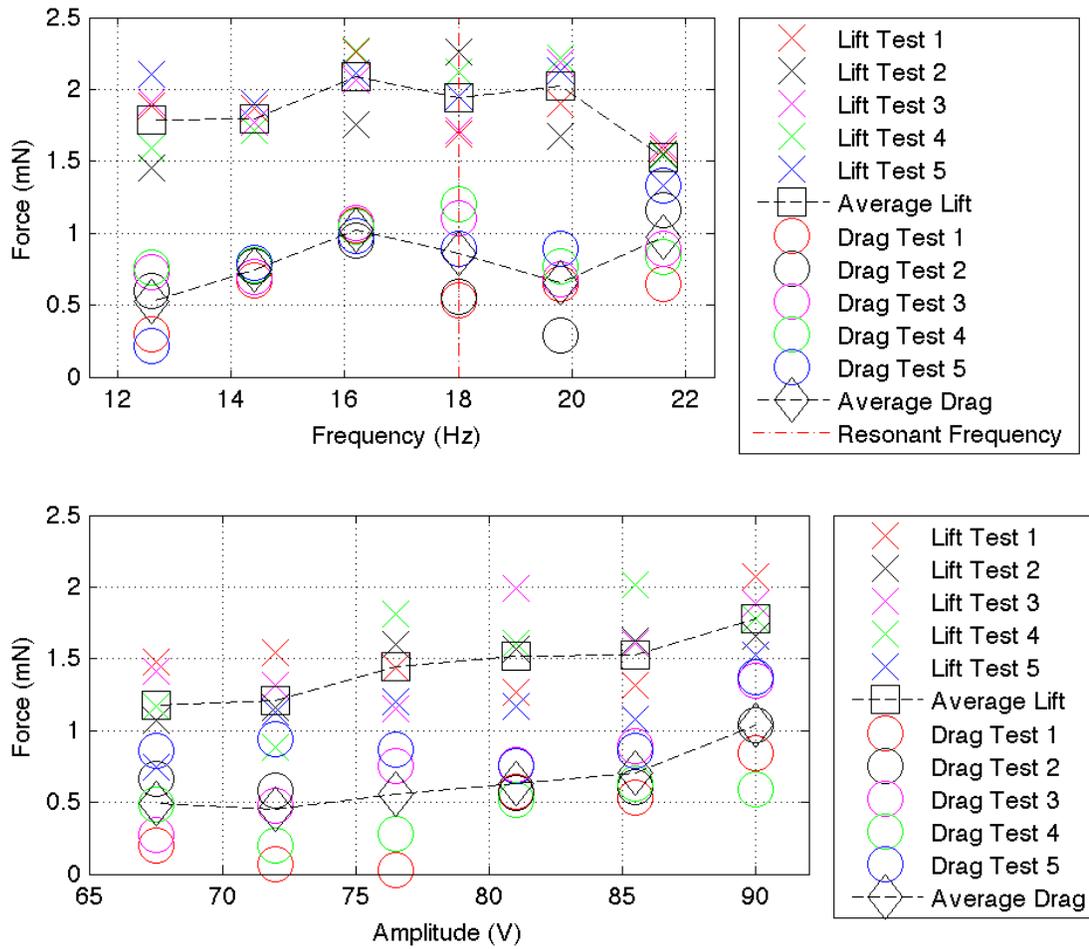
**Figure 57: Wing Design 3 Aerodynamic Results**

Looking at drag from the frequency sweep, the values increase until first mode

resonance is approached around 16.2-18 Hz in which drag decreases. This indicates a

greater flapping unevenness as resonance is approached and an overall high variability in

flapping amplitude during the upstroke as compared to the downstroke.  Additionally, in

Wing Design 1, the ratio of the smallest lift value to largest was approximately 2x

whereas for Wing Design 3 there is a minimal increase in lift over the frequency sweep.

This plateau of lift values suggests a possible insufficient bandwidth of the flapping

actuator or that the actuator itself is adversely dampening the structural dynamic modes of this wing. This could possibly explain the high variability in the drag values as well.

From the amplitude sweep data, the trend follows what would be expected. As with Wing Design 1, as amplitude increases so does lift with little variability in the lift to drag ratio. Since this particular wing design is producing greater lift values as compared to Wing Design 1, improved resolution and consequent force value repeatability would be expected. This is the case with the percent difference between the final frequency sweep and amplitude sweep values being 9.15%.

### 4.3.3  Flapping Results from Wing Design 4

Wing Design 4 testing utilized a measured first mode resonant frequency of 18 Hz with results presented in Figure 58. Similarly to Wing Design 3, the performance of the wing was not maximized at the first mode resonant frequency citing the need to more accurately measure the first mode using a finer input frequency range. It appears that resonance for this wing occurred at approximately 20 Hz with the lift value reaching a maximum at this point. Comparable to Wing Design 1, there is a large rise in lift production at the resonant frequency from the previous frequency. The overall trend of the lift curve for Wing Design 4 is favorable despite maximum lift not occurring at the expected value.

Although this wing does not produce as much lift as Wing Design 3, its lift to drag ratio is significantly higher which corresponds to high lift production and minimal flapping asymmetry. Examining the drag values, all values are less than 0.5 mN whereas for Wing Design 1 and 2, the drag values are between 0.5 mN to 1.0 mN. Since this

particular wing placed more surface area at the tip than the other designs, greater wing rotation did occur with an approximated value of ±60°. This greater rotation suggests better overall aerodynamic efficiency as seen by the large L/D ratio of 6 occurring at 20 Hz.
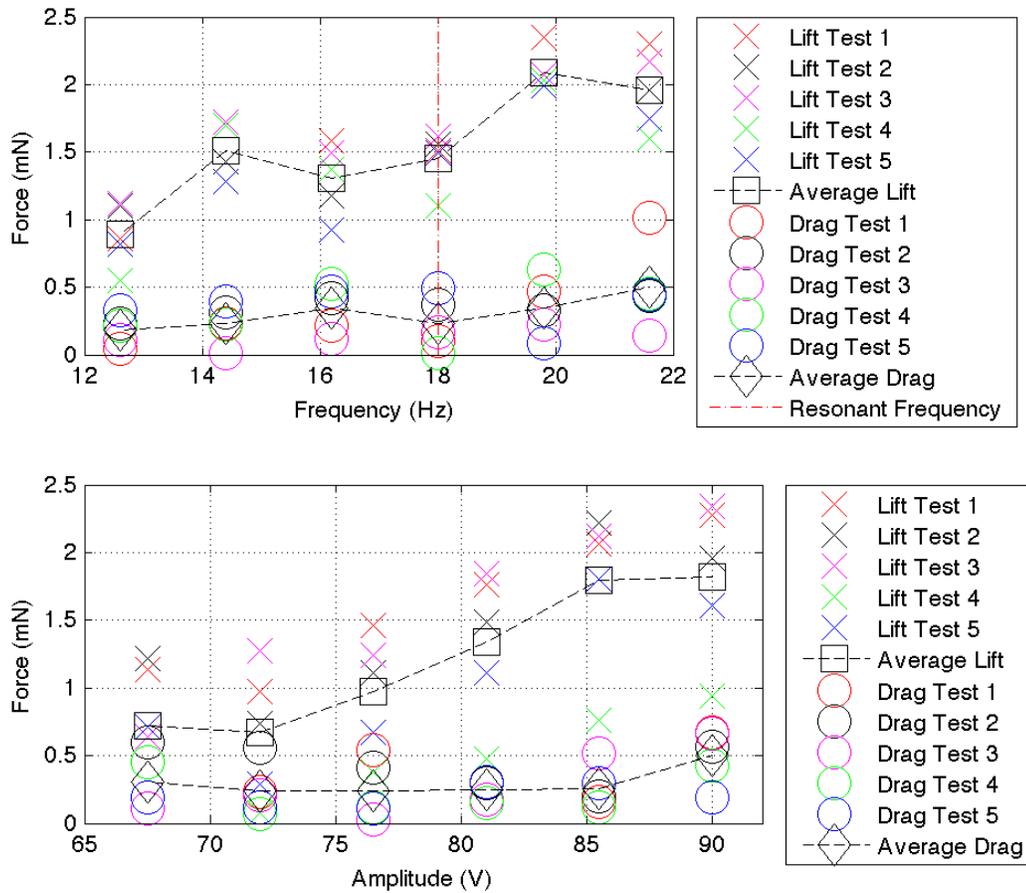


**Figure 58: Wing Design 4 Aerodynamic Results**

From the amplitude sweep data, a favorable upward trend of lift values does occur. One noticeable difference in this data as compared to the other figures is the spread in values especially in reference to Test 4, which seems to be mostly comprised of

107

outliers as compared to the other data points. Despite this greater variance, the percent difference between the final test point of both sweeps is 8.06% which is consistent with the previous designs.

### 4.3.4  Comparison of Testing Results

Although, the best measure of a FWMAVs efficiency is lift to power consumption, measuring power consumed is not an easy task and was not recorded for this research. However, a useful measure of performance is the ratio of lift to flapping asymmetry or drag.

This ratio for each wing at each data point is shown in Figure 59. The main reason for Wing Design 4's high L/D is the consistent low drag values. It did produce comparable lift to the other designs, but its drag values were typically much lower. This figure definitely shows that Wing Design 4 is most aerodynamically efficient design with an average L/D of 4.7 with Wing Design 1 and 2 having averages of 1.5 and 2.4 respectively.
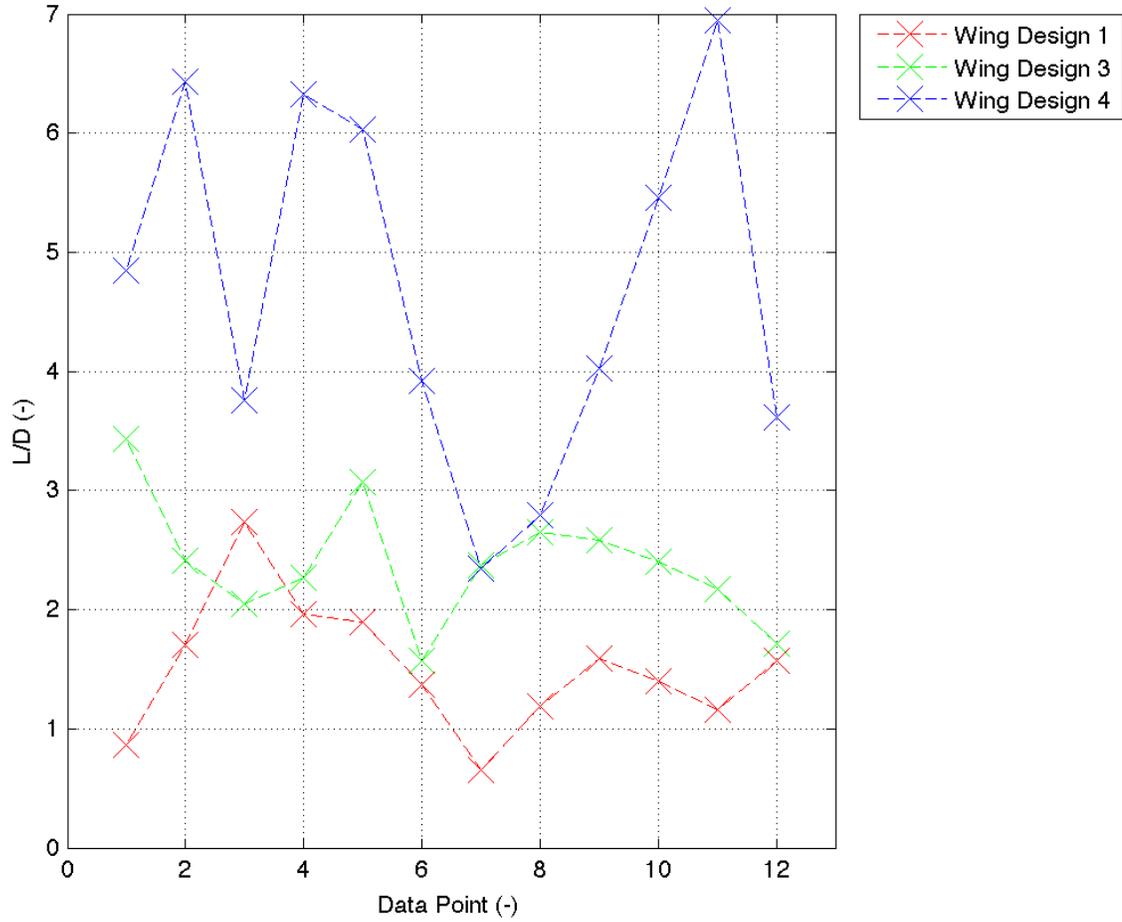
**Figure 59: Lift to Drag Comparison**

With measured force values, known wing beat frequency, surface area, while

assuming a constant tip-to-tip amplitude of 35mm for all wings, mean lift and drag

coefficients can be calculated with $C_L = \frac{L}{0.5\rho \vec{V}_{tip}^2 S}$ and $C_D = \frac{D}{0.5\rho \vec{V}_{tip}^2 S}$ using the definition

of $\vec{V}_{tip}$ defined in Equation 1. These values along with other important characteristics of

each wing design are shown in Table 21.

**Table 21: Summary of Aerodynamic Parameters of Each Wing Design**

| | Mean $C_L$ | Mean $C_D$ | Mean Lift (mN) | Mean Drag (mN) | Mean L/D | Mean SDev Lift | Mean SDev Drag |
|---|---|---|---|---|---|---|---|
| Wing Design1 | 0.87 | 0.60 | 0.71 | 0.49 | 1.51 | 0.17 | 0.29 |
| Wing Design 3 | 1.04 | 0.45 | 1.65 | 0.72 | 2.39 | 0.23 | 0.23 |
| Wing Design 4 | 1.30 | 0.28 | 1.38 | 0.30 | 4.71 | 0.37 | 0.184 |

From this table, it becomes apparent that Wing Design 4 is significantly more aerodynamically efficient than the other two designs. Despite not having the maximum lift generation, it does produce a much larger lift coefficient as compared to the other wings. The lift values for this design do have the greatest spread. This stems mostly from the fact that the measured force values for Test 4 are considerably lower than the other values. If this particular test is excluded from the standard deviation calculation, the variation reduces to 0.25, which is comparable to the other values.

Since the measured force values are much lower than the expected 10 mN, the uncertainty analysis performed becomes inapplicable. However, since the forces for the same test conditions were measured at two points during testing, the difference between those two values can be used to compute uncertainty. Thus, referring to the results from each wing, the uncertainty associated with Wing Design 1 is 13.7%, Wing Design 3 is 9.15% and Wing Design 4 had an uncertainty of 8.06%. These values are all very satisfactory and lead to confidence in the measured values.

## 4.4  Summary

This results section covers a wide range of topics with two main purposes: best wing manufacturing process and best wing design. In terms of structural dynamic

repeatability, wing manufacture 3.1.5  Wing Manufacture Method Four is superior in terms of primary mode matching and mass consistency. The downside of this method is it takes significantly longer to have the components to manufacture an individual wing. The three-layer carbon must be laid up, cured, and then cut with cutting time taking considerably longer than with the one-layer carbon. However, this method is much more suited for mass production and allows for significantly less variability in manufacturing. Using this manufacture process, an optimal wing design could be found since manufacture inconsistency is minimized.

Additionally, it was determined that the force/torque transducer is suitable to measure the forces being generated by micro air vehicle wings in this size range. As shown by the data, this transducer has enough resolution to measure the aerodynamic differences between three unique wing designs. This furthers the goal of finding an optimal wing design. Additionally, from this data it was found that Wing Design 4 significantly aerodynamically outperformed the other wing designs. This conclusion seems very reasonable, as this design is very similar to that of a hawkmoth wing. From this research, repeatable manufacturing techniques will enable optimal wing design, the transducer utilized will accurately allow for measuring of the forces produced by these wings, and optimal design should start with Wing Design 4.

# 5. Conclusions and Recommendations

Four FMWAV wing designs are selected to test manufacture repeatability and aerodynamic efficiency. Wings are manufactured using carbon fiber for the vein structure and Kapton for the wing membrane. From this research, two distinct manufacturing techniques emerged with one utilizing one-layer uncured prepreg carbon while the other uses three-layer cured carbon. For the one-layer carbon wings, an optimal manufacturing process is obtained by utilizing a carbon/Pyralux membrane with the wing structure components cut with a laser, then placed in wing molds and overlaid with Kapton, and finally placed in an autoclave to cure. The three-layer carbon method uses a cured carbon/Pyralux membrane cut with a laser. This method does not require molds due to how the membrane and carbon structure align. Manufacture repeatability of both methods is evaluated through simply weighing the wings and through the use of a laser vibrometer to determine the structural dynamic response of each wing. From this, it was found that the three-layer carbon wings are significantly more repeatable in terms of matching the first three natural frequencies for each respective wing as compared to the one-layer wing results. Additionally, there was less variation in mass for the three-layer wings. From this data, the three-layer carbon wings were found to produce higher repeatability in structural dynamics as well as mass as compared to the one-layer carbon wings. This repeatability proves that makings structural-dynamically repeatable wings is possible and with further refinement, producing wings with almost exactly the same dynamic flapping characteristics is feasible. This manufacturing process with cited repeatability was not found in review of the literature.

Aerodynamic testing comprised of testing only the one-layer carbon wings. Dual piezoelectric actuators were utilized to generate the flapping motion for two wings. Each wing was tested a six flapping frequencies and six amplitudes. Forces were measured using an ATI Industrial Automation Nano-17R force/torque transducer. Due to the small loads being generated from the flapping motion, validation of the transducer occurred to determine axis interactions, quantify signal noise and determine measurement uncertainty. From this testing, it was found that Wing Design 4, which is similar to that of a hawkmoth, proved most aerodynamically efficient based upon average lift and flapping asymmetry with an average lift to drag ratio of 4.71. Additionally, the force/torque transducer used for this testing is suitable to measure the flapping forces generated by a FWMAV and can be utilized for future testing.

Future testing should consist of flapping three-layer carbon wings using the methods described in this thesis. Additionally, a more robust flapping actuator should be developed with a larger bandwidth capable of flapping at much higher frequencies. Techniques need to also be developed to repeatedly attach the wings to the flapping actuator. Finally, future work should consider building an in-house force transducer with resolution in the μN range.

# Appendix

## Matlab Code to Generate Testing Array

```matlab
%Author: Nathanael Sladek
%Year: 2010
%This code creates the testing array used to test each wing

function [freq_res amp amps freqs tare d prep paws s]=Wing_inputs_wing

clear all
close all
clc

d = 7; % dwell time for each measurement point
tare = 5;
prep = 10; % wait time before starting run
s=3;
paws_Freq = [s d s tare s d s tare s d s tare s d s tare s d s tare s d];
paws_Amp = [s tare s d s tare s d s tare s d s tare s d s tare s d s tare s d s d d];
paws = [prep paws_Freq paws_Amp];

amp=3;
freq_res=19*2*pi;

k = length(paws);
times(1)=0;
for i = 1:k;
 times(i+1) = sum(paws(1:i));
end

%%

amps=[0.75*amp 0.8*amp 0.85*amp 0.9*amp 0.95*amp amp];
freqs=[0.7*freq_res 0.8*freq_res 0.9*freq_res freq_res 1.1*freq_res 1.2*freq_res];

inputs=zeros(3,length(times));
inputs(1,:)=times;

inputs(2,2:5)=freqs(1);
inputs(2,6:9)=freqs(2);
inputs(2,10:13)=freqs(3);
inputs(2,14:17)=freqs(4);
inputs(2,18:21)=freqs(5);
inputs(2,22:length(times)-2)=freqs(6);
inputs(3,3:4)=amps(6);
inputs(3,7:8)=amps(6);
inputs(3,11:12)=amps(6);
inputs(3,15:16)=amps(6);
inputs(3,19:20)=amps(6);
inputs(3,23:24)=amps(6);

inputs(3,27:28)=amps(1);
inputs(3,31:32)=amps(2);
inputs(3,35:36)=amps(3);
inputs(3,39:40)=amps(4);
inputs(3,43:44)=amps(5);
inputs(3,47:48)=amps(6);
```

```matlab
subplot(2,1,1);plot(inputs(1,:),inputs(3,:))
xlabel('Time (s)');ylabel('Amplitude (V)')
grid on
subplot(2,1,2);plot(inputs(1,:),inputs(2,:))
xlabel('Time (s)');ylabel('Frequency (Hz)')
grid on

save Wing_Testing_Inputs_wing.mat inputs

Ts=0.001;

end
```

## Matlab Code to Read in Aerodynamic Test Data

```matlab
%Author: Nathanael Sladek
%Year: 2010
%This code reads in a .csv file and converts forces and torques in terms of
%counts into actual force values. It also reads in a input file to properly
%tare to find the average force at specific flapping conditions

clc
clear all
close all
Test='test14 18hz 3a';

fid=fopen( Test);

for i=1:7

A{i}=fgets(fid);

end

Sample_Rate=A{1,2};
CUF=A{1,4};
CUT=A{1,6};

[str_Sample_Rate]=sscanf(Sample_Rate,'%s%s%s%f');
Sample_Rate=str_Sample_Rate(length(str_Sample_Rate));
[str_CUF]=sscanf(CUF,'%s%s%s%s%f64');
CUF=str_CUF(length(str_CUF));
[str_CUT]=sscanf(CUT,'%s%s%s%s%f');
CUT=str_CUT(length(str_CUT));

C=textscan(fid,'%s %f %f %f %f %f %f %f %f %s', 'delimiter', ',');
fclose(fid);

Data_Pt=C{1,2}(:);
FT_Seq=C{1,3}(:);
Fx=C{1,4}(:)/CUF;
Fy=C{1,5}(:)/CUF;
Fz=C{1,6}(:)/CUF;
Tx=C{1,7}(:)/CUT;
Ty=C{1,8}(:)/CUT;
Tz=C{1,9}(:)/CUT;

%%
[freq_res amp amps freqs tare d prep paws s]=Wing_inputs_wing;
Inputs=open('Wing_Testing_Inputs_wing.mat');
close all

freqs=Inputs.inputs(2,:);
amps=Inputs.inputs(3,:);
```

115

```matlab
test_length=sum(paws(1:length(paws)-1));
end_time=224;
offset=test_length-end_time+2;

j=1;
start_cell=3;

for i=start_cell:length(paws)

    if paws(i)==d

        start_time(j)=Inputs.inputs(1,i);
        tares(j)=Inputs.inputs(1,i);

        j=j+1;

    end

end

start_time_offset=start_time+offset;
tares_offset=tares+offset-8;

j=0;
for i=1:length(start_time_offset)-1

    stb(i+j)=start_time_offset(i)*1000;
    tb(i+j)=tares_offset(i)*1000;
    j=j+1;
end

for i=2:2:length(stb)-1

    stb(i)=stb(i-1)+5000;
    tb(i)=tb(i-1)+3000;

end

stb=stb(1:length(stb)-1);
tb=tb(1:length(tb)-1);

%%
j=1;

for i=1:2:length(stb)-1

    Fx_tare(j)=mean(Fx(tb(i):tb(i+1)));
    Fy_tare(j)=mean(Fy(tb(i):tb(i+1)));
    Fz_tare(j)=mean(Fz(tb(i):tb(i+1)));
    Tx_tare(j)=mean(Tx(tb(i):tb(i+1)));
    Ty_tare(j)=mean(Ty(tb(i):tb(i+1)));
    Tz_tare(j)=mean(Tz(tb(i):tb(i+1)));

    Fx_n(j)=mean(Fx(stb(i):stb(i+1)))-Fx_tare(j);
    Fy_n(j)=mean(Fy(stb(i):stb(i+1)))-Fy_tare(j);
    Fz_n(j)=mean(Fz(stb(i):stb(i+1)))-Fz_tare(j);
    Tx_n(j)=mean(Tx(stb(i):stb(i+1)))-Tx_tare(j);
    Ty_n(j)=mean(Ty(stb(i):stb(i+1)))-Ty_tare(j);
    Tz_n(j)=mean(Tz(stb(i):stb(i+1)))-Tz_tare(j);

    j=j+1;

end

Array=[Fx_n*1.2;Fy_n;Fz_n;Tx_n;Ty_n;Tz_n];
```

## Matlab Code to Read in Laser Vibrometer Data

```matlab
%Author: Nathanael Sladek
%Year: 2010
%This code reads in data generated by a Polytec 3D laser vibrometer to
%create FRF plots. The bounds of each peak must be manually inputted as the
%LP variable

clear all
close all
clc

%files=['rec1.txt';'rec3.txt';'rec4.txt';'rec6.txt'];
%files=['eli1.txt';'eli3.txt';'eli4.txt';'eli5.txt'];
files=['pep2.txt';'pep3.txt';'pep1.txt';'pep6.txt'];
%files=['wing1.txt';'wing2.txt';'wing3.txt';'wing5.txt'];


for n=1:length(files(:,1))

fid=fopen(files(n,:));

for i=1:5

A{i}=fgets(fid);

end

C=textscan(fid,'%f %f');
fclose(fid);

subplot(6,1,n);plot(C{1,1},C{1,2})

freq(:,n)=C{1,1};
mag(:,n)=C{1,2};

freq_n(:,n)=freq(20:length(freq(:,n)),n);
mag_n(:,n)=mag(20:length(mag(:,n)),n);

%LP=[1 400 750 length(mag_n)];
%LP=[1 185 400 length(mag_n)];
LP=[1 400 750 length(mag_n)];

for i=1:3

    [m(i,n),j(i,n)]=max(mag_n(LP(i):LP(i+1)-1,n));

    index(i,n)=j(i,n)+LP(i);
    value(i,n)=m(i,n);
    freq_max(i,n)=freq_n(index(i,n),n);

end

end

%save freq_max_rec.mat freq_max
%save freq_max_eli.mat freq_max
save freq_max_pep.mat freq_max
%save freq_max_wing.mat freq_max
```

## Bibliography

1. Anderson, M. L., Sladek, N. J., Cobb, R. G., "Design, Fabrication, and Testing of an Insect-Sized Wing Flapping Mechanism," *Proceedings of the 49th AIAA Aerospace Sciences Meeting including the New Horizons Forum and Aerospace Exposition*, Orlando, Florida, 2011.
2. Birch, J. M., Dickson, W. B., and Dickinson, M. H., "Force Production and Flow Structure of the Leading Edge Vortex on Flapping Wings at High and Low Reynolds Number," *Journal of Experimental Biology*, Vol. 207, 1063-1072, 2004.
3. Combes, S. A. and Daniel T. L., "Flexural Stiffness in Insect wings I. Scaling and the Influence of Wing Venation", *Journal of Experimental Biology*, Vol. 206, 29-79, 2003.
4. Conn, A., Burgess, S., Hyde, R., and Ling, C. S., "From Natural Flyers to the Mechanical Realization of a Flapping Wing Micro Air Vehicle," *Proceedings of the 2006 IEEE International Conference on Robotics and Biomimetics*, Kunming China, 2006.
5. Craparo, E., and Ingram B., "A Micro-Size Ornithopter Wing Design," *Proceedings from the 41st Aerosopace Sciences Meeting and Exhibit*, Reno, Nevada, 2003.
6. Davis, W. R., Kosicki, B. B., Boroson, D. M., and Kostishack, D. F., "Micro Air Vehicles for Optical Surveillance," *The Lincoln Laboratory Journal*, Vol. 9, Num. 2, 1996.
7. Dickison, M. H., Lehmann, F. O., and Sane, S. P., "Wing Rotation and the Aerodynamic Basis of Insect Flight," *Science Magazine*, Vol. 284, 1999.
8. Ellington, C. P. and Usherwood, J. R., "Lift and Drag Characterisitics of Rotary and Flapping Wings," *AIAA Progress in Aeronautics and Astronautics*, Vol. 195, 231-248, 2001.
9. Ellington, C. P., "Insects Versus Birds: The Great Divide," *Proceedings from the 44th AIAA Aerospace Sciences Meeting and Exhibit*, Reno, Nevada, 2006.
10. Ellington, C. P., "The Novel Aerodynamics of Insect Flight: Applications to Micro Air Vehicles," *The Journal of Experimental Biology*, Vol. 202, 34-39, 1999.
11. Hong, Y and Altman, A., "An Experimental Study of Lift Force Generaton Resulting from Spanwise Flow in Flapping Wings," *Proceedings of the 44th AIAA Aerospace Sciences Meeting and Exhibit*, Reno, Nevada, 2006.
12. Hu, H., and Kumar, A. G., "An Experimental Study of Flexible Membrane Wings in Flapping Flight," *Proceedings from the 47th AIAA Aerospace Sciences Meeting Including The New Horizons Forum and Aerospace Exposition*, Orlando, Florida, 2009.
13. Hu, Z., Cheng, B., and Deng, X., "Lift Generaton and Flow Measurement of a Robotic Insect," *Proceedings from the 49th AIAA Aerospace Sciences Meeting Including the New Horizons Forum and Aerospace Exposition*, Orlando, Florida, 2011.
14. Hundley, R. O., and Gritton, E. C., "Future Technology-Driven Revolution in Military Operations," RAND Corporation, 1994.

15. Issac, K. M., Colozza, A., and Rolwes, J., "Force Measurements on a Flapping and Pitching Wing at Low Reynolds Number," *Proceedings from the 44th Aerospace Sciences Meeting and Exhibit*, Reno, Nevada, 2006.

16. Kochersberger, K., and Abe, C., "A Novel, Low Reynolds Number Moment Balance Design for Micro Air Vehicle Research," *Proceedings from the 35th AIAA Fluid Dynamics Conference and Exhibit, Ontario, Canada, 2005.*

17. Kumar, R., Silin, D., Shkarayev, S., "Experimental Study of Aerodynamic Performance of Locust and Model Wings," *Proceedings from the 49th AIAA Aerospace Sciences Meeting including the New Horizons Forum and Aerospace Exposition*, Orlando, Florida, 2011.

18. Lentink, D., and Gerritsma, M., "Influence of Airfoil Shape on Performance in Insect Flight," *Proceedings from the 33rd AIAA Fluid Dynamics Conference and Exhibit*, Orlando, Florida, 2003.

19. Lian, Y., Shyy, W., and Haftka, R., "Shape Optimization of a Membrane Wing for Micro Air Vehicles," *Proceedings from the 41st Aerospace Sciences Meeting and Exhibit*, Reno, Nevada, 2003.

20. McMichael, James M. and Col. Michael S. Francis, USAF (Retired), "Micro Air Vehicles- Toward a New Dimension in Flight," *Federation of American Scientists*, August 7th 1997, www.fas.org.

21. Nicholson, B., Page, S., Dong, H., and Slater, J., "Design of a Flapping Quad-Winged Micro Air Vehicle," *Proceedings from the 37th AIAA Fluid Dynamics Conference and Exhibit*, Miamai, Florida, 2007.

22. Office of the Secretary of Defense, "UAS Roadmap 2005," 2005.

23. Sallstrom, E., Ukeiley, L., and Wu, P., "Aerodynamic Forces on Flexible Flapping Wings," *Proceedings of the 49th AIAA Aerospace Sciences Meeting including the New Horizons Forum and Aerospace Exposition*, Orlando, Florida, 2011.

24. Shkarayev, S., and Silin, D., "Aerodynamics of Flapping-Wing Micro Air Vehicles," *Proceedings from the 47th AIAA Aerospace Sciences Meeting Including The New Horizons Forum and Aerospace Exposition*, Orlando, Florida, 2009.

25. Wei, S., Lian, Y., Tang, J., Viieru, D., and Liu, H., "Aerodynamics of Low Reynolds Number Flyers", Cambridge University Press, New York, 2008.

26. Singh, Beerinder and Inderjit Chopra, "Dynamics of Insect-Based Flapping Wings: Loads Validation," *Proceedings of the 47th AIAA/ASME/ASCE/AHS/ASC Structures, Structural Dynamics, and Materials Conference*, Newport, Rhode Island, 2009.

27. Sunada, S., and Ellington, C. P., "A New Method for Explaining the Generation of Aerodynamic Forces in Flapping Flight," *Mathematical Methods in Applied Sciences*, Vol. 24, 1377-1386, 2001.

28. Teoman, E., and Church D. L., "General Laser Micromachining Princples," *TeoSys Engineering LLC*, 2006.

29. Viieru, D., Tang, J., Lian, Y., Liu, H., and Shyy, W., "Flapping and Flexible Wing Aerodynamics of Low Reynolds Number Flight Vehicles," *Proceedings*

*from the 44<sup>th</sup> AIAA Aerospace Sciences Meeting and Exhibit*, Reno, Nevada, 2006.

30. Wilson N., and Wereley, N., "Experimental Investigation of Flapping Wing Performance in Hover," *Proceedings from the 48<sup>th</sup> AIAA/ASME/ASCE/AHS/ASC Structures, Structural Dynamics, and Materials Conference*, Honolulu, Hawaii, 2007.

31. Wood, R. J., "Design, Fabrication, and Analysis of a 3DOF, 3cm Flapping Wing MAV," *Proceedings of the 2007 IEEE/RSJ International Conference on Intelligent Robots and Systems*, San Diego, California, November 2007.

32. Wood, R. J., Avadhanula, S., Menon, M., Fearing, R. S., "Microrobotics Using Composite Materials: The Micromechanical Flying Insect Thorax," *Proceedings from the IEEE International Conference on Robotics and Automation*, 2003.

33. Wood, R. J., Steltz, E., and Fearing, R. S., "Optimal Energy Density Piezoelectric Bending Actuators," *Sensors and Actuators*, Vol. 119, 476-488, 2005.

34. Wood, R., and Fearing R., "Flight Force Measurements for a Micromechanical Flying Insect," *Proceedings from the IEEE/RSJ International Conference on Intelligent Robots and Systems, Maui, Hawaii, 2001*.

35. Wu, P., and Ifju, P., "Experimental Methodology for Flapping Wing Structure Optimization in Hovering Flight of Micro Air Vehicles," *Proceedings from the 51<sup>st</sup> AIAA/ASME/ASCE/AHS/ASC Structures, Structural Dynamics, and Materials Conference*, Orlando, Florida, 2010.

36. Xie, L., Wu, P., and Ifju, P., "Advanced Flapping Wing Structure Fabrication for Biologically-Inspired Hovering Flight," *Proceedings 51<sup>st</sup> AIAA/ASME/ASCE/AHS/ASC Structures, Structural Dynamics, and Materials Conference*, Orlando, Florida, 2010.

37. Zbikowski, R., Pedersen, C. B., Hameed A., Friend, C. M., and Barton, P.C., "Current Research on Flapping Wing Micro Air Vehicles at Shrivenham," *Proceedings of the AVT Symposium on Unmanned Vehicles for Aerial, Ground, and Naval Military Operations*, Ankara, Turkey, 2000.

38. Zdunich, P., Bilyk, D., MacMaster, M., Loewen, D., Delaurier, J., Kornbluh, R., Low, T., Stanford, S., and Holeman D., "Development and Testing of the Mentor Flapping-Wing Micro Air Vehicle," *Journal of Aircraft*, Vol. 44, No. 5, 2007.

| REPORT DOCUMENTATION PAGE | | *Form Approved* *OMB No. 074-0188* |
|---|---|---|

The public reporting burden for this collection of information is estimated to average 1 hour per response, including the time for reviewing instructions, searching existing data sources, gathering and maintaining the data needed, and completing and reviewing the collection of information. Send comments regarding this burden estimate or any other aspect of the collection of information, including suggestions for reducing this burden to Department of Defense, Washington Headquarters Services, Directorate for Information Operations and Reports (0704-0188), 1215 Jefferson Davis Highway, Suite 1204, Arlington, VA 22202-4302. Respondents should be aware that notwithstanding any other provision of law, no person shall be subject to an penalty for failing to comply with a collection of information if it does not display a currently valid OMB control number.
**PLEASE DO NOT RETURN YOUR FORM TO THE ABOVE ADDRESS.**

| 1. REPORT DATE *(DD-MM-YYYY)* 03-03-2011 | 2. REPORT TYPE Master's Thesis | 3. DATES COVERED *(From – To)* March 2010 – March 2011 |
|---|---|---|

| TITLE AND SUBTITLE Flapping Wing Micro Air Vehicle Wing Manufacture and Force Testing | 5a. CONTRACT NUMBER |
|---|---|
| | 5b. GRANT NUMBER |
| | 5c. PROGRAM ELEMENT NUMBER |
| 6. AUTHOR(S) Sladek, Nathanael J., 2nd Lt., USAF | 5d. PROJECT NUMBER If funded, enter ENR # |
| | 5e. TASK NUMBER |
| | 5f. WORK UNIT NUMBER |

| 7. PERFORMING ORGANIZATION NAMES(S) AND ADDRESS(S) Air Force Institute of Technology Graduate School of Engineering and Management (AFIT/ENY) 2950 Hobson Way, Building 640 WPAFB OH 45433-8865 | 8. PERFORMING ORGANIZATION REPORT NUMBER AFIT/GA/ENY/11-M14 |
|---|---|
| 9. SPONSORING/MONITORING AGENCY NAME(S) AND ADDRESS(ES) Air Force Research Laboratory, Air Vehicles Directorate Attn: Gregory H. Parker Building 24B 2145 Fifth Street WPAFB, OH 45433 (937) 255-7750 | 10. SPONSOR/MONITOR'S ACRONYM(S) AFRL/RBAL |
| | 11. SPONSOR/MONITOR'S REPORT NUMBER(S) |

**12. DISTRIBUTION/AVAILABILITY STATEMENT**
 APPROVED FOR PUBLIC RELEASE; DISTRIBUTION UNLIMITED.

**13.** SUPPLEMENTARY NOTES
This material is declared a work of the U.S. Government and is not subject to copyright protection in the United States.

**14. ABSTRACT**
Numerous wing manufacturing techniques have been developed by various universities for research on Flapping Wing Micro Air Vehicles. Minimal attention though is given to repeatability of wing aerodynamics and dynamic response, which is crucial to avoid asymmetric flapping. Thus the focus of this research becomes twofold. First, repeatable wing manufacturing techniques are developed to ensure flapping wings have similar aerodynamic and dynamic characteristics. For this purpose, four wing designs were selected to not only test the aerodynamics of the different designs, but to also validate manufacturing techniques. The various wing designs are assessed using two methods: dynamic and aerodynamic data. Dynamic data, specifically the wing's structural dynamic response, is measured using a 3D laser vibrometer. From this vibration data, the wings natural frequency modes can be determined which should correlate strongly within the various wing designs if the manufacturing techniques are repeatable. Next, using a piezoelectric flapping actuator, the four wing designs are flapped with force data collected. This data is then used to determine the aerodynamic characteristics of each wing. From the two methods of wing evaluation, it was found that the wings manufactured using a three-layer carbon layup showed greater structural dynamic modal repeatability as compared to one-layer carbon wings. Additionally, Wing Design 3 flapped with the most efficiency with a significantly higher lift to drag ratio as compared to the other wing designs. From this research, the wing manufacturing techniques are quantitatively shown to be repeatable while an optimal wing design based on the maximum lift-to-drag ratio is found which can be used for future research.

**15. SUBJECT TERMS**
 Flapping Wing Micro Air Vehicles

| 16. SECURITY CLASSIFICATION OF: | | | 17. LIMITATION OF ABSTRACT | 18. NUMBER OF PAGES | 19a. NAME OF RESPONSIBLE PERSON Richard G. Cobb, Civ AFIT/ENY |
|---|---|---|---|---|---|
| a. REPORT U | b. ABSTRACT U | c. THIS PAGE U | UU | 133 | 19b. TELEPHONE NUMBER *(Include area code)* (937) 255-3636, ext 6124 (richard.cobb@afit.edu) |

**Standard Form 298 (Rev. 8-98)**
Prescribed by ANSI Std. Z39-18

121